Universidade de São Paulo
Instituto de Física

Estudo de efeitos do meio sobre observáveis de jatos em colisões entre íons-pesados relativísticos

Maria Monalisa de Melo Paulino

Orientador: Prof. Dr. Marcelo Gameiro Munhoz

Dissertação de mestrado apresentada ao Instituto de Física da Universidade de São Paulo, como requisito parcial para a obtenção do título de Mestra em Ciências.

Banca Examinadora:
Prof. Dr. Marcelo Gameiro Munhoz - Orientador (IFUSP)
Prof. Dr. Murilo Santana Rangel (UFRJ)
Prof. Dr. Fernando Gonçalves Gardim (UNIFAL-MG)

São Paulo
2023

FICHA CATALOGRÁFICA
Preparada pelo Serviço de Biblioteca e Informação do Instituto de Física da Universidade de São Paulo

Paulino, Maria Monalisa de Melo

Estudo de efeitos do meio sobre observáveis de jatos em colisões entre íons-pesados relativísticos. São Paulo, 2023.

Dissertação (Mestrado) - Universidade de São Paulo. Instituto de Física. Depto. de Física Nuclear.

Orientador: Prof. Dr. Marcelo Gameiro Munhoz

Área de Concentração: Física de Altas Energias.

Unitermos: 1. Física de altas energias; 2. Cromodinâmica quântica; 3. Quarks; 4. Íons pesados relativísticos.

USP/IF/SBI-079/2023

University of São Paulo
Physics Institute

Study of the medium effects in jet observables in relativistic heavy-ion collisions

Maria Monalisa de Melo Paulino

Supervisor: Prof. Dr. Marcelo Gameiro Munhoz.

Dissertation submitted to the Physics Institute of the University of São Paulo in partial fulfillment of the requirements for the degree of Master of Science.

Examining Committee:
Prof. Dr. Marcelo Gameiro Munhoz - Supervisor (IFUSP)
Prof. Dr. Murilo Santana Rangel (UFRJ)
Prof. Dr. Fernando Gonçalves Gardim (UNIFAL-MG)

São Paulo
2023

À todas as mulheres da família

Agradecimentos

Dedico este trabalho à minha querida família, liderada por incríveis mulheres cearenses. Este é apenas o começo de uma jornada acadêmica que espero que se multiplique na nossa família. Sou profundamente grata pelos valores que aprendi até agora, pela minha determinação e independência, especialmente à minha mãe, Rosângela, à minha madrinha, Valdênia e às minhas primas, Paulinha e Dizinha. Também dedico este trabalho ao meu irmão Joalis e ao meu primo, Jonas, que sempre apoiaram e incentivaram os meus sonhos e ideias.

Também dedico este trabalho à Associação Oportunize, por ter reconhecido em mim uma criança com anseios por melhores oportunidades de ensino. Sem os anos que passei em uma escola de qualidade, proporcionados por essa associação, eu não teria alcançado o título de Mestre em Física.

Gostaria de expressar minha profunda gratidão à família que construí aqui no Sudeste, em especial ao meu companheiro de jornada, Luighi, por todo seu apoio, calma e parceria, utilizando sempre as melhores palavras para me incentivar, e, também, aos seus pais, José e Regina, que me ensinaram muito sobre amor e paciência. Quero agradecer também aos amigos que têm proporcionado apoio emocional fundamental até o momento, com conversas e cafés que causam conforto nos momentos difíceis: Eliana, Maria Paula, Teresa, Agnes, Juliana, Mareu, Lucas Filho, Matheus, Gustavo Sadao, Ana, Fernanda, Lua, Gustavo Alves, Pedro, Natalia, Geovane, Leopoldo, Igor, Antonio e Barbara. Também agradeço à equipe de handebol feminino do IFUSP (Handbohr), que não só me acolheu, mas também me ajudou a encontrar momentos de tranquilidade, mesmo nos desafios mais intensos que a vida de pós-graduanda pode trazer.

Este trabalho não teria chegado ao seu término sem a ajuda quase diária dos meus colegas de trabalho, Leonardo e Fabio, a quem admiro imensamente. Além disso, expresso meu agradecimento ao grupo de pesquisa HEPIC-IFUSP, que me acolheu desde o primeiro ano da graduação.

Por fim, agradeço imensamente ao meu orientador, Marcelo Munhoz pela sua paciência, organização, didática e empatia ao longo deste trabalho de mestrado. Suas orientações foram fundamentais para o sucesso desta pesquisa. Estou profundamente grata pela oportunidade de aprender com você e pela confiança que depositou em mim durante este período.

Abstract

This work aims to study phenomenologically the influence of the medium formed in collisions between heavy ions on the propagation of jets originating from the fragmentation of partons. The project implements a model of partonic propagation a non-homogeneous and hydrodynamically expanding medium using the Monte Carlo event generators JEWEL (Jet Evolution With Energy Loss), T$_R$ENTo for initial medium conditions, and the (2+1)D v-USPhydro for the event-by-event evolution of a realistic medium. The group has previously combined these models, enabling the study of a new series of observables related to jets generated by heavy quarks beyond R_{AA}, such as di-jet (x_J), jet mass (M_{jet}) and semi-inclusive hadron-jet. These observables have been the subject of numerous experimental measurements, but there is a scarcity of models that seek to describe their behavior.

All observables are presented for central and peripheral PbPb collisions at 2.76 TeV and 5.02 TeV, following the experimental setups of the LHC Run-2, for anti-k$_T$ jets with varying radius R from 0.2 to 1.0. The simulated nuclear modification factor R_{AA} and jet mass M_{jet} satisfactorily reproduce experimental results for both central and peripheral collisions when using the combination of models without thermal background subtraction. On the other hand, the semi-inclusive hadron-jet (h-jet) and the di-jet x_J observables have demonstrated their indifference to changes in the surrounding medium. The results with respect to centrality and the value of R suggest the opportunity to gain a deeper understanding of the medium response using JEWEL with thermal subtraction.

Keywords: High Energy Physics; Quark-Gluon-Plasma; Heavy-Ion; Hydrodynamics; Quantum Chromodynamics.

Resumo

Este trabalho tem como objetivo estudar fenomenologicamente a influência do meio formado em colisões entre íons pesados na propagação de jatos originados a partir da fragmentação de pártons. O projeto implementa em um modelo de propagação partônica em um meio não homogêneo e em expansão hidrodinâmica por meio dos geradores de eventos Monte Carlo JEWEL (Jet Evolution With Energy Loss), T$_R$ENTo para condições iniciais do meio e o (2+1)D v-USPhydro para a evolução do meio realista evento a evento. O grupo já realizou anteriormente uma combinação desses modelos, o que permitirá o estudo de uma nova série de observáveis correspondentes a jatos gerados por quarks pesados além do R_{AA}, como o di-jet (x_J), o jet mass (M_{jet}) e o semi-inclusivo hadron-jato (h-jet). Esses observáveis têm sido objeto de inúmeras medidas experimentais, porém, há escassez de modelos que busquem descrever o comportamento desses observáveis. Todos observáveis são apresentados para colisões centrais e periféricas de PbPb a 2.76 TeV e a 5.02 TeV, seguindo as configurações experimentais da Run-2 do LHC, para jatos anti-k$_T$ com raios R variando de 0.2 a 1.0. Os observáveis fator de modificação nuclear R_{AA} e jet mass M_{jet} simulados reproduzem satisfatoriamente os resultados experimentais para colisões centrais e periféricas ao utilizar a combinação de modelos sem subtração térmica de background. Enquanto que o semi-inclusivo hadron-jato h-jet e o observável di-jet x_J mostraram-se indiferente à alterações de meio. Os resultados com relação à centralidade e ao valor de R sugere a oportunidade de obter uma compreensão mais aprofundada da resposta do meio utilizando o JEWEL com subtração térmica.

Palavras Chave: Física de Altas Energias; Plasma de Quarks e Glúons; Íons Pesados; Hidrodinâmica; Cromodinâmica Quântica.

List of Figures

List of Tables

Contents

Introduction

> ***"Nothing in life is to be feared. It is only to be understood."***
>
> (Marie Curie)

In recent decades, understanding the first microseconds of the Universe's existence has been a central focus of high-energy physics [1]. Experiments conducted at the Large Hadron Collider (LHC) at CERN and the Relativistic Heavy-Ion Collider (RHIC) at the Brookhaven National Laboratory (BNL) have played a crucial role in pushing the boundaries of our understanding. These experiments aim to generate and study the Quark-Gluon Plasma (QGP), an extraordinary state of matter formed in relativistic heavy-ion collisions [2, 3]. The QGP, a liquid-like phase of strongly interacting matter, is characterized by its extremely high energy density and temperature, which cause the confinement of quarks and gluons within hadronic structures to break down [4]. Through the use of several models, scientists have made significant progress in unraveling the expansion, cooling, and particle production processes within the QGP, providing insights into the fundamental nature of the strong force [4].

In addition to the formation of the QGP, heavy-ion collisions involve high-momentum interactions known as hard scatterings, where partons in the early stages of the collision exchange energy and momentum. These interactions are described by perturbative Quantum Chromodynamics (pQCD), which is based on the concept of asymptotic freedom [5]. As partons pass through the medium, they undergo a cascade-like process called parton shower, which can go through modifications due to the presence of the QGP. The study of resulting objects called jets, which are collimated sprays of particles, offers valuable insights into the properties of the deconfined matter [6]. However, the sensitivity of jets to the finer details of the QGP and its evolution remains uncertain, as high-energy partons can escape the medium with minimal interaction. Thus, analyzing jet distributions in heavy-ion collisions, particularly in comparison to proton-proton collisions, is crucial for understanding these complex interactions [6].

The main objective of this study is to explore the interplay between jets and the medium by comparing experimental data with advanced Monte Carlo event generators. Two models, JEWEL (Jet Evolution With Energy Loss) [7] and PYTHIA [8], serve as frameworks for simulating the entire evolution of partons in heavy-ion collisions, encompassing the initial hard scattering, in-medium shower evolution, gluon emission, and hadronization. Although JEWEL assumes a simplified smooth medium with longitudinal-only expansion, it succeeds in explaining several observables under this idealized assumption [7, 9, 10]. However, there is a need for more realistic medium simulations, which is fulfilled by the state-of-the-art v-USPhydro code [11, 12]. This code utilizes the Smooth Particle Hydrodynamics (SPH) Lagrangian method [13, 14] to solve the viscous hydrodynamic equations of the QGP in the transverse plane on an event-by-event basis, considering different initial conditions and incorporating transverse and viscosity expansion, which are absent in the original model.

The chosen observables for this study include the nuclear modification factor R_{AA}, the dijet asymmetry x_j, the jet mass M_{jet}, and the semi-inclusive hadron-jet correlation h_{jet}. By varying parameters such as the impact parameter and the collision centrality in the simulations, we aim to assess the sensitivity of each observable to medium modifications.

Chapter 1 will explore important theories, including Quantum Chromodynamics, Quark-Gluon Plasma, Hydrodynamics, Jet Quenching, and Hadronization. To provide the necessary theoretical background for the simulated collisions in this work. In Chapter 2, we will describe the hydrodynamic models and the jet reconstruction techniques employed in relativistic heavy-ion collisions and provide insights into the simulation and analysis procedures. Subsequent chapters will present the definitions and results obtained from varying several parameters for the observables mentioned above. Finally, we will conclude with a comprehensive discussion of the findings regarding the influence of the medium on jets in relativistic heavy-ion collisions.

Chapter 1

Theory

1.1 Quantum Chromodynamics

Quantum Chromodynamics (QCD) is a quantum field theory that describes the strong interaction between particles. It is formulated in the non-Abelian gauge symmetry group SU(3), where gluons mediate the interaction between quarks, the elementary constituents of hadrons. The QCD Lagrangian, which governs the system, can be written as [15, 16]:

$$\mathcal{L}_{QCD} = -\frac{1}{4}F^a_{\mu\nu}F^{a\mu\nu} + \sum_f \bar{q}_f(i\gamma^\mu D_\mu - m_f)q_f, \tag{1.1}$$

where $F^a_{\mu\nu}$ is the field strength tensor for gluons, $q_f$is the Dirac field for quark flavor f,m_f is the quark mass, and $D_\mu = \partial_\mu + igA^a_\mu \frac{\lambda_a}{2}$ is the covariant derivative and λ^a are matrices that satisfy:

$$\left[\frac{\lambda^a}{2}, \frac{\lambda^b}{2}\right] = if^{abc}\frac{\lambda^c}{2}, \tag{1.2}$$

with the normalization condition $tr(\lambda^a\lambda^b) = 2\delta^{ab}$. The field strength tensor $F^a_{\mu\nu}$ is defined as:

$$F^a_{\mu\nu} = \partial_\mu A^a_\nu - \partial_\nu A^a_\mu + gf^{abc}A^b_\mu A^c_\nu \tag{1.3}$$

where A^a_μ represents the gluon field, g_s is the strong coupling constant, and f^{abc} are the structure constants of the SU(3) group and a is a combination of colour and anticolour.

Quantum Chromodynamics describes strong interactions involving 8 gluons, corresponding to the eight generators in the SU(3) group. The non-commutativity of the theory successfully captures essential aspects of the strong force. One notable feature is that gluons carry both color and anticolor charge, allowing them to interact with each other. This self-interaction of gluons gives rise to the phenomenon known as asymptotic freedom.

In field strength tensor and D_μ, the constant g represents the gauge coupling, which is related to the coupling constant of the strong force, denoted as α_s ($g^2 = 4\pi\alpha_s$). The coupling constant is a parameter that determines the strength of the strong interaction.

The strength of the interaction between quarks, and therefore the degree of confinement, is determined by the coupling constant, α_s. In perturbative Quantum Chromodynamics (pQCD), the coupling constant α_s is found to be given by Equation 1.4, which is valid for high values of Q^2.

$$\alpha_s(Q^2) = \frac{12\pi}{(33 - 2n_f)\ln\bigl(Q^2/\Lambda^2_{QCD}\bigr)} \tag{1.4}$$

where n_f is the number of quark flavors active at the scale Q^2 [17].

The parameter Λ is referred to as the QCD scale constant. When $Q^2 \gg \Lambda^2$, the coupling constant becomes small, leading to deconfinement and a perturbative treatment of QCD. However, when $Q^2 = \Lambda^2$, the coupling constant diverges. It should be noted that the expression for α_s is derived from the one-loop approximation. Hence the divergence of the coupling constant in non-perturbative regimes is expected. Furthermore, $\alpha_s(\mu_R^2)$ is defined by Λ for a specific n-loop approximation, and the value of Λ depends on the method used to solve the renormalization group equation.

Quantitative lattice QCD (l-QCD) calculations, which involve discretizing space-time and solving QCD equations on a grid, support the predictions of asymptotic freedom. These calculations demonstrate that matter undergoes a phase transition from a hadronic gas to a Quark-Gluon Plasma (QGP). The transition typically occurs at a temperature (T) between 150 MeV and 190 MeV, corresponding to an energy density (ε) of approximately 1 GeV/fm^3 [18].

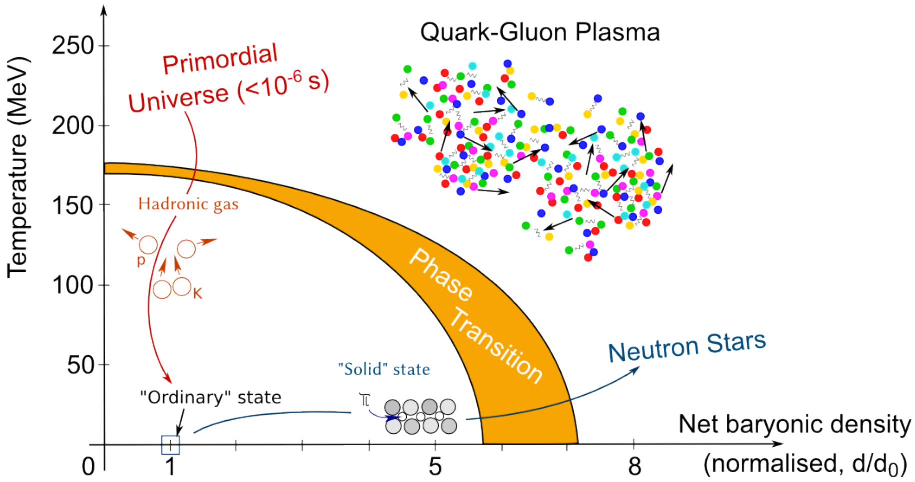

Figure 1.1: Phase diagram of the QCD depicting the expected QGP phase transition. Fig. from [19].

Figure 1.1 presents the theoretical phase diagram of Quantum Chromodynamics (QCD), providing a visual representation of the temperature and baryonic chemical potential ranges where the Quark-Gluon Plasma (QGP) exists, as well as the transitional region corresponding to the hadronic phase.

1.2 Quark-Gluon Plasma

Given the considerations above, investigating the quark-gluon plasma (QGP) state holds significant importance in comprehending the QCD phase diagram and the transition from the hadronic phase to strongly interacting matter. Consequently, there is a strong demand for experimental methods to explore and evaluate the properties of the QGP.

Figure 1.1 highlights the remarkable nature of the conditions required for forming the quark-gluon plasma (QGP) and the transition to the hadronic phase. Replicating this state in a controlled manner is only possible through specific and stringent experimental conditions that can achieve an equivalent energy density. The elevated temperatures attained in heavy-ion collisions make them well-suited for QGP studies and represent the only means by which humans have been able to reproduce, under controlled circumstances, the conditions resembling the early stages of the universe. Figure 1.2 provides a schematic depiction of a heavy-ion collision.

Figure 1.3 provides a schematic illustration of the evolutionary stages of a heavy-ion collision. The vertical axis, represented by the coordinate t, denotes time, while the horizontal axis represents the beam direction. The various stages of evolution are

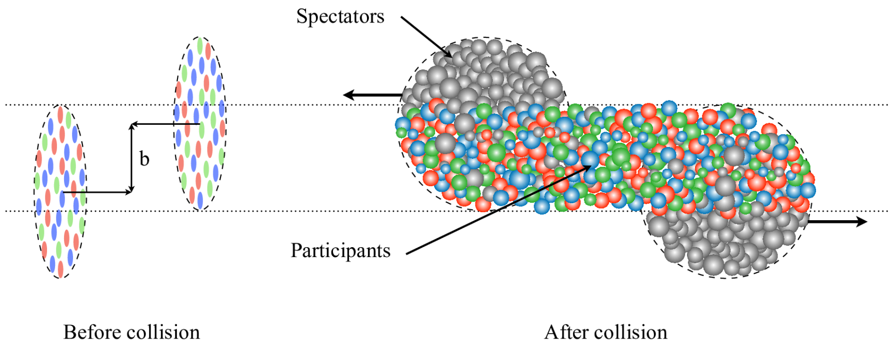

Figure 1.2: The diagram presented offers a visual representation of a heavy-ion collision, displaying essential elements such as the impact parameter b, as well as the presence of spectator nucleons and participant nucleons. [20].

described as follows:

1. In the *pre-equilibrium* stage of a heavy-ion collision, immediately following the collision itself, a significant number of quarks and gluons are generated through inelastic collisions. During this phase, the matter exists in a state of pre-equilibrium, where the newly created partons interact. As the density increases, the production of quark-antiquark ($q\bar{q}$) pairs intensifies.

2. The *formation of the QGP* occurs when the partonic matter reaches a state of equilibrium. At this stage, the matter transitions into the unique state of matter composed of deconfined quarks and gluons.

3. In the quark-gluon plasma (QGP), the pressure is exceptionally high, leading to the expansion of the medium driven by pressure gradients. As the QGP expands, the density progressively decreases, initiating the process of *hadronization*, the formation of particles composed of quarks and anti-quarks.

4. During the system's evolution, the expansion continues until it reaches a point where elastic collisions between particles cease to occur due to the decrease in temperature. At this stage, known as the phase of *free hadrons*, the momenta of the hadrons become fixed and no longer change significantly.

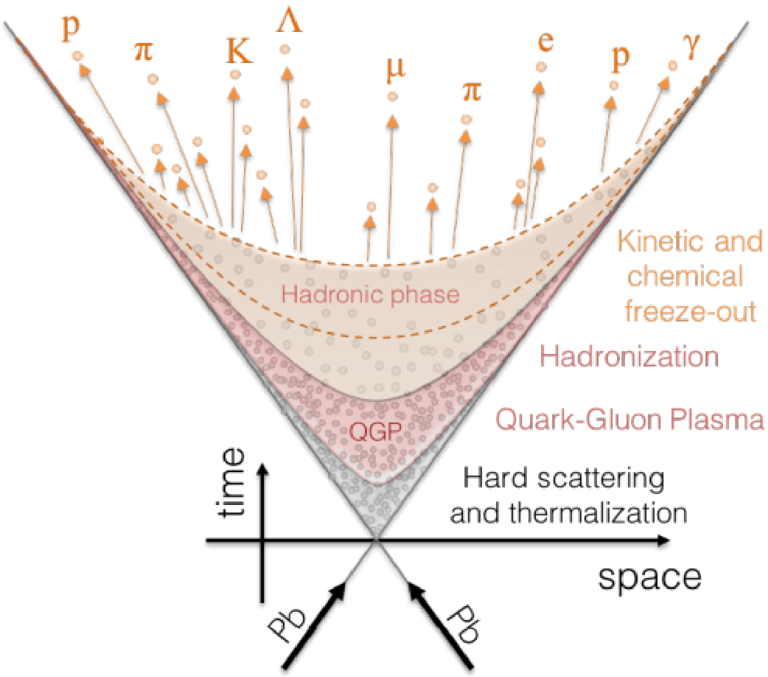

Figure 1.3: Heavy-ion collisions undergo an evolution comprising a pre-equilibrium phase, QGP formation, expansion, cooling, and hadron formation. Detectors measure free hadrons produced in this process to study their properties [21].

Considerable dedication has been invested in investigating the properties of the quark-gluon plasma (QGP) through heavy-ion collisions, utilizing the Large Hadron Collider (LHC) as the latest and most extensive experimental apparatus. Heavy-ion collision studies are integral to the LHC's physics program, with the first lead-lead (Pb-Pb) collision in late 2010. Four detectors, namely ALICE (A Large Ion Collider Experiment), ATLAS (A Toroidal LHC ApparatuS), CMS (Compact Muon Spectrometer), and LHCb (Large Hadron Collider beauty), actively contribute to the LHC's heavy-ion program. ALICE is the only experiment mainly dedicated to QGP studies.

The LHC is the most powerful particle accelerator ever constructed, surpassing the collision energies of the Relativistic Heavy Ion Collider (RHIC) by more than an order of magnitude. The LHC has initially delivered Pb-Pb collisions at $\sqrt{s_{NN}} = 2.76$ TeV, reaching even higher energy levels in 2015 and 2018 (run-2), with Pb-Pb collisions at $\sqrt{s_{NN}} = 5.02$ TeV and pp collisions at $\sqrt{s} = 13$ TeV, and in 2022, with the commencement of run-3, the energy level was elevated for Pb-Pb collisions at $\sqrt{s_{NN}} = 5.5$ TeV, setting new records in energy exploration.

The LHC also has been investigating phenomena such as jet quenching. Jet quenching refers to the decrease in jet energy observed in nucleus-nucleus (AA) collisions compared to proton-proton (pp) collisions. When partons originating from the hard scattering of nucleons traverse a non-transparent medium, their behavior is expected to be modified, see Fig. 1.4. The observed suppression in the transverse momentum spectra of jet constituents provides evidence for the existence of this medium. These partons, produced in the early stages of the collision, carry valuable information about the medium as they evolve. Consequently, they serve as probes for studying the characteristics of the QGP.

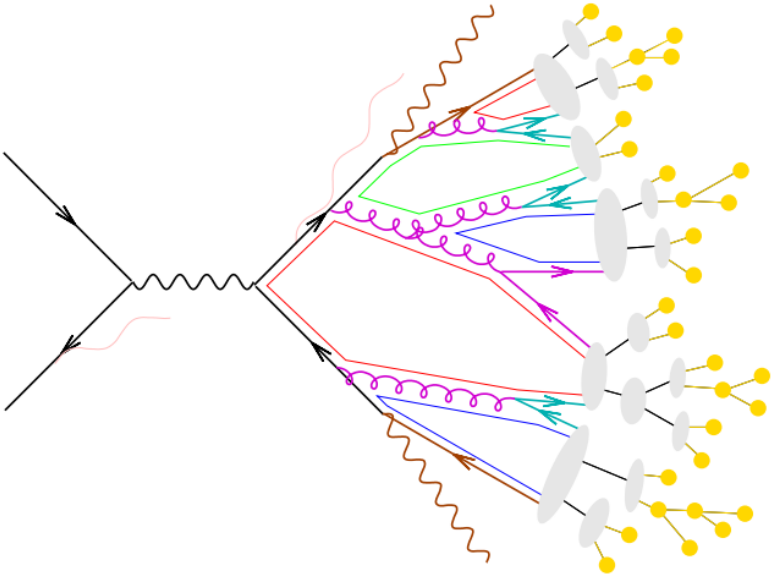

Figure 1.4: Schematic view of the hadronization process [22]. At a certain point of this parton shower, marked by the gray spots, the quarks, and gluons are converted into hadrons, a process which, as of today, can only be described phenomenologically.

To quantify the modification experienced by the partons during their evolution through the medium, the ratio of the jet transverse momentum spectrum in AA and pp collisions is calculated, with appropriate adjustments as necessary. This quantity, known as the nuclear modification factor R_{AA}, is introduced in Section 3.1 and serves as an observable that quantifies the effects of the medium on the partons. The LHC's high-energy collisions have provided valuable insights into the study of jet quenching and its relation to the QGP.

Furthermore, we are also interested in understanding the properties of jets generated in heavy-ion collisions by exploring specific observables such as di-jets, jet mass, and hadron-jet correlation. The study of these observables provides valuable information about the interaction between jets and the medium formed during collisions. In the study of di-jets in Section 3.2, the investigation will center on the sharing of jet energy through an analysis of the energy fraction contained in the secondary jet relative to the energy of the higher-energy jet. In Section 3.3, the analysis of jet mass allows us to investigate jets' internal structure and the medium's influence on their formation. In Section 3.4, the hadron-jet correlation helps us understand how composite hadrons (particles composed of quarks and anti-quarks) are produced about jets and how this production is affected by the surrounding medium. Understanding these properties will contribute to a more comprehensive understanding of jet dynamics in heavy-ion collisions and the behavior of the QGP, frequently described and modeled using relativistic hydrodynamics to depict its dynamic evolution.

1.3 Hydrodynamics

Hydrodynamics is an extension of fluid mechanics that deals with systems in which the macroscopic properties of the fluid, such as pressure, density, velocity, and temperature, are described in terms of continuous fields in space and time. The fundamental principles of hydrodynamics are based on conservation laws, including the conservation of mass, conservation of momentum, and conservation of energy. These laws describe how physical quantities behave in a fluid system as the fluid flows and deforms [4].

In hydrodynamics, fluids are treated as continuous media, and macroscopic phenomena are described by partial differential equations known as hydrodynamic equations. The hydrodynamic equations depend on the type of fluid, its thermodynamic properties, and the boundary conditions imposed on the system.

Realistic hydrodynamics is a fundamental tool for studying the evolution of the Quark-Gluon Plasma (QGP) created in heavy-ion collisions. Once the QGP is formed, it rapidly expands and cools, undergoing various distinct phases before eventually condensing back into stable particles that can be detected in experiments. The QGP exhibits collective behavior throughout this evolution, such as particle flow and energy dissipation. Realistic hydrodynamics mathematically describes these collective phenomena, enabling scientists to comprehend how the QGP behaves as an almost perfect fluid with very low viscosity.

Relativistic hydrodynamics describes the collective behavior of the Quark-Gluon Plasma (QGP). The relativistic hydrodynamic equations include the conservation equation for energy-momentum, given by [5]:

$$\partial_\mu T^{\mu\nu} = 0,$$

where ∂_μ represents the four-dimensional covariant derivative operator, and $T^{\mu\nu}$ is the energy-momentum tensor of the QGP. This tensor describes the system's energy density, energy flux, and pressure.

In addition, another crucial equation is the conservation equation for baryons, which is written as:

$$\partial_\mu n_B^\mu = 0,$$

where n_B^μ is the baryonic flow, representing the baryon density.

Furthermore, to study the QGP's behavior, the equation of state that relates the pressure P with the energy density ε and baryon density n_B needs to be incorporated. For the QGP, the equation of state is influenced by Quantum Chromodynamics (QCD) theories at high temperatures and energy densities.

It is important to emphasize that the hydrodynamic equations of the QGP can be pretty complex and require accurate initial conditions and appropriate thermodynamic data to solve the systems of equations. The study of QGP using hydrodynamics is an active area of research, often involving advanced computational simulations to model heavy-ion collisions and the resulting QGP evolution.

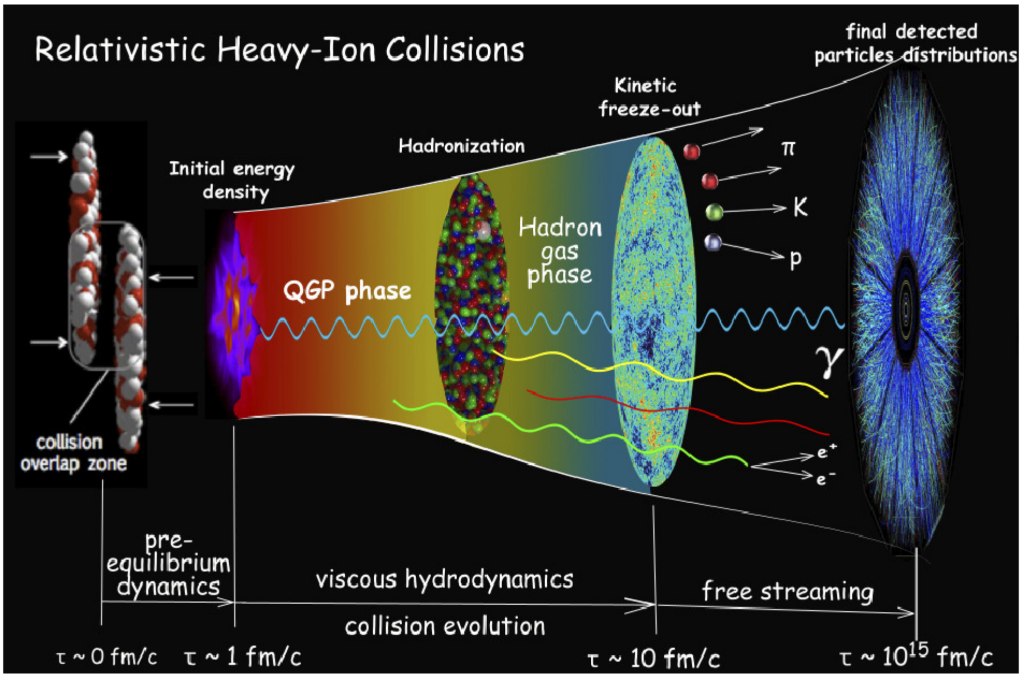

Figure 1.5: Heavy-ion collision scheme. Credit: Paul Sorensen and Chun Shen [23].

During heavy-ion collisions, the evolution of hydrodynamics goes through essential stages. Initially, the medium is highly energetic and out of thermal equilibrium. Next, rapid thermal equilibration and expansion of the medium as a fluid occur. During the Quark-Gluon Plasma (QGP) phase, the medium behaves as an almost perfect fluid, exhibiting low viscosity and preserving initial fluctuations. As the medium cools, quarks and gluons recombine and condense into stable particles, concluding the hydrodynamic phase. Understanding this evolution is crucial to obtaining information about the QGP and comprehending the extreme conditions of the primordial universe.

Over the years, various hydrodynamic models have been employed in physics to comprehend the behavior of Quark-Gluon Plasma (QGP) and its evolution during heavy-ion collisions. Some historically relevant models include [24]:

- **Ideal Hydrodynamics:** Initially, ideal hydrodynamics was extensively utilized to describe the QGP. In this model, the QGP is treated as a fluid with no viscosity, implying no energy dissipation or friction between particles. Despite being a simplified approximation, ideal hydrodynamics was valuable in understanding the collective nature of the QGP during its early phases [25].
- **Viscous Hydrodynamics:** Subsequently, viscous hydrodynamic models were developed to account for the QGP's viscosity, which plays a significant role at high energies. Density affects the energy dissipation rate and can influence the QGP's collective behavior, including initial fluctuations observed in experiments [26].
- **3+1-dimensional Hydrodynamics:** Initially, hydrodynamic models considered the QGP's evolution in two spatial dimensions plus time (2+1 dimensions). However, subsequent studies revealed that the expansion of the QGP occurs in all three spatial dimensions plus time (3+1 dimensions), necessitating the incorporation of 3+1-dimensional hydrodynamic models for a more accurate description [27].
- **Conformal Hydrodynamics:** Considering the Quantum Chromodynamics (QCD) high-energy limit, exhibiting conformal symmetry, conformal hydrodynamics models were developed to describe the QGP's behavior under such conditions. These models are beneficial in studying the QGP at high temperatures and densities, where conformal symmetry is a good approximation [28].
- **Hybrid Models:** With advancements in computational technology, hybrid hydrodynamic models were developed, combining hydrodynamics with other theoretical approaches such as particle thermodynamics and field theory. These models provide a more comprehensive and realistic description of the QGP's evolution and are often employed in simulations for comparison with experimental data [29].

These are just a few examples of historically utilized hydrodynamic models to comprehend the QGP. Each approach possesses its strengths and limitations, and the choice of model depends on the specific properties being investigated and the conditions of the heavy-ion collision under study. These models' continued usage and refinement have been fundamental in advancing our understanding of the QGP and matter's properties under extreme temperature and density conditions.

1.3.1 Parton Shower

The parton shower process corresponds to the cascade production of scattered partons that eventually change into hadronic jets that detectors can measure, see Fig.1.6. A differential equation describes this process' probability of ramification in other partons used in this work. This is a differential cross-section for any process with an additional parton in the final state, $d\sigma_{n+1}$ that can be expressed by the cross-section for the emission of an n-parton final state. See Equation (1.5).

$$d\sigma_{n+1} = \sigma_n \frac{dt\ dz}{t} \frac{\alpha_s(\mu^2)}{2\pi} \hat{P}_{ba}(z) \tag{1.5}$$

This equation is numerically resolved in a Monte Carlo event generator that simulates the evolution of the hadronic jet from the initial parton to the formation of the final hadrons [7].

Where z is the light-cone momentum fraction by the outgoing parton, and $\hat{P}$ is the Altarelli-Parisi splitting function. The parameter t has the nature of additional emission and can also be represented by $t \approx p_\perp^2 \approx Q^2$. The scale μ^2, related to the coupling constant α_s, can be represented by $p_\perp^2$. Upon closer analysis of the equation, it's possible to notice that for emissions at low scales of t (of the order of a few Λ_{QCD}), they typically won't produce any resolvable parton, leading to the termination of such scales within the same hadron as their emitter. To address this issue in JEWEL, an infrared cutoff t_c is introduced, chosen in such a way that $p_\perp^2(t_c) \approx 1$ GeV. However, when implementing this kind of cutoff, z is also affected, preserving the structures within the splitting nuclei. After iterating the equation above any k of additional emissions are obtained:

$$d\sigma_{n+k} = \sigma_n \prod_{j=1}^{k} \frac{dt_j\ dz_j}{t_j} \frac{\alpha_s(p_{\perp,j}^2)}{2\pi} \hat{P}_j(z_j)\Theta(t_{j-1} - t_j) \tag{1.6}$$

where Θ-function represents the Heaviside function, ensuring that the conditions of discontinuity imposed by t_{j-1} and t_j result in a positive value for the equation, in compliance with the existing virtuality. Specifically, if $t_{j-1} - t_j < 0$, Θ-function equals one, while for $t_{j-1} - t_j \geq 0$, Θ returns zero.

The process described above can be represented probabilistically, making it suitable for utilization in simulations involving the *Sudakov form factor* Eq.1.7, where is denoted by the evolution parameter t, which has a linear dependence on the virtuality of the parton and organizes the order of the calculations within the shower. The t_c is an infrared cut-off scale that comes from the attempt to avoid divergences in the collinear limit, that is, $t \to 0$, and that has a partonic moment $p_T^2(t_c) \approx 1$ GeV^2. The range of t and the choice of setting imply a limit of z, such that $t \in [t_c, t_0] \to z \in [z_{min}, z_{max}]$ and t_h comes from multiple branchings with a defined order relation $t_c > t_1 > t_2 > \cdots > t_h$.

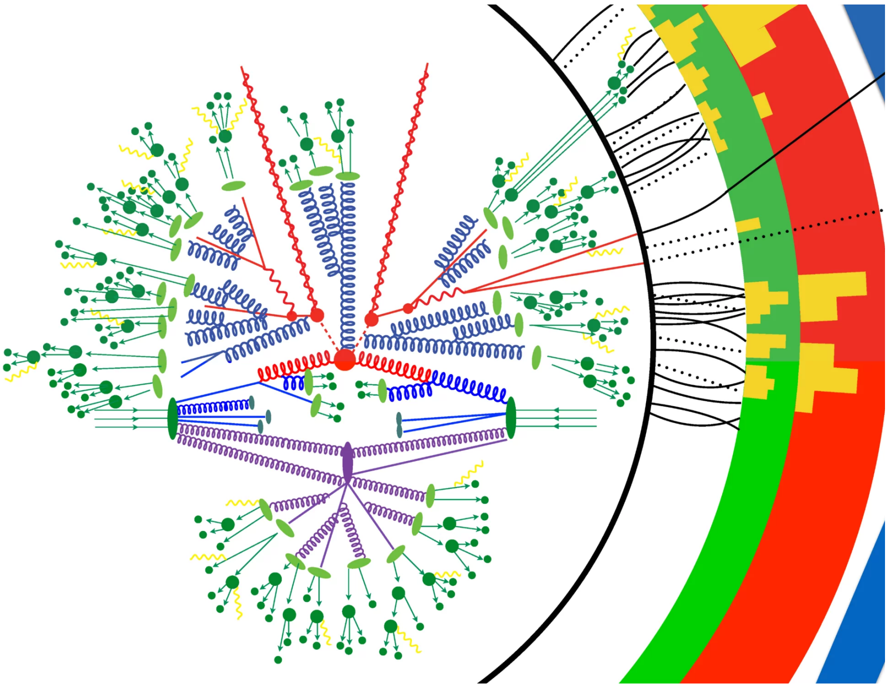

Figure 1.6: Parton showers illustration. Describe the particles and radiation resulting from high-energy particle collisions. Credit: Benjamin Nachman [30].

$$\mathcal{S}_a(t_h, t_c) = \exp\left\{ -\int_{t_c}^{t_h} \frac{dt}{t} \int_{z_{min}}^{z_{max}} dz \sum_b \frac{\alpha_s(p_T^2)}{2\pi} \hat{P}_{ba}(z) \right\} \tag{1.7}$$

This shower will operate as though there is no medium present, what we call a vacuum. The development of future virtuality and the medium modifications of the jet will be made possible by the collisional process. Simple $2 \to 2$ matrix elements squared are used to tackle the collisional component of the JEWEL algorithm. The gluons that represent the scattering centers are given a thermal mass. The Debye mass is determined by $\mu_D \approx 3T$. Thus, the $2 \to 2$ cross-section is

$$\sigma_i(E,T) = \int d|\hat{t}| \int dx \sum_{j \in q,\bar{q},g} f^i_j(x,\hat{t}) \frac{\hat{\sigma}_j}{d\hat{t}}(x\hat{s}, |\hat{t}|) \tag{1.8}$$

where $f^i_j(x,\hat{t})$ represents the PDF that takes into account the potential initial-state radiation from the energetic projectile involved.

Partons, such as quarks or gluons, as they traverse the dense medium of QGP, lose energy due to multiple scatterings and induced gluon radiation, suppressing their energetic particle jets. This phenomenon, known as Jet Quenching, provides valuable information about the properties of QGP, such as its density, viscosity, and opacity, and serves as a powerful tool to explore high-energy physics and Quantum Chromodynamics (QCD) as we will see in the next section.

1.4 Jet Quenching

Jet quenching is a collection of phenomena observed in high-energy heavy-ion collisions resulting from interactions between energetic jet partons and the Quark-Gluon Plasma medium. Due to the substantial transverse momentum transfer in hard processes, the cross-section for initial jet production can be computed using pQCD, which has been demonstrated to agree with experimental data on jet production in proton-proton (pp) collisions. These pQCD calculations for jet production rates can be extended to proton-nucleus (pA) collisions within the collinear pQCD factorization framework, showing agreement with experimental data after accounting for nuclear modification of parton distribution functions. Such calculations for nucleus-nucleus collisions (AA) can be used as baselines for the initial production of jets, against which the medium modification of jet production due to jet quenching can be obtained and compared with experimental data. This includes the suppression of spectra for single hadrons, dihadrons, and γ-hadrons, as well as spectra for single jets, dijets, and γ-jets. [31].

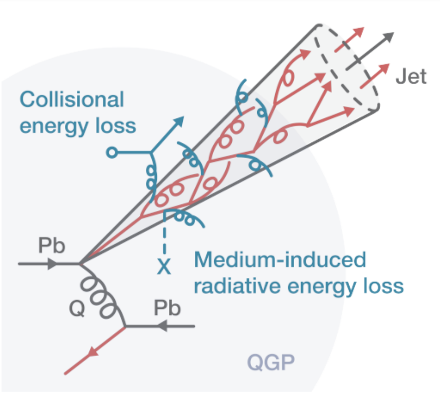

Figure 1.7: Diagram illustrating jet quenching in a head-on nucleus-nucleus collision [32].

Several mechanisms contribute to jet quenching, including gluon radiation induced by the medium, elastic scattering of particles in the medium, and particle absorption by the medium. The energy loss of jets is experimentally measured through the suppression of their energy and transverse momentum distributions compared to reference proton-proton collisions. The study of jet quenching provides crucial insights into the properties of the Quark-Gluon Plasma (QGP), such as its density, viscosity, and opacity. It is a powerful tool for exploring high-energy physics and Quantum Chromodynamics (QCD).

The suppression of jet energy and transverse momentum distributions is calculated concerning reference proton-proton collisions, and the magnitude of this suppression is utilized to extract information about the properties of the Quark-Gluon Plasma (QGP), such as its density and viscosity.

The cross-section is a probability measure of a scattering process occurring in a particle collision. The cross-section can be calculated using perturbative Quantum Chromodynamics (pQCD), a well-established theory describing the strong interaction between particles for initial jet production in high-energy heavy-ion collisions. These pQCD calculations of the jet production rate can serve as baselines for initial jet production in heavy-ion collisions, against which the medium modification of jet production due to jet quenching can be obtained and compared with experimental data. The multiplicity of particles produced in heavy-ion collisions is also essential for understanding the phenomenon of jet quenching, as the energy lost by jet partons is redistributed in the medium and can increase particle multiplicity. Therefore, the cross-section, jet quenching, and multiplicity are related in the sense that all of them are essential for understanding jet production in high-energy heavy-ion collisions and the properties of the Quark-Gluon Plasma (QGP) medium formed in these collisions.

The tool used in this work for simulating this process is the Jet Evolution With Energy Loss (JEWEL) [7, 33, 34] generator of Monte Carlo events based on the formalization of BDMPS-Z [35] that uses QCD (Quantum Chromodynamics) cubes to explain how partons lose energy as they cross the medium and how this loss of energy affects jet evolution. It simulates particulate parton flows with ordered virtuality, i.e., $t = Q^2$, where Q is the virtual parton's mass, taking into account the interaction with a medium, as previously mentioned.

Typically, Monte Carlo (MC) implementations are used in systems referred to as "memory-less" systems. This means that these systems adhere to the Markov property, where the current state depends only on the current step of simulation and is unaffected by earlier states. However, quantum interference contradicts this hypothesis, necessitating a different approach to be taken within the model. In the JEWEL context, the overposition of the formation time of the gluon production in the medium, denoted as τ_f, results in interference with the subsequent spreading processes. As a result, it is necessary to classify these interactions as coherent or incoherent [33].

An abridged representation of the method is shown in [33]. If we consider k_T to be the gluon momentum, w its energy at creation, and ΔL to be the MC specified distance to the next interaction, we have that:

$$\tau_f \equiv \frac{E}{t} = \frac{2w}{k_T^2} \qquad \begin{cases} \Delta L > \tau_f \Rightarrow \text{incoherence} \\ \Delta L < \tau_f \Rightarrow \text{coherence} \end{cases} \tag{1.9}$$

When the gluon formation occurs in an incoherent mode and results in $k_T \to k_T + s_T$, the calculation is repeated. Here, s_T represents the momentum transfer associated with the subsequent scattering center occurring in coherence [36].

1.5 Hadronization

Hadronization is the process by which partons (quarks and gluons) produced in high-energy collisions combine to form hadrons, composite particles such as protons, neutrons, and mesons. Due to the confinement feature of Quantum Chromodynamics (QCD), partons cannot exist as free particles and must, therefore, combine to form hadrons before being observed. Hadronization is a fundamental process in particle physics as it is responsible for developing observable particles in high-energy collision experiments. The detection of hadrons by the large detectors at the LHC occurs after the hadronization process.

Various theoretical models and computational techniques can be utilized to simulate the process of hadronization since it cannot be directly calculated using perturbative Quantum Chromodynamics (pQCD). It is essential to note that hadronization is an active area of research, and the utilized models are continually being refined and developed to match experimental data better.

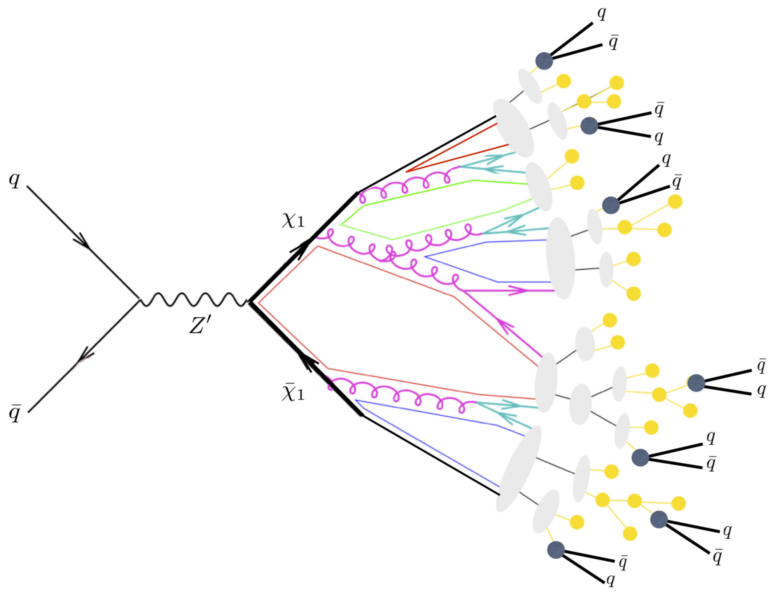

Figure 1.8: Schematic view of the hadronization process [37]. At a certain point of this parton shower, marked by the gray spots, the quarks and gluons are converted into hadrons, a process which, as of today, can only be described phenomenologically.

Each model has its own physical assumptions and limitations, and the choice of model depends on the type of event being simulated and the objectives of the simulation. The string fragmentation model is a hadronization model used in event generators to simulate hadron production in high-energy collisions. The model is based on the idea that field strings transmit the strong force that binds quarks and antiquarks, Fig.1.9. When quarks and antiquarks move away from each other, the string stretches and breaks, producing oppositely charged hadron pairs. The string model is implemented in event generators like PYTHIA [8] and simulates hadron production in high-energy collisions.

PYTHIA [8] is one of the most sophisticated and well-known string models of hadronization, widely used in particle physics to simulate hadron production in high-energy collisions.

In Quantum Chromodynamics (QCD), linear confinement at large distances is expected. This provides the starting point for the string model, which is most easily illus-

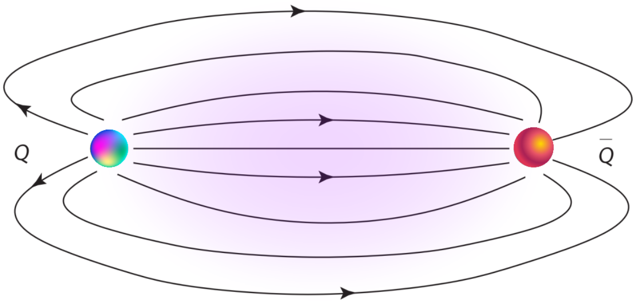

Figure 1.9: A flux tube spanned between a quark and an antiquark.

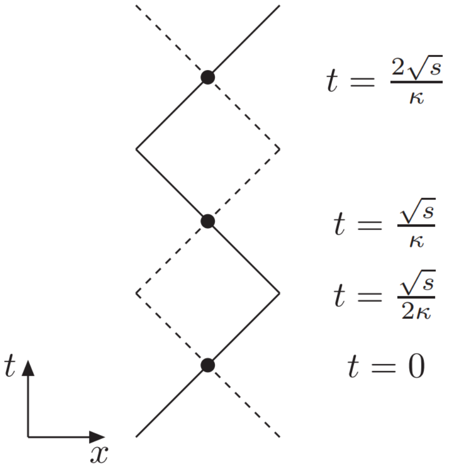

Figure 1.10: Quark-antiquark system depicted by the yo-yo model with characteristic times. Full line for q trajectory dashed for $\bar{q}$, black dots for vertices [39].

trated for producing a back-to-back $q\bar{q}$ pair, for example, in e^+e^- annihilation events. As the partons move apart, the physical picture is that of a color flux tube being stretched between the q and the $\bar{q}$. The transverse dimensions of the tube have typical hadronic sizes, around 1 fm. Assuming the tube is uniform along its length automatically leads to a confinement image with a linearly rising potential, $V(r) = \kappa r$. The string constant κ, i.e., the amount of energy per unit length, is known from hadron mass spectroscopy [38].

Let's consider a color-dipole consisting of a quark-antiquark ($q\bar{q}$) pair with an initial energy of $\sqrt{s}$ in the center-of-mass frame. This dipole is allowed to move along the x-axis, as illustrated in Figure 1.10. Initially, the pair are closely spaced, and all the system's energy is associated with their relative motion. Their momenta are transferred to the string as they separate, converting into the field's potential energy. This potential energy reaches its maximum at $t = \sqrt{s}/2\kappa$ (in light-cone coordinates) when the string is fully extended and the quarks change their direction of motion. Beyond $t = 2\sqrt{s}/\kappa$, the system returns to its original positions, exhibiting stable harmonic motion. This configuration is referred to as the "hadronic yo-yo model", and its associated mass can be determined as $m_h^2 = \kappa^2 A$, where A denotes the area enclosed by one oscillation [38].

In the case where $m_T^2 > 0$, where $m_\perp^2 = m^2 + p_x^2 + p_y^2 = E^2 - p_z^2 = \kappa^2((\Delta z)^2 - (\Delta t)^2)$ is the mass shell for the hadron being produced. The creation of quark-antiquark $(q_j \bar{q} j)$ pairs with flavor f cannot happen at a single point vertex. This is because the energy necessary for their generation must be sourced from the string itself. Instead, the pair has the capability to tunnel between points associated with a string length of mTf/κ, see Fig.1.11.

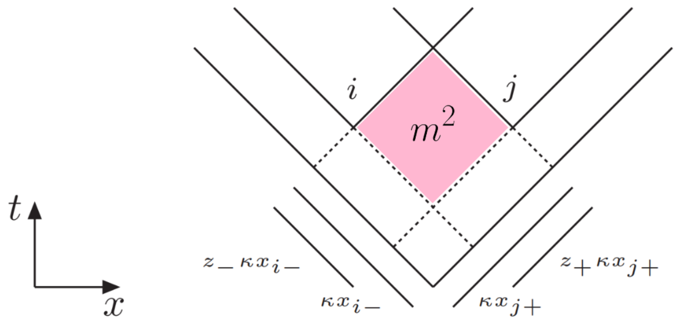

Figure 1.11: The string breaks at vertices i and j, which have lightcone coordinates as shown. The fraction of the remaining lightcone momentum taken away by hadron production is denoted as $z^{\pm}$ [39].

The total probability for an event to occur can be represented as the product of $n-1$ probabilities for the breakup vertices, combined with n delta functions that account for the masses of the hadrons in the transverse direction. The solution to this can be described using a fragmentation function $f(x)$, where x denotes the fraction of the remaining lightcone momentum that the newly formed hadron carries. For iterations to the left/right, the new hadron carries a fraction of $E \pm p_x$.

$$f(x) \propto \frac{1}{x}(1-x)^a \exp\left(-\frac{bm_\perp^2}{x}\right) \tag{1.10}$$

where a and b are two free parameters. Hence, after applying the WKB approximation, the production probability for this tunneling process is proportional to

$$\exp\bigl(-\pi m_\perp^2/\kappa\bigr) = \exp\bigl(-\pi m^2/\kappa\bigr)\exp\bigl(-\pi p_\perp^2/\kappa\bigr) \tag{1.11}$$

The string fragmentation process defines the termination point of hadronization. No more energy will be available for the production of new hadrons after many decays. It is worth noting that Eq.1.11 demonstrates a rapid fall as the mass (m) grows, indicating a significant reduction in the generation of heavy quarks via the hadronization process.

In the next chapter, we will continue our investigation by addressing the models for jet reconstruction and simulation in realistic media. We will explain the Realistic Medium Evolution ($\mathrm{T_RENTo}$ + vUSPhydro) used in this project and JEWEL (Jet Evolution With Energy Loss) as a tool to simulate the process of Jet Quenching in heavy-ion collisions. With this approach, we will be closer to elucidating the underlying mechanisms and properties of the QGP, contributing to a more comprehensive and in-depth understanding of high-energy particle physics in the collisions of heavy ions.

Chapter 2

Models and Simulation Description

2.1 Models in JEWEL

Jet Evolution With Energy Loss (JEWEL) is a Monte Carlo event generator that simulates the evolution of QCD jets in heavy-ion collisions. It accounts for the interaction of partons through QCD radiation and rescattering in a medium with fully microscopic dynamics within a perturbative framework consistent with minimal assumptions. The medium scattering is described by $2 \rightarrow 2$ pQCD matrix elements, considering possible additional radiations from particle showers [34].

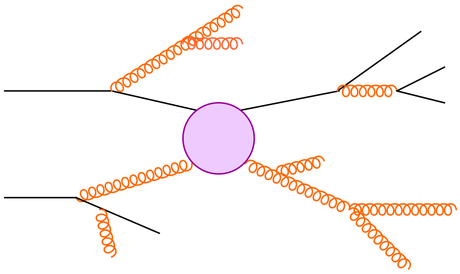

Figure 2.1: A diagram shows extra emissions from the parton shower accompanying a $2 \rightarrow 2$ matrix element representing a hard quark-gluon scattering event.

JEWEL initiates by employing PYTHIA to simulate a proton-proton collision. Subsequently, the hard scattering process takes place, where high-energy collisions capable of yielding quark-gluon particles are simulated. Following this, JEWEL simulates the evolution of quark-gluon jets as they traverse through a hot and dense medium, such as the QGP. JEWEL models the interactions between the quarks and gluons within the jet and the hot medium, calculating how the energy and momentum of the partons evolve as they interact with the medium. This is crucial for comprehending how the jets are modified while traversing the quark-gluon plasma. After the jets interact with the medium, JEWEL returns to PYTHIA for the hadronization step, which will be further elucidated in the Sec.2.3 outlining the entire simulation process employed in this study.

The models utilized by JEWEL for jet evolution occur in both a vacuum and a medium. The vacuum jet evolution model is based on a parton shower formalism, which describes the evolution of jets in terms of partonic particles. On the other hand, the medium jet evolution model employs a consistent perturbative approach that describes the interaction of jets with a hot and dense medium.

JEWEL incorporates Bjorken's plasma expansion model to describe the Plasma of Quarks and Gluons (QGP) evolution after a heavy-ion collision. This model, known as the Bjorken model, assumes that the plasma expands rapidly along the collision axis, simplifying the plasma evolution in one dimension [7].

To simulate the spread of particles in the jets as they pass through the QGP's middle, Monte Carlo simulation techniques are used, allowing the energy loss of the jets to be modeled as they interact with the plasma.

The ramification of the particles that compose the jets is performed by the use of a modeling technique known as *parton shower*, which essentially involves the spreading of particles as the jet evolves and loses energy as it passes through the QGP.

JEWEL employs the Glauber model to compute the spatial distribution of the medium formed in collisions between heavy ions. This model gives information about the system's initial energy distribution; therefore, JEWEL uses it to recreate the system's initial conditions, as we shall see in more detail in the next part.

2.1.1 Initial Conditions – Glauber

The Glauber model [40] is commonly employed within the context of JEWEL (Jet Evolution With Energy Loss) to characterize the density profile of the medium in high-energy heavy-ion collisions. The Glauber model offers insights into the spatial distribution of nuclear particles within the colliding nuclei, such as protons or nucleons, in a heavy-ion collision. It is a geometrical model based on the assumption of a constant inelastic cross section for each consecutive collision, σ_{inel} [5].

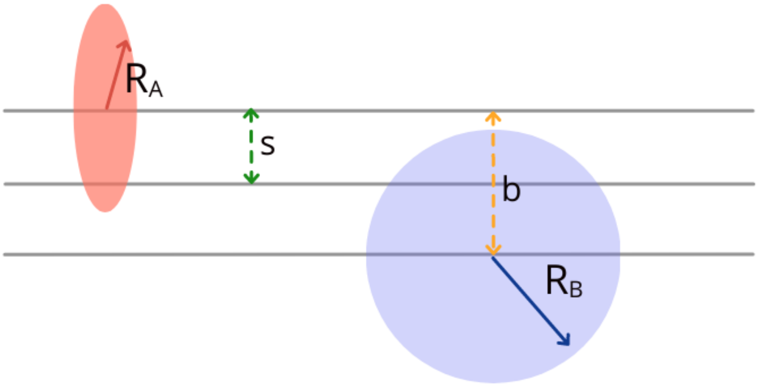

Figure 2.2: Scheme of a nucleus-nucleus collision in the rest frame of the target nucleus blue. Where b is the impact parameter, and s is the distance between the center of one nucleus and a point inside the second nucleus.

When two nuclei collide, the nucleons in the row at the transverse distance between the center of one nucleus and a point inside the second nucleus s in nucleus A clash with the nucleons in the row at $\vec{b}-\vec{s}$ in nucleus B, as shown in Fig. 2.2. This interaction of these two rows of nucleons is referred to as a row-on-row collision. When nucleus A is at location $(\vec{b}_A, z_A)$ and nucleus B is at position $(\vec{b}_B, z_B)$, we may compute the likelihood of a nucleon-nucleon collision at impact parameter b. The probability is normalized so that integration over the nuclear volume gives unity since we have defined $\int d^3r\rho_A(r) = A$ and

$$\frac{\rho_A(\vec{b}_A, z_A)}{A} d^2b_A dz_A = 1 \tag{2.1}$$

The simplest inelastic nucleon-nucleon collision probability is a delta function multiplied by the nucleon-nucleon inelastic cross section, $\sigma_{inel}\delta(\vec{b}-\vec{b}_A-\vec{b}_B)$. Since,

$$dP_{AB}(b) = \frac{\rho_A(\vec{b}_A, z_A)}{A} d^2b_A dz_A \frac{\rho_B(\vec{b}_B, z_B)}{B} d^2b_B dz_B \delta(\vec{b}-\vec{b}_A-\vec{b}_B) \tag{2.2}$$

The total probability is the integral over the normalized volume elements of both nuclei.

$$P_{AB}(b) = \frac{\sigma_{inel}}{AB} \int d^2s dz_A dz_B \rho_A(\vec{s}, z_A) \rho_B(|\vec{b}-\vec{s}|, z_B) \tag{2.3}$$

The nuclear thickness function can provide essential information for determining the density of the medium created in these collisions. This density is crucial for comprehending how quark-gluon jets interact with the hot medium during their passage. The nuclear thickness function is just the integral of the nuclear density over the longitudinal dimension:

$$T_A(b) = \int dz \rho_A(b, z) \tag{2.4}$$

The total probability, expressed in terms of b, corresponds to the integration across the volume elements of both nuclei, with normalization performed relative to AB, that is

$$P_{AB}(b) = \frac{\sigma_{inel} T_{AB}}{AB} \tag{2.5}$$

In the context of JEWEL, spatial overlap between colliding nuclei is calculated using the nuclear overlap function, as expressed in Eq. 2.6. Nuclear overlap is of crucial significance due to its direct influence on the likelihood of nuclear interactions occurring during the collision process. Increased nuclear overlap correlates with a heightened probability of significant nuclear interactions taking place.

$$T_{AB}(b) = \int d^2 s T_A(s) T_B(|\vec{b} - \vec{s}|) \tag{2.6}$$

The product $\sigma_{inel} T_{AB}(b)$ also gives the number of nucleon-nucleon collisions $N_{coll}(b) = \sigma_{inel} T_{AB}(\vec{b})$ that depends on energy since the inelastic cross section grows with $\sqrt{s}$. To obtain the number of participants in AB collision, we can start from the probability of a hadron-nucleus interaction in a nucleon-nucleon collision, since $B = 1$ e $T_{AB}(B) \rightarrow T_A(b)$.

$$P_{hA}(n, \vec{b}) = \binom{A}{n} \left[\sigma_{inel} \frac{T_A(b)}{A}\right]^n \left[1 - \sigma_{inel} \frac{T_A(b)}{A}\right]^{A-n} \tag{2.7}$$

Whose sum over all probabilities and considering $\sigma_{inel} T_A(b)/A \ll 1$

$$\sum_{n=1}^{A} P_{hA}(n, \vec{b}) = 1 - \exp(-\sigma_{inel} T_A(b)) \tag{2.8}$$

We can utilize Equation (2.8) to ascertain the count of participating nucleons in a nucleus-nucleus collision. The quantity of participants within nucleus A is directly proportional to the nuclear profile function at the transverse position s, denoted as $T_A(s)$. This is further multiplied by the summation of probabilities for a nucleon-nucleus collision at the transverse position $|\vec{b} - \vec{s}|$ within nucleus B, as defined in Equation (2.8). Similarly, the number of participants within nucleus B is determined using the same approach. Consequently, at a given impact parameter b, the count of participants i can be calculated [5].

$$
\begin{aligned}
n_{AA}(b) = \int d^2s \, \Big[T_A(s) \Big(1 - \exp\Big[-\sigma_{inel} T_B(|\vec{b} - \vec{s}|)\Big]\Big) \\
+ T_B(|\vec{b} - \vec{s}|)(1 - \exp[-\sigma_{inel} T_A(s)]) \Big]
\end{aligned}
\tag{2.9}
$$

Considering a AA collision, since this work only was simulated and used data from PbPb collision for nucleon-nucleon and given that the energy density in the transverse plane, denoted as $\epsilon_{AA}(b)$, is directly proportional to $n_{AA}(b)$. An ideal relativistic gluon gas represents the JEWEL medium [9], while quarks are neglected because the QGP is initially gluon rich, and the gluons come much faster into thermal equilibrium than the quarks. This means that the number and energy densities of gluons are related to the temperature via:

$$n(b) = d_g \frac{T^3 \zeta(3)}{\pi^2} \tag{2.10}$$

$$\epsilon(b) = d_g \frac{\pi^2 T^4}{30} \tag{2.11}$$

where d_g degrees of freedom. Then, $n \propto \epsilon^{3/4}$. JEWEL only takes interactions into account in the deconfined phase. Hence rescattering is only feasible if the local temperature is higher than the threshold temperature T_c. When a re-scattering happens, a thermal parton is produced with flavor and momentum determined by the thermal distribution of an ideal gas at the time and position of the scattering, assuming vanishing chemical potential.

While Glauber's model provided us with initial condition information on the spatial distribution of collisions in JEWEL, Bjorken's model provides us with an essential understanding of the expansion and temporal dynamics of QGP. In the next subsection, we will explore how JEWEL uses the bases provided by the Bjorken model to plot the trajectory and interaction of particle jets.

2.1.2 Bjorken Model

The initial conditions in the Landau model are set for a given laboratory time in the center-of-mass frame, where the matter is highly compressed and initially at rest. However, this description overlooks an important aspect of high-energy hadronic collisions: the delayed production of fast particles at locations further away from the collision center compared to slower particles. This phenomenon is naturally accounted for in string models of multiparticle production. Specific initial conditions must be imposed to incorporate this effect into the hydrodynamic description. Bjorken proposed and examined this concept [4].

In the context of JEWEL, the Bjorken model describes the temporal evolution of the Quark-Gluon medium that expands and develops as the particle jets pass through it. In this way, it is possible to model the interaction of the jets with the dense and hot medium, including the energy loss of the jets.

The hydrodynamic model developed by Bjorken [41] assumes that the rapidity distribution of charged particles, dN_{ch}/dy, remains constant within the midrapidity region. This implies that the central region exhibits Lorentz boost invariance along the beam axis. As a consequence, the longitudinal flow is characterized by $v_z = z/t$, with all thermodynamic quantities describing the central region dependent solely on the longitudinal proper time $\tau = \sqrt{t^2 - z^2}$ and the transverse coordinates x and y. Disregarding transverse expansion effects eliminates the dependence on the transverse coordinates, resulting in a simplified one-dimensional hydrodynamic model that can be analytically treated.

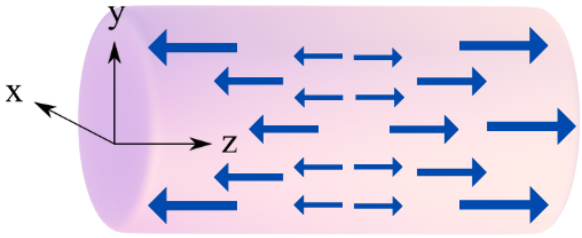

Figure 2.3: Schematic representation of a system with axial symmetry undergoing a longitudinal Bjorken scaling expansion.

Although preceding models incorporated hydrodynamics with boost invariance, Bjorken's approach offers an advantage. It introduces a formula that estimates the initial energy density achievable in relativistic heavy-ion collisions. Calculations based on this formula indicate that high-energy nuclear collisions generate matter with an energy density surpassing normal nuclear matter by at least one order of magnitude. This observation suggests the formation of quark-gluon plasma in such collisions.

In heavy-ion collisions, the four-vector velocity, normalized to unity, when the component v_ϕ is zero and assuming that the longitudinal component is much bigger than the radial component, is

$$u^\mu = (\cosh\theta, 0, 0, \sinh\theta) \tag{2.12}$$

We can write the hydrodynamic equation in cylindrical coordinates.

$$\begin{aligned} u^{\mu}\partial_{\mu} &= cosh\theta\frac{\partial}{\partial t} + sinh\theta\frac{\partial}{\partial z} \\ \partial_{\mu}u^{\mu} &= sinh\theta\frac{\partial}{\partial t} + cosh\theta\frac{\partial}{\partial z} \end{aligned} \tag{2.13}$$

Applying u_{ν} to the system's equation of motion from the energy-momentum tensor $\partial_{\mu}T^{\mu\nu} = 0$, we obtain

$$u^{\nu}\partial_{\nu}\varepsilon + (\varepsilon + P)\partial_{\nu}u^{\nu} = 0 \tag{2.14}$$

After applying the equations in Eq.(2.13), the expression becomes

$$0 = \cosh\theta\frac{\partial\varepsilon}{\varepsilon t} + \sinh\theta\frac{\partial\varepsilon}{\varepsilon z} + (\varepsilon + P)\left(\sinh\theta\frac{\partial\theta}{\varepsilon t} + \cosh\theta\frac{\partial\theta}{\varepsilon z}\right) \tag{2.15}$$

We can also obtain the following result.

$$0 = \sinh\theta\frac{\partial P}{\varepsilon t} + \cosh\theta\frac{\partial P}{\varepsilon z} + (\varepsilon + P)\left(\cosh\theta\frac{\partial\theta}{\varepsilon t} + \sinh\theta\frac{\partial\theta}{\varepsilon z}\right) \tag{2.16}$$

We can simplify the expression using light-cone variables, rapidity y, and proper time τ.

$$y = \frac{1}{2}\ln\frac{t + z}{t - z} \tag{2.17}$$

$$\tau = \sqrt{t^2 - z^2} \tag{2.18}$$

We can also express the coordinates t and z as functions of τ and y since, on the light-cone axis, we have $t = \pm z$ and $y = \pm\infty$.

$$t = \tau\cosh y \tag{2.19}$$

$$z = \tau\sinh y \tag{2.20}$$

In this way, rewriting Eq.(2.15) and Eq.(2.16) in terms of τ and y, we obtain

$$0 = \tau\frac{\partial\varepsilon}{\partial\tau} + \tanh\theta - y\frac{\partial\varepsilon}{\partial y} + (\varepsilon + P)\left(\tau\tanh\theta - y\frac{\partial\theta}{\partial\tau} + \frac{\partial\theta}{\partial y}\right) \tag{2.21}$$

$$0 = \tau \tanh\theta - y\frac{\partial P}{\partial \tau} + \frac{\partial P}{\partial y} + (\varepsilon + P)\left(\tau\frac{\partial \theta}{\partial \tau} + \tanh\theta - y\frac{\partial \theta}{\partial y}\right) \tag{2.22}$$

Utilizing the conservation of the baryon number, we can start from the following relation to obtain another equation.

$$\partial^{\mu}(n_{bar}u_{\mu}) = 0 \tag{2.23}$$

$$\begin{aligned} 0 &= u_{\mu}\partial^{\mu}n_{bar} + n_{bar}\partial\mu u_{\mu} \\ &= \cosh\theta\frac{\partial n_{bar}}{\partial t} + \sinh\theta\frac{\partial n_{bar}}{\partial z} + n_{bar}\left(\sinh\theta\frac{\partial\theta}{\partial t} + \cosh\theta\frac{\partial\theta}{\partial z}\right) \end{aligned} \tag{2.24}$$

This results in an equation very similar to Eq.(2.15) with ε and $(\varepsilon + P)$ replaced by n_{bar}.

$$0 = \tau\frac{\partial n_{bar}}{\partial \tau} + \tanh\theta - y\frac{\partial n_{bar}}{\partial y} + n_{bar}\left(\tau\tanh\theta - y\frac{\partial\theta}{\partial\tau} + \frac{\partial\theta}{\partial y}\right) \tag{2.25}$$

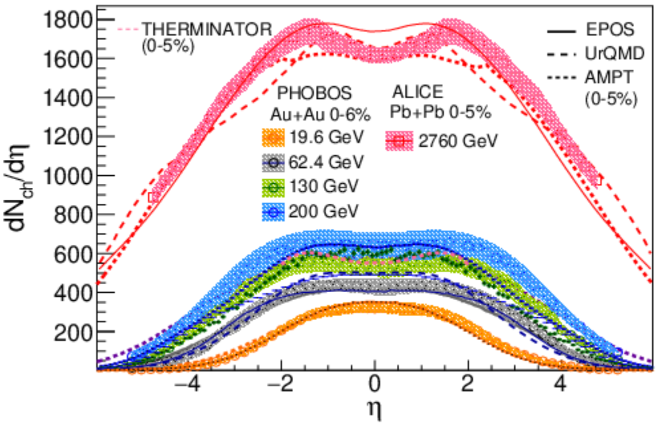

Figure 2.4: Comparison of selected experimental $dN_{ch}/d\eta$ distributions of measured in AuAu and PbPb collisions with calculations performed with the PYTHIA, AMPT, UrQMD, EPOS, and THERMINATOR models [42].

Bjorken's initial condition assumes that $\theta(y, \tau_0) = y$, the initial system after the ions interact looks the same, regardless of rapidity. The motivation for this assumption stems from the belief that a Lorentz boost along the beam axis should not impact the rapidity distribution of particles produced in the mid-rapidity region. Consequently, the quantity $\left.\frac{dN}{dy}\right|_{y\sim 0}$ remains constant. This results in a distinct central plateau structure, wherein all thermodynamic quantities depend on the proper time τ and the transverse coordinates. Figure 2.4 visually represents this phenomenon.

This implies that $\partial\theta/\partial y = 1$, $\partial\theta/\partial\tau = 0$ and $\tanh\theta - y = 0$. Then Eqs. (2.15), (2.16) and (2.25) reduce to

$$0 = \tau\frac{\partial\varepsilon}{\partial\tau} + \varepsilon + P, \tag{2.26}$$

$$0 = \frac{\partial P}{\partial y}, \tag{2.27}$$

$$0 = \tau\frac{\partial n_{bar}}{\partial\tau} + n_{bar} \tag{2.28}$$

The solution to the equation above is

$$n_{bar}(\tau) = n_{bar}(\tau_0)\frac{\tau_0}{\tau} \tag{2.29}$$

Where τ_0 represents the initial proper time when the system attains local equilibrium, thus establishing the validity of the hydrodynamic solution. The hydrodynamic evolution relies on Bjorken expansion, which simplifies by disregarding transverse expansion and employing an ideal gas equation of state, leading as in [9].

$$\epsilon(b,\tau) = \epsilon(b,\tau_i)\left(\frac{\tau}{\tau_i}\right)^{-4/3} \tag{2.30}$$

$$T(b,\tau) \propto \epsilon^{1/4}(b,\tau_i)\left(\frac{\tau}{\tau_i}\right)^{-1/3} \tag{2.31}$$

where $\epsilon(b,\tau_i)$ is the initial energy density.

The entropy density equation, which shares the same form as the baryon density equation, consequently possesses the solution.

$$s(\tau) = s(\tau_0)\frac{\tau_0}{\tau} \tag{2.32}$$

Starting from entropy, we can obtain by applying $T\partial_\nu$ to (su^ν) and utilizing the definition of the speed of sound in a fluid, $VdP/dE = c_s^2$:

$$\partial_\nu \ln s = \frac{1}{c_s^2}\partial_\nu \ln T \tag{2.33}$$

$$
\begin{aligned}
0 &= u^\mu \partial_\mu s + s \partial_\mu u^\mu \\
&= \partial_\mu u^\mu + u^\mu \partial_\mu \ln s \\
&= \partial_\mu u^\mu + \frac{1}{c_s^2} u^\mu \partial_\mu \ln T
\end{aligned} \tag{2.34}
$$

Using light-cone coordinates, we can obtain the following solution:

$$
0 = c_s^2 + \tau \frac{\partial \ln T}{\partial \tau} \tag{2.35}
$$

$$
T(\tau) = T(\tau_0) \left(\frac{\tau_0}{\tau} \right)^{c_s^2} \tag{2.36}
$$

It is noteworthy that, given the exclusively longitudinal expansion, any geometric characteristic of the initial condition remains preserved throughout the evolution process in the JEWEL simulation.

2.2 Realistic Medium Evolution Models

The quark and gluon plasma can be described in terms of hydrodynamics, which describes the behavior of fluids on a large scale. In addition to other physical effects, the simulation of a hydrodynamic system like the QGP considers viscosity, energy flow, and the system's own expansion. More can be learned about the QGP, including information about the quark-gluon state transition, the nature of the coupling, and other events related to particle production, if we examine a realistic model in collisions of charged particles.

In this work, we determine the system's initial conditions produced in collisions of relativistic heavy-ion collision using the T_RENTo model. T_RENTo is a well-known code that makes it possible to determine the spatial distribution of energy density after a collision. Some prerequisites must be met to use the v-USPhydro method to simulate hydrodynamics because it can accurately depict how the hot plasma of quarks and gluons changes over time and space while considering crucial parameters like plasma expansion and viscosity. The v-USPhydro is an ideal candidate for the system's evolution. T_RENTo and v-USPhydro were used to define the initial conditions and medium development, respectively, to investigate the properties of the plasma QGP and, in particular, the interaction with the particle jets created in these collisions. As a result, theoretical understanding of particle physics and high-energy nuclear physics has advanced.

The main difference between Glauber's model and T_RENTo is that the latter considers the distribution of nuclei thickness along the collision axis, taking into account the internal structure of nuclei and their nuclear interactions.

2.2.1 Initial Conditions – T$_R$ENTo

The Thickness Event-by-event Nuclear Topology (T$_\mathrm{R}$ENTo)[43] is a new parametric initial condition model for high-energy nuclear collisions based on eikonal entropy deposition via a "reduced thickness" function. It generates nucleus-nucleus eccentricity harmonics consistent with experimental flow constraints and is compatible with ultra-central uranium-uranium data, unlike existing models that include binary collision terms.

The model assumes that the eikonal superposition of the thickness functions T_A and T_B produces entropy through a scalar field $f(T_A, T_B)$ where f is postulated as a generalized average, called reduced thickness.

$$\frac{dS}{dy} \propto f(T_A, T_B) \doteq T_R(p; T_A, T_B) = \left(\frac{T_A^p + T_B^p}{2}\right)^{\frac{1}{p}} \tag{2.37}$$

where p is the free continuous parameter that interpolates between qualitatively different physical paths for entropy formation. In order to visualize this, consider a pair of nucleon participants colliding with a non-zero impact parameter, as depicted in Fig. 2.5.

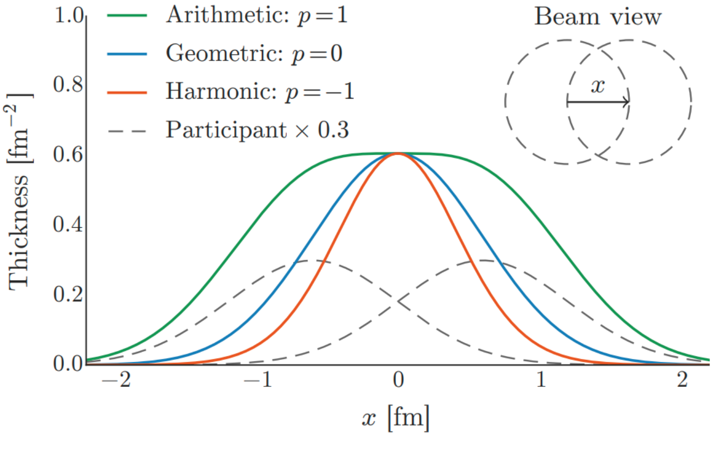

Figure 2.5: A pair of nucleon participants' thickness has been reduced. As depicted in the top right, the nucleons clash with a nonzero impact parameter along the x-axis. The grey dashed lines are one-dimensional cross sections of the participant nucleon thickness functions T_A, T_B, while the colored lines (green, blue, orange) represent reduced thickness T_R for $p = 1, 0, -1$ [43].

Consider a collision between two nuclei A and B with an impact parameter b along the x-axis and nuclear densities $\rho_{A,B} = \rho_{parton}(x \pm b/2, y, z)$, and suppose that the integral $\int dz \rho_{parton}$ has a closed form or can be numerically evaluated, allowing the parton thickness functions to be determined. The probability of collision of the parton is

$$P_{AB} = 1 - \exp\left[-\sigma_{gg} \int dx\, dy \int dz\, \rho_A \int dz\, \rho_B\right] \tag{2.38}$$

where the integral in the exponential is the overlap integral of the parton thickness functions and σgg is an effective parton-parton cross-section set to equal the experimental inelastic nucleon-nucleon cross-section σNN.

Similar to Glauber's model, the collision probability can be tackled using the fluctuating thickness for each parton as:

$$T_{A,B}(x, y) = w_{A,B} \int dz\, \rho_{A,B}(x, y, z) \tag{2.39}$$

where $w_{A,B}$ are separate random weights drawn from a gamma distribution with a unit mean,

$$P_k(w) = \frac{k^k}{\Gamma(k)} w^{k-1} e^{-kw} \tag{2.40}$$

These gamma weights incorporate extra multiplicity fluctuations to recreate the huge fluctuations found in experimental nucleus-nucleus collisions. To best suit the data, the shape parameter k can be tuned: tiny values ($0 < k < 1$) correlate to significant multiplicity fluctuations, whereas big values ($k \gg 1$) suppress variations.

In high-energy collisions, there exists an important parameter known as centrality, which pertains to the measurement of how central or peripheral the collision between atomic nuclei or subatomic particles is. This classification is utilized to elucidate how the collision's geometry impacts the behavior of the produced matter.

Centrality categories, such as $0-10\%$, $20-30\%$, and up to $60-80\%$, are determined based on the percentage of overlap between the colliding nuclei. For instance, in a $0-10\%$ collision, the nuclei collide in a highly central manner, exhibiting substantial overlap, whereas in a $60-80\%$ collision, the overlap is significantly reduced, rendering it less central.

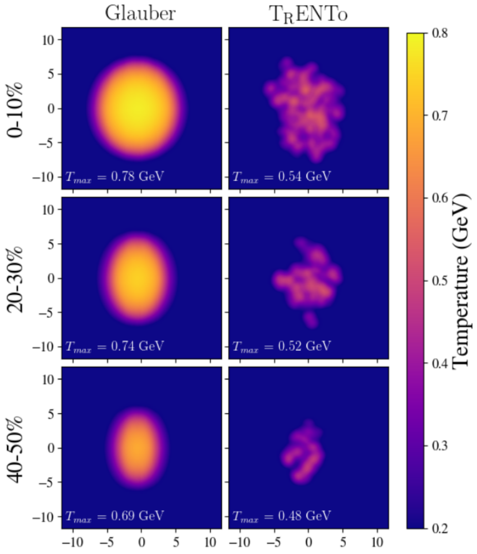

Figure 2.6: Initial temperature conditions for some centralities using the Glauber and T$_{\mathrm{R}}$ENTo models. Length scale in fm and proper time scale in fm/c.[36]

2.2.2 v-USPhydro

The v-USPhydro is a numerical code for relativistic hydrodynamics developed to investigate viscosity's effects on the dynamics of heavy-ion collisions. It utilizes the Smoothed Particle Hydrodynamics (SPH) algorithm, a 2+1-dimensional fluid simulation technique suitable for handling problems involving free surfaces, deformable boundaries, and large deformations without a mesh structure.

This model has the capability to simulate the evolution of the quark-gluon plasma (QGP) formed in heavy-ion collisions, taking into account the effects of viscosity. It allows the study of the QGP dynamics and the investigation on how its viscosity can influence plasma properties.

The Eulerian approach uses a predefined grid, and the Lagrangian method, which discretizes the fluid into individual particles and records their location and velocity over time, is often used for solving hydrodynamic equations. In the v-USPhydro framework, the well-known Lagrangian approach known as SPH is applied, providing an efficient framework for solving the Equations of Motion.

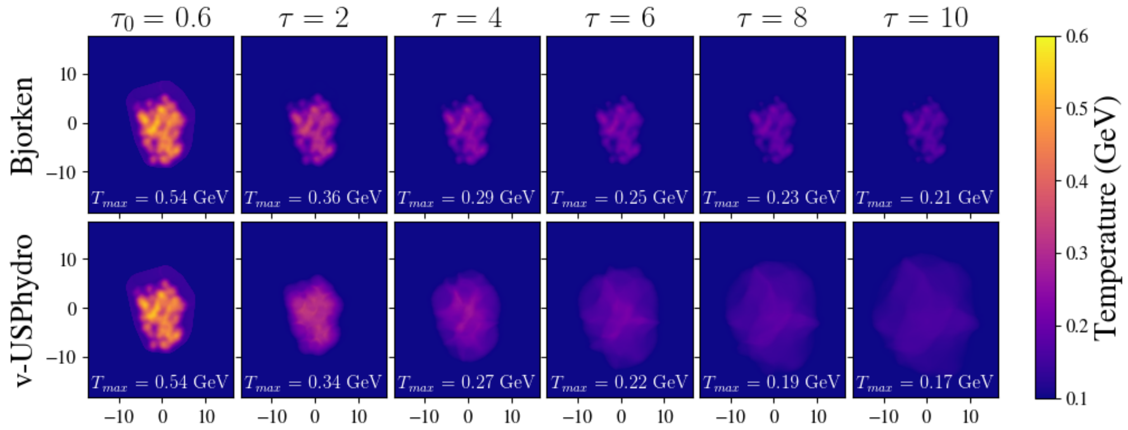

Figure 2.7: The temperature evolution is shown in the top row for Bjorken's expansion and in the bottom row for v-USPhydro's expansion, considering a random TRENTo central $(0-10\%)$ initial profile at different proper time steps (columns) for PbPb collisions at 5.02 TeV. The maximum temperature in each panel is indicated in white, the length scale is in fm, and the proper time scale is in fm/c [36].

Dissipative hydrodynamics is an extension of ideal hydrodynamics that considers the fluid's viscosity. The causal dissipative hydrodynamics equations include viscosity terms that describe the dissipation of energy and momentum in the fluid. Viscosity can be divided into two categories: shear viscosity, which describes the dissipation of momentum perpendicular to the velocity gradient, and bulk viscosity, which describes energy dissipation due to volume variations. Volume viscosity is also known as mass viscosity or bulk viscosity.

In summary, the model is based on a formulation of causal dissipative relativistic hydrodynamics in two spatial dimensions, which includes the conservation equations for energy, momentum, and baryon number, along with evolution equations for shear and bulk viscosities. The equations are numerically solved using a finite difference method in a Cartesian coordinate system. The model also incorporates an equation of state that describes the relationship between pressure, energy, and entropy density of the fluid.

The conservation equation for energy-momentum, which describes how energy and momentum are conserved in a hydrodynamic system, is given by:

$$T^{\mu\nu} = \epsilon u^{\mu}u^{\nu} - (p+\Pi)\Delta^{\mu\nu} \tag{2.41}$$

In this equation, $T^{\mu\nu}$ is the energy-momentum tensor, ϵ is the energy density, u^{μ} is the four-velocity of the fluid element, p is the thermodynamic pressure, Π represents the bulk viscous pressure, and $\Delta^{\mu\nu} = g^{\mu\nu} - u^{\mu}u^{\nu}$ is the projection and $g^{\mu\nu}$ is the metric tensor.

The first term on the right-hand side represents the ideal fluid part, where the energy-momentum is determined solely by the energy density and the four-velocity. The second term, $-(p+\Pi)\Delta^{\mu\nu}$, accounts for the viscous effects and represents the deviation from the ideal fluid behavior. The bulk viscous pressure Π captures the dissipative effects due to variations in the volume of the fluid element.

When combined with other equations of state and transport equations, this conservation equation forms a system of equations that governs the evolution of the hydrodynamic system over time. Solving these equations allows one to study the flow patterns, dissipative effects, and the system's overall behavior under different conditions.

The equation presented below is the evolution equation for viscosity, which describes how viscosity evolves over time. This equation is one of the constitutive equations in viscous hydrodynamics and is utilized to elucidate the influence of viscosity on the evolution of a hydrodynamic system.

$$\tau\Pi(D\Pi+\Pi\theta)+\Pi+\zeta\theta=0 \tag{2.42}$$

In this equation, τ represents the relaxation time coefficient required to preserve causality, D represents the covariant derivative, θ signifies the expansion scalar and ζ corresponds to the bulk viscosity coefficient.

The equation states that the change in bulk viscous pressure Π is determined by the product of the relaxation time τ and the sum of the covariant derivative of the bulk viscous pressure $D\Pi$ and the product of the bulk viscous pressure and the expansion scalar $\Pi\theta$. The terms Π and $\zeta\theta$ represent the contributions of the bulk viscosity and shear viscosity, respectively, to the system's evolution.

By solving this evolution equation, in conjunction with other governing equations of the hydrodynamic system, we can gain insights into how viscosity influences the system's behavior as it evolves over time.

In the Smoothed Particle Hydrodynamics (SPH) approach, a conserved reference density current $J^\mu=\sigma u^\mu$ is introduced, where σ represents the local density of a fluid element in its rest frame. As the fluid undergoes flow, the density follows the equation $D\sigma+\sigma\theta=0$, which, in hyperbolic coordinates, can be written as $\partial_\mu(\tau\sigma u^\mu)=0$. The equations of motion in the SPH model can be written in terms of this reference density, governing the evolution of the four-velocity u^μ and the reference density σ. In terms of this reference density, the equations of motion employed in this paper can be expressed as in [44].

$$\begin{aligned}
\gamma\frac{d}{d\tau}\left(\frac{(\varepsilon+p+\Pi)}{\sigma}u^{\mu}\right) &= \frac{1}{\sigma}\partial^{\mu}(p+\Pi),\\
\gamma\frac{d}{d\tau}\left(\frac{s}{\sigma}\right)+\left(\frac{\Pi}{\sigma}\right)\frac{\theta}{T} &= 0,\\
\gamma_{\Pi}\left(\frac{\Pi}{\sigma}\right)+\frac{\Pi}{\sigma}+\frac{\zeta}{\sigma}\theta &= 0
\end{aligned} \tag{2.43}$$

In the context of this study, the variables s, ε, and σ represent the densities of entropy, energy, and local fluid, respectively. The quantities p and T correspond to the pressure and temperature of the system. Additionally, the fluid expansion rate $\theta = \partial_{\tau}\mu(\tau u^{\mu})$ is also essential for the description and analysis of the system.

SPH uses Lagrangian coordinates and a normalized distribution function to reconstruct hydrodynamic fields at specific space-time points. The kernel function with finite support and a cutoff parameter, h, controls the accuracy and number of particles needed. The choice of h determines the preservation of the initial structure and is limited by computational time. The kernel function in hyperbolic coordinates for boost-invariant hydrodynamics is normalized as:

$$\int W[\mathbf{r};h]d^2\mathbf{r} = 1 \tag{2.44}$$

Where **r** is a Lagrangian coordinate, and the h parameter is a length scale that indicates the kernel's width and creates a cutoff for modes with shorter wavelengths [44].

In the Smoothed Particle Hydrodynamics (SPH) method, the reference density in the laboratory frame is represented using Lagrangian coordinates as:

$$\tau\gamma\sigma \to \sigma^{\star}(\mathbf{r},\tau) = \sum_{\alpha=1}^{N_{SPH}} \nu_{\alpha} W[\mathbf{r}-\mathbf{r}_{\alpha}(\tau);h] \tag{2.45}$$

The normalization of the kernel implies that the integral of the reference density in the transverse plane is a constant, given by $\int d^2 r\sigma^{\star} r(\tau) = \sum_{\alpha}^{N_{SPH}} \nu_{\alpha}$. As a result, it is natural to interpret ν_{α} as a conserved quantity associated with the Lagrangian coordinate $(r_{\alpha}(\tau)$, while σ^{α} represents a summation of small piece-wise distributions $\nu_{\alpha}W[r - r_{\alpha}(\tau);h]$, known as "SPH particles" [44].

For an extensive quantity represented by $a(\mathbf{r},\tau)$, the SPH method provides the following description:

$$a(\mathbf{r},\tau) = \sum_{\alpha=1}^{N_{SPH}} \nu_\alpha \frac{a(\mathbf{r}_\alpha(\tau))}{\sigma^\star(\mathbf{r}_\alpha(\tau))} W[\mathbf{r} - \mathbf{r}_\alpha(\tau); h] \tag{2.46}$$

In addition to the position and velocity mentioned earlier in the text, which is utilized in the SPH method, various other dynamic variables can be obtained from the given quantity, such as entropy and bulk viscosity associated with the α-th SPH particle.

These equations of motion can be solved in v-USPhydro. The advantage of the SPH method in hydrodynamics lies in transforming the coupled, nonlinear partial differential equations in the Eulerian view into a set of nonlinear ordinary coupled differential equations for the Lagrangian variables. Additionally, there is no need to impose extra conditions on the dynamical fields at very low temperatures. In fact, without bulk viscosity, the model demonstrates that the code precisely matches the analytical solution for 2+1.

2.3 Simulation Description

2.3.1 Overview

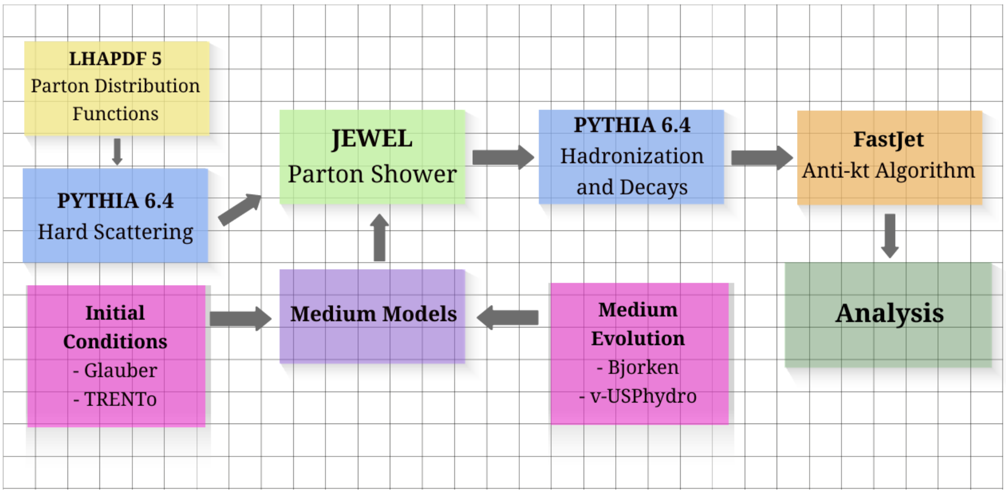

Figure 2.8: Illustration of the simulation steps and the subsequent computation of observables.

Jet simulation offers an important role in advancing our understanding of the physical phenomena that occur during relativistic heavy-ion collisions. In this chapter, we will examine in detail the fundamental components of the simulation used in this study. We will start by describing how the initial conditions apply, established from the contributions of the Glauber and $\mathrm{T_RENTo}$ models, the hadronization, and parton distribution software. In addition, it will be revealed how the reconstruction of jets occurs using algorithms in the JEWEL framework and how the analyses were written. This reconstruction performed by JEWEL will have default medium evolution, bjorken, and mainly in realistic medium configurations using v-USPhydro. The sequence used in the simulations performed in this work, as illustrated in Fig.2.8, is:

1. PYTHIA 6.4 [8] is used to generate a hard scattering between nucleons for a given nuclear mass.
2. The event continues from an initial vertex with the parton development of the scattering, as described in Section 1.3.1 with PDFs given by the LHAPDF 5 [45].
3. For proton-proton collisions, the parton shower is developed without interactions with the medium in a vacuum.
4. The parton shower in heavy-ion collision: for JEWEL's default medium is a simple Glauber+Bjorken (Sections 2.1.1 and 2.1.2), and for this work, we also used the more realistic alternatives $\mathrm{T_RENTo}$+v-USPhydro (Sections 2.2.1 and 2.2.2).
5. When the partons reach on-shell mass or depart the medium, they are returned to PYTHIA for hadronization and decay, as described in Section 1.5. This produces the event's final hadronic configuration.
6. The jets are reconstructed by the Anti-k$_T$ algorithm provided by the FastJet package [46] in a Monte Carlo event developed by the Rivet 3.1.4 framework [47], finally obtaining the desired observables.

The initial connection between JEWEL 2.2.0 and the new medium profiles was first explored and examined in Sec.2.1. Unlike the default configuration of JEWEL, the new medium profiles are characterized by a discrete collection of points denoted as $T(x, y, \tau)$. The spatial grid employed possesses a dimension of 0.15 fm, while the temporal aspect evolves in increments of 0.1 fm/c. An essential aspect of this framework is the interpolation of the grid, which occurs bicubically in space and linearly in time, as highlighted in [48].

The inclusion of user-defined critical temperature (T_C) serves as a boundary that constrains the scope of medium interactions. In practical terms, when the local temperature $T(x, y, \tau)$ falls below T_C, it indicates the absence of a QGP within that region. Consequently, no interactions are computed, and the presence of a mixed phase is not accounted for.

In addition to the critical temperature, the user can change another free parameter. The Debye mass discussed briefly in Chap. 1 sec.1.3.1 uses by JEWEL with a free scale parameter s_μ by

$$\mu_D(T) \equiv 3T \Rightarrow \mu_D(T) = 3s_\mu T \tag{2.47}$$

The parameter s_μ was determined to be 0.9 by modifying it to represent single-inclusive hadron suppression at RHIC; this value is identical to that in the default release of JEWEL [34]. After calculating nuclear factor modification R_{AA} for PbPb (0-10%) at $\sqrt{s_{NN}} = 5.02$ TeV for values of $s_\mu = 0.9$, 1.0, and 1.1 as well as for $T_C = 0.15$, 0.16, and 170 MeV [34], the best values for these parameters were determined using also the data from the ATLAS experiment [49]. The optimal tuning for the JEWEL + T$_R$ENTo + v-USPhydro setup was $s_\mu = 1.1$ considering recoils and $s_\mu = 1.0$ without recoils, and $T_C = 170$ MeV for both.

The vUSPhydro medium profiles used are differentiated across distinct centrality classes depending on the number of soft-charged pions and their accompanying properties [11]. In contrast, the Glauber media, which is the default in JEWEL, has its centralities specified by user-defined parameters. This distinction shows the differences in approach between the two mediums: v-USPhydro categorizes media profiles according to particular multiplicity classes, whereas JEWEL's default setup allows users to determine the centralities of its Glauber media profiles.

2.3.2 Refining the Simulation Model

Several modifications have been implemented in the realistic model employed within this study in recent years. One of the key changes pertains to the inclusion of transverse velocity. Previously, the scattering center possessed only longitudinal velocity. Consequently, an addition of velocity within the transverse plane was implemented. This enhancement enables the extraction of transverse momentum, denoted as $u(x, y, \tau)$, in addition to local temperature, represented as $T(x, y, \tau)$, when utilizing the v-USPhydro. Furthermore, adjustments were made to the effective density. Previously, it could be defined as:

$$n_{eff}(x,y,z,\tau) = \frac{n_0}{\gamma} \tag{2.48}$$

where n_0 is the density of a gluon gas and $\gamma = 1/\sqrt{1-v_z^2} = \cosh y$. As the original JEWEL use that scattering center 4-velocity is $u = (\gamma, 0, 0, u_z)$, now we can write $u = (\gamma, u_x, u_y, u_z)$ [50]. Therefore, as the effective density in [51]:

$$n_{eff}(x,y,z,\tau) = \frac{n_0}{\gamma} \rightarrow n_{eff}(x,y,z,\tau) = \frac{p^{\mu}u_{\mu}n_0}{p_0} \tag{2.49}$$

where u_{μ} is the transverse flow velocity, $p^m u$ is the parton four-momentum, and the p_0 is the initial momentum of the parton.

The initial vertex of the hard scattering was the subject of the second recent alteration. The initial technique used in JEWEL included restrictions on the vertex selection, only allowing it to be taken from the overlap zone of colliding nuclei. This term should not be used in T$_R$ENTo [43]. Instead, we chose the vertex using the probability distribution with T^4 proportional to the initial energy density in the transverse plane. Additionally, only locations where the local temperature was above the freeze-out temperature are included in the permitted zone [50].

From equations (2.10) and (2.11), it can be observed that the temperature of the medium directly influences how the evolution of the medium occurs in the Bjorken model, which is the hydrodynamics framework originally employed by JEWEL. The maximum temperature (T_{max}) of the medium used in JEWEL is a constant determined by selecting the maximum temperature at a point within the medium, thereby configuring a constant maximum effective density (n_{max}) dependent on this maximum temperature value. In our realistic medium model, this maximum temperature is not selected from a single point but rather from the average maximum temperature across the medium.

In addition to the maximum temperature, the rapidity or average rapidity (y) used by JEWEL was also constant and fixed. A modification was made to allow for the selection of rapidity based on the experimental value comparison of interest.

The parameters employed in the simulation for JEWEL, the medium, and T$_R$ENTo are detailed in Appendix A. In addition to the possible parameters described therein, the simulations allow for the selection of collision centrality. Centrality in heavy-ion collisions indicates the degree of overlap or impact between the nuclei of the colliding ions. It is employed to categorize heavy-ion collisions into different classes based on how central or peripheral the collision was. These centrality classes are expressed as percentages, such as those utilized in this study, including 0-10%, 10-20%, 20-30%, 30-40%, 40-50%, and 50-60%. Within these categories, the percentage signifies the fraction of the most central collisions relative to the total number of observed collisions.

Table 2.1: Specificities of the simulations for each observable jet studied. For all models, the default JEWEL (Glauber+Bjorken) and $\mathrm{T_RENTo}$+vUSPhydro for the most realistic medium.

Observable	Centrality (%)	Kinematics cuts	Jet radius R
R_{AA}	0-10, 10-20, 20-30, 30-40, 40-50, 50-60	$p_T > 20$ GeV $\lvert y\rvert < 2.8$ $\lvert\eta\rvert < 3.2 - R$	0.2, 0.3, 0.4, 0.6, 0.8, 1.0
x_j	0-10, 10-20, 20-30, 30-40, 40-50, 50-60	$p_T > 20$ GeV $\lvert\eta\rvert < 1.2$	0.2, 0.3, 0.4, 0.6, 0.8, 1.0
M_{jet}	0-10	$p_T > 20$ GeV $\lvert\eta\rvert < 0.9 - R$	0.2 and 0.4
$h\text{-}jet$	0-10	$5 < p_T < 100$ GeV $\lvert y\rvert < 2.8$ $\lvert\eta\rvert < 3.2 - R$	0.2, 0.4, 0.5

The Tab.2.1 shows the observables simulated, covering aspects such as kinematic constraints and centrality, specifically tailored for each observable. Throughout this study, all simulations consistently adopted a center of mass energy of 2.76 TeV and 5.02 TeV operating in JEWEL mode that incorporates recoils, as Section 2.3.3 explains.

After an overview of the simulation and its stages, in the upcoming sections, we will delve into understanding how jet reconstruction takes place in the simulations conducted in this study. This will be achieved through the implementation of algorithms such as the anti-k$_T$, along with techniques employed to replicate the system's physical details, including the thermal subtraction method.

2.3.3 Jet Reconstruction

As discussed previously in Chapter 1, jets are a consequence of the confinement property of strong interactions. This phenomenon arises because the energy of partons can undergo several successive transformations, including evolution, fragmentation, hadronization, and final-state decay, ultimately resulting in a collimated collection of hadrons in an azimuthal (pseudo)rapidity space. This collimated collection is what we define as a jet.

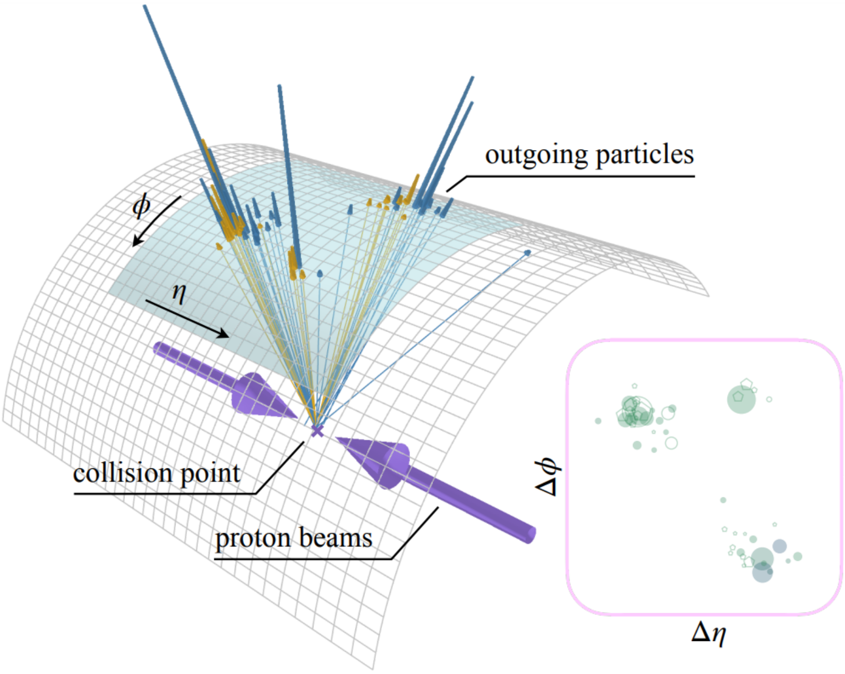

Figure 2.9: Illustration of jet reconstruction at the CERN LHC using JetClass [52]. Complex particle detector systems measure these outgoing particles, and jets can be reconstructed from measured particles [53].

Convergence between theory and experimental evidence is essential to establish a solid definition of a jet, which consists of sets of guidelines that prescribe how particles in the final state are organized to form jets. These specific sets of rules, which guide this clustering process, are incorporated into the jetting algorithms. They must, in turn, conform to a set of general properties [54], which are formally known as the "*Snowmass Accord of 1990*":

- Simple to implement in an experimental analysis;
- Simple to implement in the theoretical calculation;
- Defined at any order in perturbation theory;
- Yields finite cross sections at any order of perturbation theory;
- Yields a cross-section that is relatively insensitive to hadronization;

These properties were developed to ensure that the jet algorithms were consistent, reliable, and applicable in experimental and theoretical analyses.

Hard partons are expected to experience multiple collinear splittings or soft emissions in both perturbative and non-perturbative regimes, some of which remain poorly understood. Therefore, it is advisable to favor algorithms capable of yielding final results that remain unaffected by these emissions [55].

For infrared safeness:

> *In any n-parton configuration, adding an infinitely soft parton does not affect the observable at all*

And for collinear safeness:

> *In any n-parton configuration, replacing any massless parton with an exactly collinear pair of massless partons does not affect the observable at all.*

If all requirements are met, the method is said to be infrared and collinear (IRC) safe. Various techniques were rejected or altered to ensure IRC safety since it is a helpful tool in theoretical pQCD calculations and offers a better framework for examining detector physics, such as noise and granularity [55].

In the next section, we will see the main method of particle combination used in the reconstruction of jets in high-energy physics experiments, particularly collisions at the LHC.

Anti-k$_T$

Inspired by the Snowmass agreement, the algorithm characterizes the momentum of a jet in terms of the momenta of its constituent particles as shown below for transverse energy, pseudorapidity, and azimuth, as[55]:

$$\begin{aligned} E_{Tjet} &= \sum_{i \in jet} E_{Ti}, \\ \eta_{jet} &= \sum_{i \in jet} E_{Ti}\eta_i / E_{Tjet}, \\ \phi_{jet} &= \sum_{i \in jet} E_{Ti}\phi_i / E_{Tjet} \end{aligned} \tag{2.50}$$

The distance between a pair (i, j) can be defined as $\Delta R_{ij}^2 = (y_i^2 - y_j^2)^2 + (\phi_i^2 - \phi_j^2)^2$ and for every pair of particles we can define the distance:

$$d_{ij} = \min(p_{Ti}^2, p_{T,j}^2)\frac{\Delta R_{ij}^2}{R^2} \quad \text{and} \quad d_{iB} = p_{Ti}^2 \tag{2.51}$$

After calculating all possible d_{ij} and d_{iB}, the algorithm compares the two values; if $\min\{d_{ij}\} < \min\{d_{iB}\}$ recombine i and j into a new particle and return to the first step, however, if $\min\{d_{ij}\} > \min\{d_{iB}\}$ jet i is complete and remove it from the particles' list returning to the first step. This process is repeated until all jets are created. All opening angles within each jet are smaller than R in this context, but all opening angles between jets are bigger than R.

In Figure 2.10 it can be seen that the algorithm results in circular jets with well-defined boundaries even when an overlap occurs.

The jet radius parameter, denoted as R, controls the spatial extent of the reconstructed jets. It is anticipated that altering the value of R will influence the incorporation of initially scattered energy stemming from parton fragmentation processes. As a result, this alteration offers valuable insights into the mechanisms of jet quenching and potential medium modifications and provides constraints that could potentially refine models [36]. Tab.2.1 shows which R values were used in each observation, essentially varied in $0.2, 0.3, 0.4, 0.5, 0.6, 0.8, 1.0$.

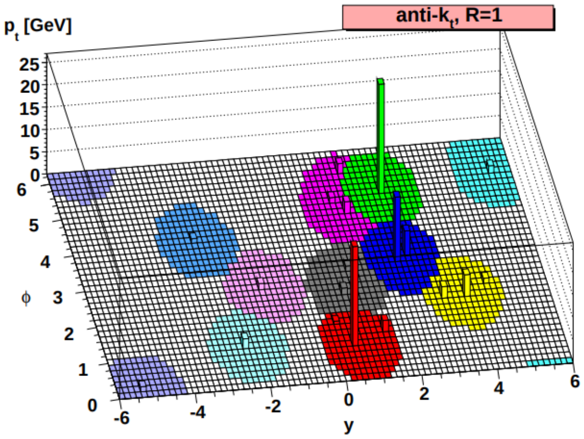

Figure 2.10: Partonic event with random soft particles clustered with anti-k$_T$ algorithms for $R = 1$. Jets are represented in various colors [56].

The anti-k$_T$ algorithm plays a key role in accurately identifying jets and understanding the strong interactions that lead to the formation of these structures. However, correcting certain unwanted energy effects in the simulation is still necessary, particularly in situations where the hot and dense medium can influence the results. Thermal subtraction is a technique that aims to correct these effects, as we will see in the next section.

Thermal Subtraction

In JEWEL, as seen in Section 2.1.2, the medium details, as 4-velocity, temperature, and density, are supplied to the code by the Bjorken hydrodynamic model that describes the longitudinally invariant expansion of an ideal gas of quarks and gluons. The location in the medium where the interactions between particles occur is defined as the "scattering center". Such centers are used to provide JEWEL with the phase density of the medium necessary to simulate the propagation of jets in a medium such as the QGP. The density of scattering centers at any point in space-time is calculated from the initial density determined by hydrodynamics. When an interaction occurs, a scattering center is generated with a moment given by the thermal distribution at the local temperature.

In Section 1.3.1, we saw that there is a parton shower in the collision system. As partons evolve in the medium, they interact with the scattering centers via the $2 \to 2$ process, which triggers new recoiling partons generated in the simulation. These recoils evolve freely until they are hadronized without suffering interactions in between. Thus, the contributions of the parton shower from the medium response in the final state cannot be distinguished. As a way to get around this problem, JEWEL allows saving the thermal information of these scatterings in the form of "ghost" particles, soft moment carriers in azimuth velocity space.

JEWEL's thermal subtraction method is used to remove background from collision events that contain jets. In experimental data, the background is subtracted from the reconstructed jets. However, as JEWEL does not simulate the soft event, it is not possible to follow the same prescription in the analysis of Monte Carlo events. Instead, the recoil scattering centers are removed from the event before hadronization, and no background subtraction is performed [57].

It is also possible to keep the thermal partons that interacted with a rigid parton ("recoils") in the event, but the thermal moment these partons had before the interaction must be subtracted from the final event. Transverse momentum and mass can be subtracted from nearby particles to ensure that defined mass squares are positive. The algorithm called the Constituent Subtraction method, is found below [57]:

1. The final state particles and thermal momenta are represented by the four-momenta $p_\perp$:

$$p_T = ((m_\delta + p_\perp)cosh(y), p_\perp cos(\phi), p_\perp sin(\phi), (m_\delta + p_\perp)sinh(y)) \qquad (2.52)$$

where the mass $m_\delta = \sqrt{m^2 + p_\perp^2} - p_\perp$, y rapidity and ϕ the azimuthal angle.

2. The distance between all possible pairs of particles in final state i and thermal momentum k is compiled:

$$\Delta R_{ik} = \sqrt{(y_i - y_k)^2 + (\phi_i - \phi_k)^2} \tag{2.53}$$

3. Starting from the smallest distance, the list is traversed, each pair being subtracted from the smallest $p_\perp$ and the smallest m_δ from their larger values:

$$\begin{aligned} &\text{if} \qquad p_\perp^{(i)} \geq p_\perp^{(k)} \Rightarrow \begin{cases} p_\perp^{(i)} \to p_\perp^{(i)} - p_\perp^{(k)} \\ p_\perp^{(k)} \to 0 \end{cases} \\ &\text{if} \qquad p_\perp^{(i)} < p_\perp^{(k)} \Rightarrow \begin{cases} p_\perp^{(i)} \to 0 \\ p_\perp^{(k)} \to p_\perp^{(k)} - p_\perp^{(i)} \end{cases} \end{aligned} \tag{2.54}$$

and

$$\begin{aligned} &\text{if} \qquad m_\delta^{(i)} \geq m_\delta^{(k)} \Rightarrow \begin{cases} m_\delta^{(i)} \to m_\delta^{(i)} - m_\delta^{(k)} \\ m_\delta^{(k)} \to 0 \end{cases} \\ &\text{if} \qquad m_\delta^{(i)} < m_\delta^{(k)} \Rightarrow \begin{cases} m_\delta^{(i)} \to 0 \\ m_\delta^{(k)} \to m_\delta^{(k)} - m_\delta^{(i)} \end{cases} \end{aligned} \tag{2.55}$$

4. The process continues until the list ends or until the 0.5 distance cut in ΔR_{ij} is performed to avoid subtracting large distances.

5. All zero $p_\perp$ moments are removed after all subtractions are performed. The remaining moment constitutes the subtracted ensemble.

Constituent subtraction is done on individual particles instead of four-moment subjets, making the jet mass much more stable and in agreement with experimental observations. Constituent subtraction can be performed on all final state particles either before or after jet reconstruction. The constituent subtraction was used to consider the recoils in all the simulations of this work, as we will see in the next chapter about the studied results.

Chapter 3

Results

3.1 Nuclear Modification Factor – R_{AA}

The nuclear modification factor (R_{AA}) is a fundamental parameter used to characterize the differences in particle production observed in the presence of a Quark-Gluon Plasma (QGP) and in collisions where this medium is absent. In particular, a QGP is expected to be formed in heavy ion collisions, while in proton-proton collisions, such a medium is not anticipated to occur.

This section aims to provide a comprehensive definition of R_{AA} and present the findings of simulations employing realistic hydrodynamics and JEWEL recoil subtraction techniques for various centralities and $R = 0.2, 0.3, 0.4, 0.6, 0.8$ and 1.0. Furthermore, the results obtained from these simulations will be compared with experimental data from high-energy experiments, such as those conducted by the ATLAS, ALICE, and CMS experiments at the Large Hadron Collider (LHC).

To this end, jets were reconstructed from the simulated data using the anti-k$_T$ algorithm, which were performed for PbPb and pp collisions at 2.76 and 5.02 TeV, respectively, using both Glauber+Bjorken and T$_\mathrm{R}$ENTo+v-USPhydro models. By performing these simulations, we aim to understand better the properties of QGP and its effects on particle production and explore the underlying physics of heavy ion collisions.

3.1.1 Definition

The R_{AA} is defined as the ratio of particle production per event in heavy-ion collisions (AA) to particle production in proton-proton collisions, normalized by the number of

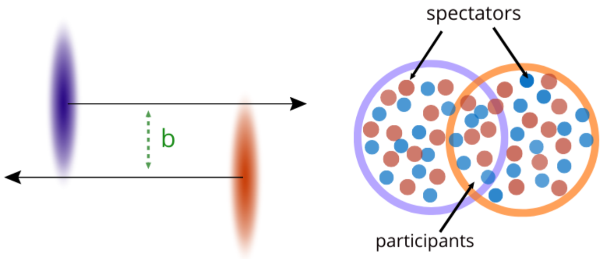

Figure 3.1: Illustration of atomic nuclei collision, showing impact parameter b (left) and participating nucleons and spectators (right).

nuclear collisions in the heavy ions (N_{coll}). The following formula gives it:

$$R_{AA}(p_T) \doteq \frac{1}{\langle N_{coll} \rangle} \frac{\frac{1}{N_{evt}} \frac{dN}{dp_T}|_{AA}}{\frac{1}{N_{evt}} \frac{dN}{dp_T}|_{pp}} \tag{3.1}$$

Where $dN/dp_T|_{AA}$ is the distribution of particles produced in heavy-ion collisions as a function of the transverse momentum p_T, and $dN/dp_T|_{pp}$ is the distribution of particles produced in pp collisions as a function of the transverse momentum p_T, and $\langle N_{coll} \rangle$ is the average number of binary collisions expected in the nucleus-nucleus interaction, calculated by Glauber model, Sec.2.1.1.

In the JEWEL simulation, each event only involves one hard scattering, which corresponds to the interaction between two partons in the colliding nuclei. As a result, $\langle N_{coll} \rangle = 1$. This simplification allows for a more efficient simulation of the partonic interactions in heavy-ion collisions.

When $R_{AA} > 1$, it indicates that the production of particles is enhanced in nucleus-nucleus collisions compared to pp. On the other hand, when the $R_{AA} < 1$, it indicates that the production of high-energy particles is suppressed in nucleus-nucleus collisions compared to proton-proton collisions. This suppression is mainly due to the energy loss of partons as they transverse the hot and dense medium. This suppression has a name: “jet quenching”. It is thought that a modification of the parton shower occurs due to interaction with the QGP and that intensification depends on the mechanism of energy loss, the properties of the medium, and the energy of the particles produced. The R_{AA} of jets can be used to test theoretical models of jet modification in the QGP.

3.1.2 Centrality Dependence

The impact parameter b illustrated in Fig. 3.1 is an important parameter of the collision since it affects its entire dynamics. More central collisions (small impact parameter) tends to produce a hotter and denser medium than peripheral ones (large impact parameter). Therefore, studying the dependence of observables on the impact parameter b is crucial for understanding the properties of the QGP and its formation in heavy-ion collisions. The simulations were performed with approximately 3 million events for each centrality: $0-10\%$, $10-20\%$, $30-40\%$, $40-50\%$, and $50-60\%$. The result of our simulation using Trento+vUSPhydro for the most central collisions for this observable can be seen in Figure 3.2 compared to the data from the detectors ALICE, ATLAS, and CMS.

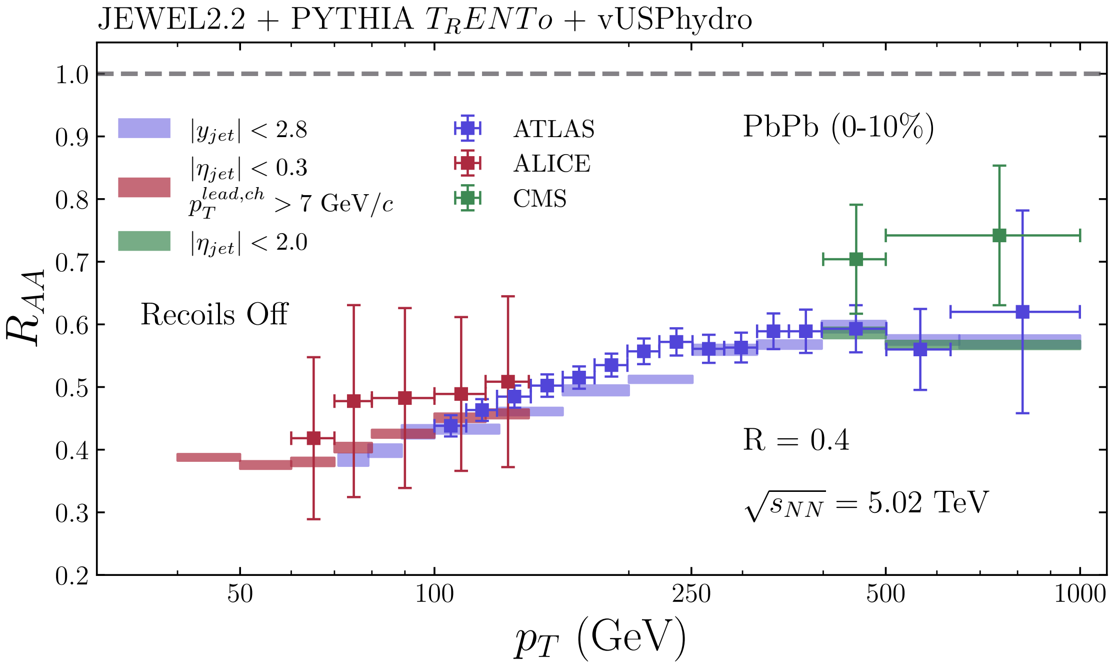

Figure 3.2: Jet nuclear modification factor for $\mathrm{T_RENTo}$+v-USPhydro compared to ALICE[58], ATLAS[59] and CMS[60] in central collisions. The anti-kT algorithm is used with R = 0.4 jets.

As shown, the data from ATLAS experiment [59] considers a larger region of p_T. As a result, the data from this LHC experiment were used as the base for the following reproducing results. The PbPb and pp collisions were simulated using JEWEL Glauber+Bjorken and JEWEL T_RENTo + v-USPhydro using the parameters in Appendix A. In which the value 0.4 was used for the R jet parameter radius and centrality of 0-10%, 10-20%, 30-40%, and 50-60% at $\sqrt{s_{NN}} = 5.02$. For the simulation of ATLAS data, $|y_{\text{jet}}| < 2.8$ was used. For CMS, $|\eta| < 2.0$ was used, and for ALICE simulation $|\eta| < 0.3$ was used, with values ranging from $0 - 10\%$ to $50 - 60\%$.

First, the outcome of the analysis was simulated using the implementation of the models T$_\mathrm{R}$ENTo and v-USPhydro to JEWEL, with and without recoils, in other words, using or not the subtraction method described in the 2.3.3 section, where the debey mass for recoils on was 1.1 and for recoils off was 1.0. The critical temperature was 170 MeV. See Figure 3.3.

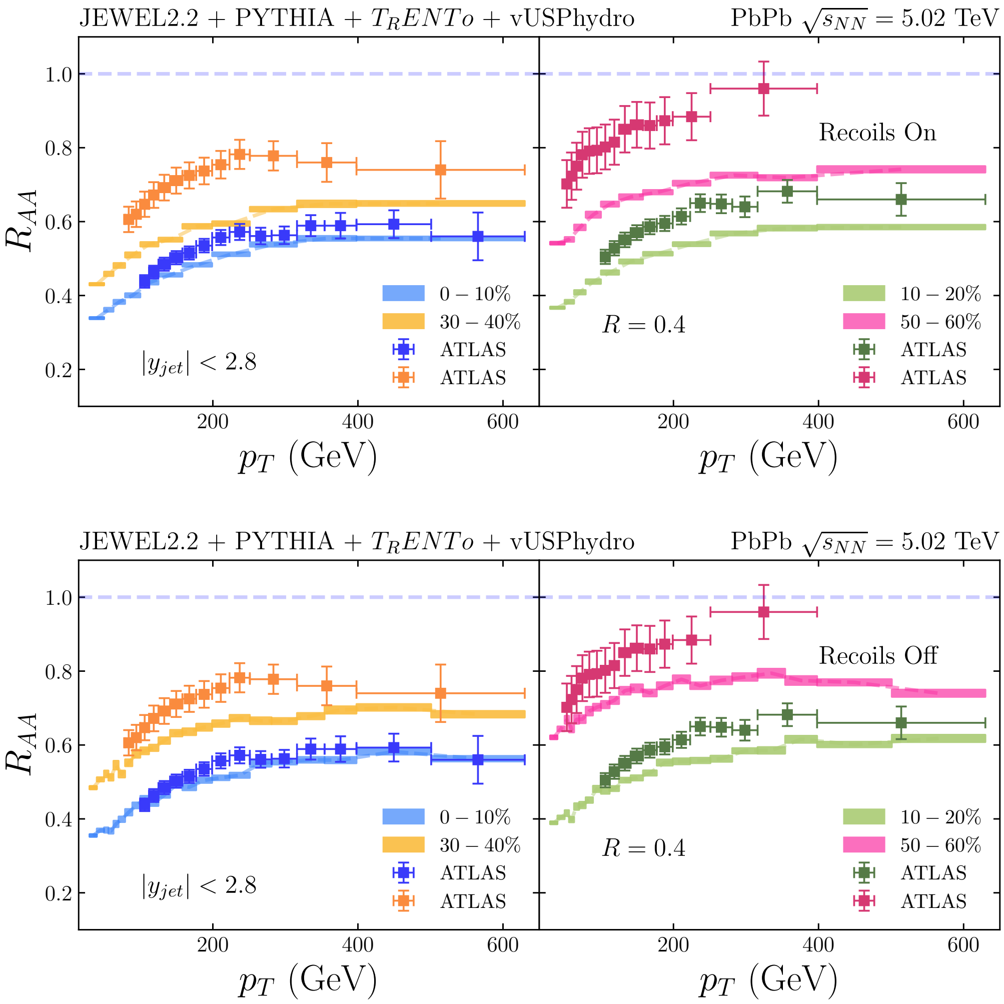

Figure 3.3: Color-coded jet nuclear modification factor for T$_\mathrm{R}$ENTo and v-USPhydro with ATLAS data [59] and recoils on (up) and off (down) for different centralities.

Figure 3.4, shows the results of the simulation using JEWEL's default configuration, Glauber for initial conditions, and Bjorken for the evolution of the hydrodynamic medium. The parameters remain the same, except for the MDS parameter of 0.9, as opposed to the

1.1 used by the model with v-USPhydro with recoils and 1.0 without recoils.

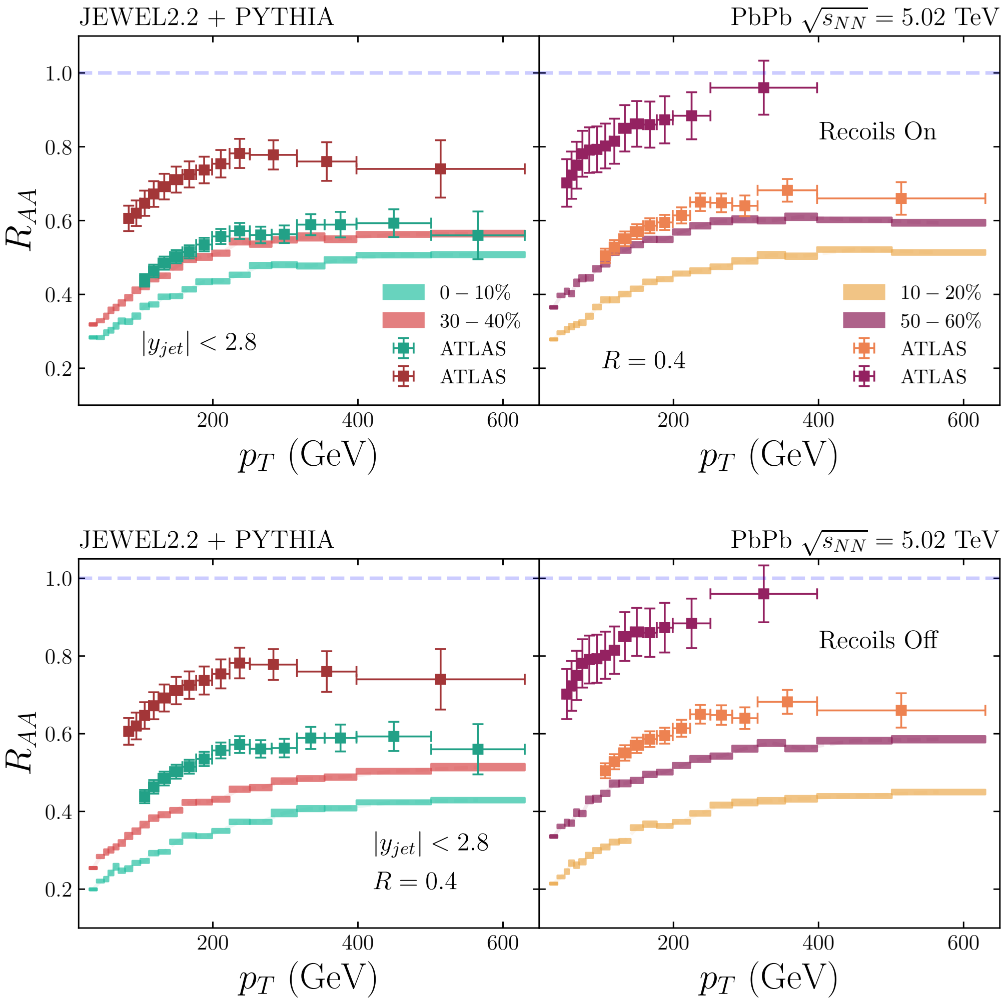

Figure 3.4: Color-coded jet nuclear modification factor for Glauber and Bjorken with ATLAS data [59] and recoils on (up) and off (down) for different centralities.

It is noticed that, for the energy of $\sqrt{s_{NN}} = 5.02$ TeV, with $R = 0.4$ and for all the configurations used in these results above, our implementation of a more realistic medium reproduces better the data from the ATLAS experiment. It is also possible to observe the significant deviation of JEWEL's default configuration concerning the data for more peripheral collisions $(50 - 60\%)$ compared to the more realistic one. Moreover, upon deactivating the subtraction method (recoils off), there is a slight approximation with the experimental data, as can be seen in Figure 3.3.

To analyze potential differences in how the medium can interfere with jets at lower energies in the simulation, the system was also studied with energy of $\sqrt{s_{NN}} = 2.76$ TeV and with $|y_{jet}| < 2.1$ for possible comparison with pre-existing data. For this purpose, data from the ATLAS experiment were used again for the same reason as before [61]. From the results of the figures below (3.5 and 3.6), we can draw the same conclusions as the previous paragraph for the energy of $\sqrt{s_{NN}} = 5.02$ TeV.

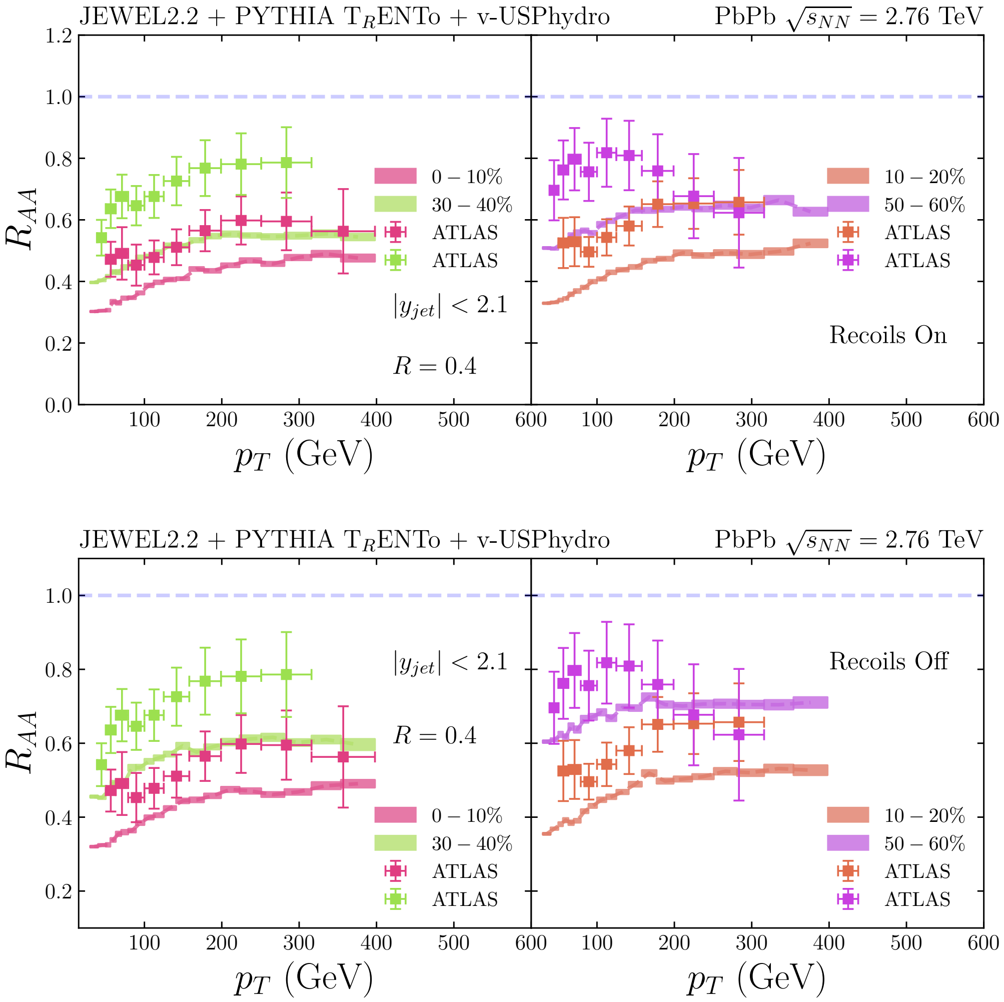

Figure 3.5: Color-coded jet nuclear modification factor for T$_{\rm R}$ENTo and v-USPhydro with ATLAS data [61] and recoils on (up) and off (donw) for different centralities.

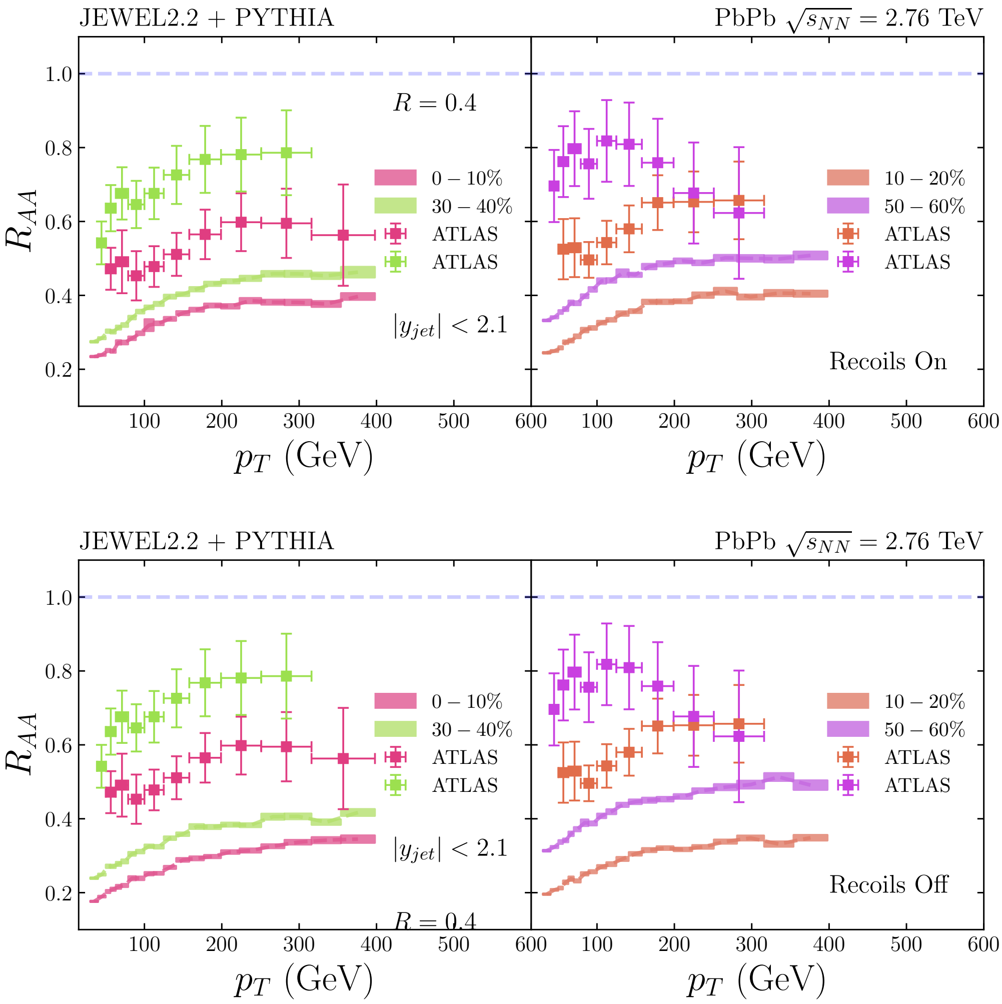

Figure 3.6: Color-coded jet nuclear modification factor for Glauber and Bjorken with ATLAS data [61] and recoils on (up) and off (down) for different centralities.

3.1.3 R factor variation

The R factor is a distance parameter used in the anti-k_T jet reconstruction algorithm (described in section 2.3.3) to determine the size of the jet cone surrounding each particle. Its value governs the collimation of the jet, influencing its resolution and susceptibility to background contamination.

By varying the R factor in observables such as R_{AA}, different regions of distances between the particles that make up the jet can be explored, allowing for more precise information about the interaction of jets with the QGP. Additionally, different R values can be used to optimize the sensitivity of jet measurements for different ranges of p_T of the particles composing the jet.

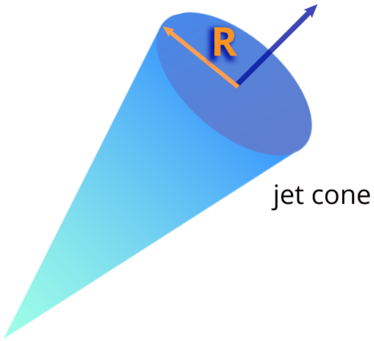

Figure 3.7: Illustration of particles in jet cone region.

Experiments at the LHC have employed varying R values, from R = 0.2 to R = 1.0, to optimize the performance of jet reconstruction for diverse event types and observables. Notably, when examining the R_{AA} of jets in heavy-ion collisions, it is critical to adjust the R parameter to investigate the dependence of the jet quenching effect on the jet size and its sensitivity to the medium properties. Comparing R_{AA} outcomes obtained with different R values enables testing theoretical predictions and distinguishing competing effects of jet fragmentation, energy loss, and flow.

From figures 3.8, 3.9, 3.10 and 3.11 similar to the indications in centrality dependence, v-USPhydro demonstrates an improvement over Bjorken, particularly concerning the recoil-off mode in results.

As R increases, Glauber+Bjorken exhibits different behaviors in the presence or absence of thermal subtraction. It is noticeable that with recoils enabled, the R_{AA} increases significantly, particularly for lower p_T, a trend that reverses when the subtraction method is not applied. Such an inversion behavior also occurs in the presence of the v-USPhydro hydrodynamic model in JEWEL, which might suggest that the employed background thermal subtraction (constituent subtraction), Sec.2.3.3, is subtracting beyond what is theoretically expected.

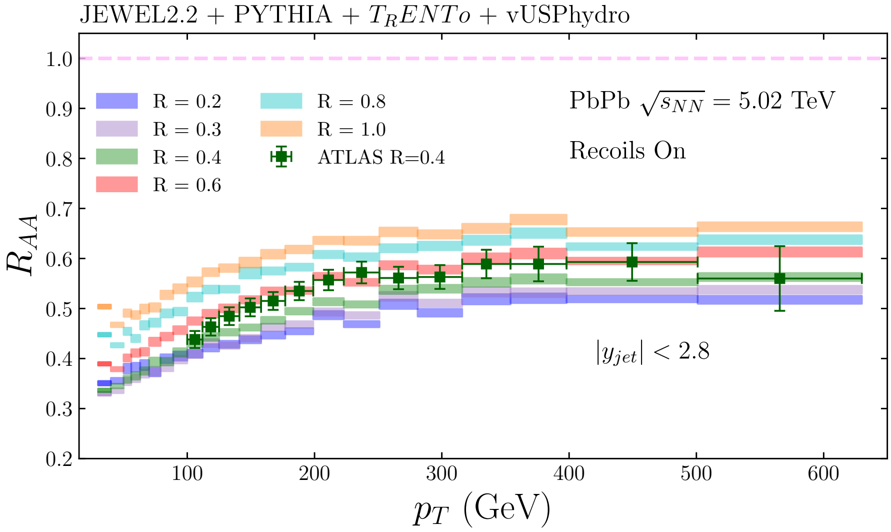

Figure 3.8: Jet nuclear modification factor for T_RENTo and v-USPhydro model with recoils compared to ATLAS [59] central $0 - 10\%$ results for multiple jet radio R.

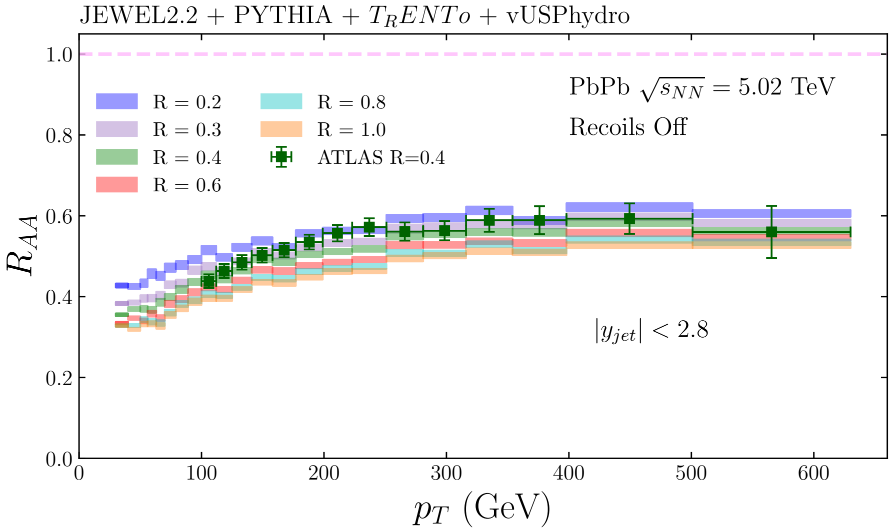

Figure 3.9: Jet nuclear modification factor for T_RENTo and v-USPhydro model without recoils compared to ATLAS [59] central $0 - 10\%$ results for multiple jet radio R.

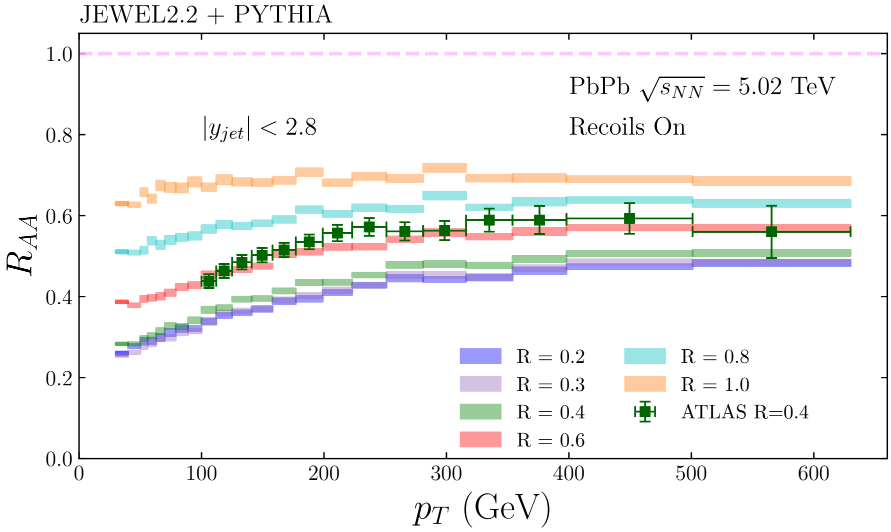

Figure 3.10: Jet nuclear modification factor for Glauber and Bjorken model with recoils compared to ATLAS [59] central $0 - 10\%$ results for multiple jet radio R.

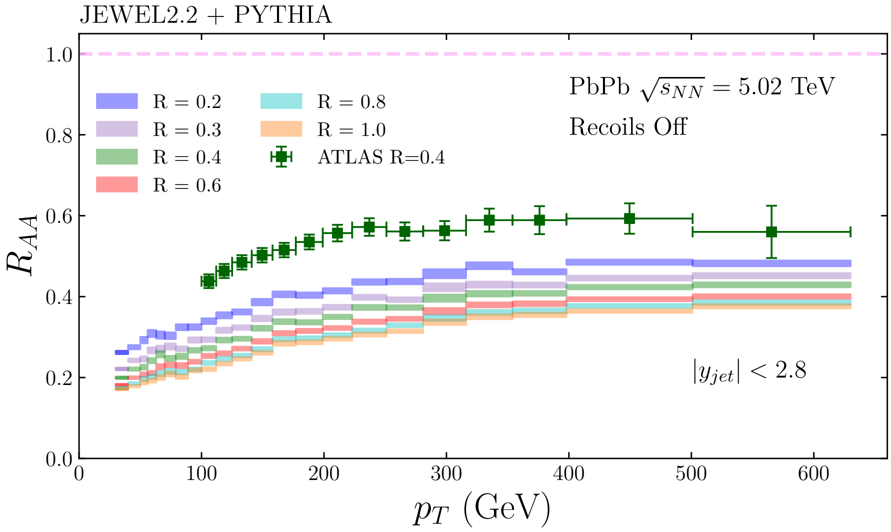

Figure 3.11: Jet nuclear modification factor for Glauber and Bjorken model without recoils compared to ATLAS [59] central $0 - 10\%$ results for multiple jet radio R.

Conducting the study at two distinct energies is paramount for comprehending how nuclear suppression effects may vary with collision energy. Different energies can offer insights into the medium's interference at different energy regimes. Therefore, simulations and analyses were replicated for the energy of 2.76 TeV. Figures 3.12, 3.13, 3.14, and 3.15 depict the outcomes for R ranging from 0.2 to 1.0 for both the default JEWEL configuration (Glauber+Bjorken) and JEWEL + T$_R$ENTo + v-USPhydro.

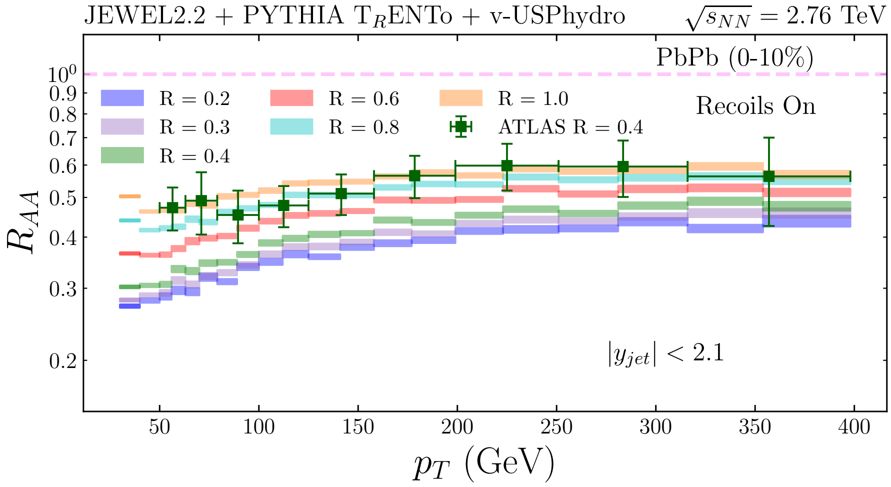

Figure 3.12: Jet nuclear modification factor for T$_\mathrm{R}$ENTo and v-USPhydro model with recoils compared to ATLAS [59] central $0-10\%$ results for multiple jet radio R.

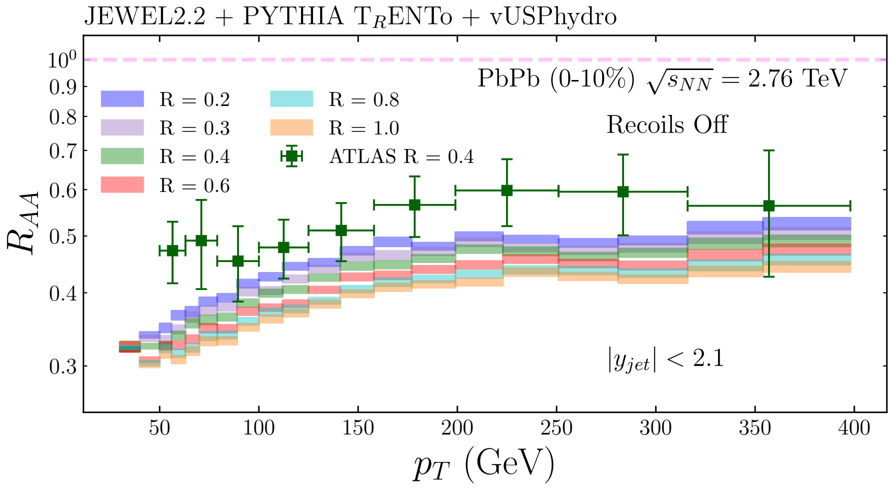

Figure 3.13: Jet nuclear modification factor for T$_\mathrm{R}$ENTo and v-USPhydro model without recoils compared to ATLAS [59] central $0-10\%$ results for multiple jet radio R.

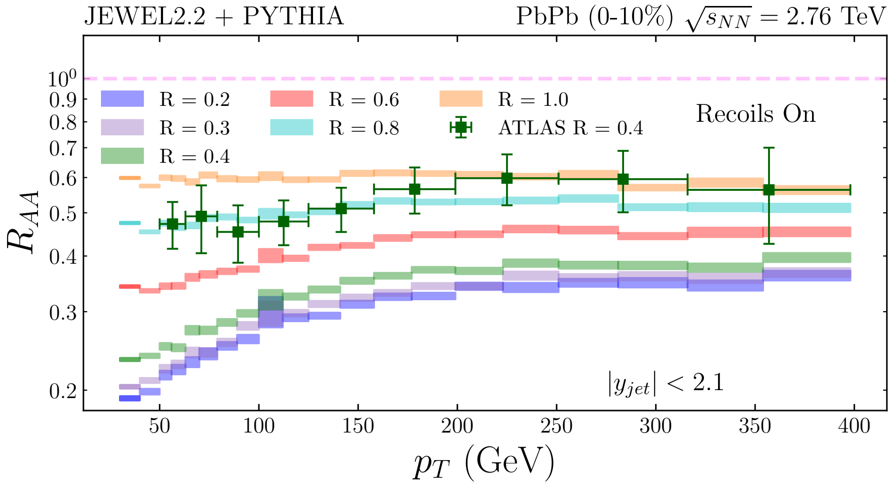

Figure 3.14: Jet nuclear modification factor for Glauber and Bjorken model with recoils compared to ATLAS [59] central $0-10\%$ results for multiple jet radio R.

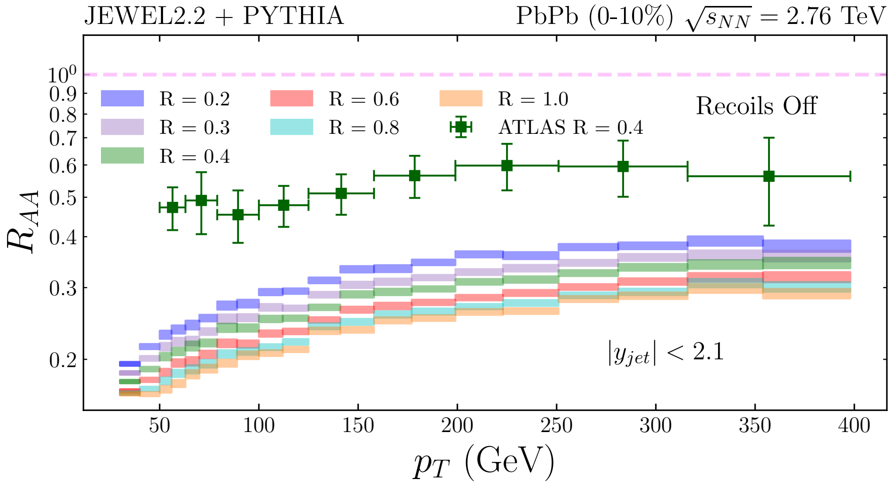

Figure 3.15: Jet nuclear modification factor for Glauber and Bjorken model without recoils compared to ATLAS [59] central $0-10\%$ results for multiple jet radio R.

Similar to the findings at 5.02 TeV, it is evident that the recoils-off mode aligns better with the data, particularly for the JEWEL configuration with a more realistic medium. However, there is a more pronounced suppression of the R_{AA} for recoils-on. Additionally, at low p_T, similar to the result in Figure 3.10, the nuclear modification factor notably increases with the increment of R, suggesting a potential parton overproduction with the thermal subtraction method. This effect is also observed in the realistic medium configuration, as shown in Figure 3.12.

3.2 Dijet – x_J

3.2.1 Definition

When two particles collide in a process called $2 \rightarrow 2$ scattering, they often produce a pair of jets. These back-to-back jets, known as “dijets”, are formed through a process called QCD evolution of the initial partons. Compared to single jets, dijets provide a cleaner way to study jet quenching in Pb+Pb collisions, as they experience asymmetric energy loss due to traveling different path lengths through the QGP. This is caused by the overlapping nuclei’s geometry and the jet trajectories’ orientation. Previous research has shown that the geometry of the nuclei affects the rates of jets detected in these collisions.

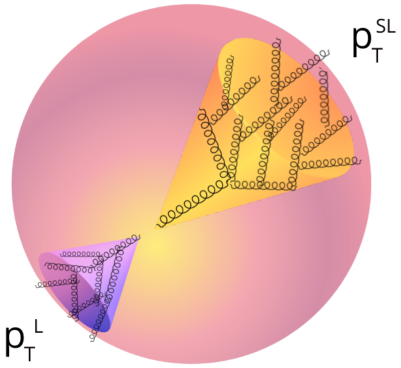

Figure 3.16: Illustration of the momentum balance of the leading and sub-leading jet system.

Additionally, fluctuations in the energy loss process may cause each jet to experience different amounts of energy loss. By measuring the p_T balance of dijets, researchers can better understand the relative contribution of fluctuations and geometry to jet quenching.

To evaluate and contrast the ultimate transverse momenta of the two jets defining a dijet, the momentum balance of the leading dijet is studied through the ratio:

$$x_J \equiv p_{T,2}/p_{T,1} \tag{3.2}$$

Where the two jets with the highest energy from the event’s set of jets are used to construct the primary dijet, where $p_{T,1}$ represents the transverse momentum of the leading

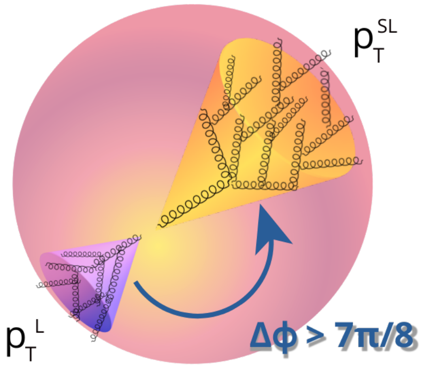

Figure 3.17: Illustration of the angle $\Delta\phi > 7\pi/8$ between the transverse momentum of the leading and sub-leading jet system.

jet with the highest-p_T, and $p_{T,2}$ represents the transverse momentum of the subleading jet with the second-highest-p_T.

3.2.2 Energy dependence

This study presents simulations of di-jet yield, which is the number of jet pairs in a given interval of $p_{T,1}$ normalized by the total number of jet pairs, represented as $(1/N)dN/dx_J$. The results are shown as a function of x_J, in intervals of $p_{T,1}$ for collision with centrality $0-10\%$. The binning in $(p_{T,1}, p_{T,2})$ distribution is chosen so that the bins correspond to fixed ranges of x_J, and the $(1/N)dN/dx_J$ results are obtained by projecting into these x_J bins. The simulations were performed with the aim of replicating existing experimental data. We employed the parameter $R = 0.4$ for this purpose, and furthermore, we examined potential variations in the outcomes at different energy levels, specifically $\sqrt{s_{NN}} = 2.76$ TeV and $\sqrt{s_{NN}} = 5.02$ TeV.

Specific cuts and parameters were duplicated to enable a reliable comparison between experimental data from the Large Hadron Collider (LHC) and simulations. To compare with ATLAS data, a cut of $|\eta_{jet}| < 2.1 - R$ was implemented, along with a jet transverse momentum cut ranging from 20 to 1000 GeV and $\sqrt{s_{NN}} = 2.76$ TeV. This ensured consistency in the comparison between the simulated and experimental data. The jet pairs formed are from the two highest-p_T jets in the event with $p_T > 20$ GeV. The pair was required to have $\Delta\phi > 7\pi/8$, where $\Delta\phi$ it is defined by the angle between the transverse momentum leading and sub-leading jets $p_{T,1}$ and $p_{T,2}$.

The initial simulations were conducted using the energy of $\sqrt{s_{NN}} = 5.02$ TeV with a radius parameter $R = 0.4$ and centrality of $0 - 10\%$, in order to facilitate comparison with the experimental data from the ATLAS experiment [62]. The applied cut for the transverse momentum of the leading jet was $158 < p_{T,1} < 178$ GeV, as shown in Figures 3.18 below.

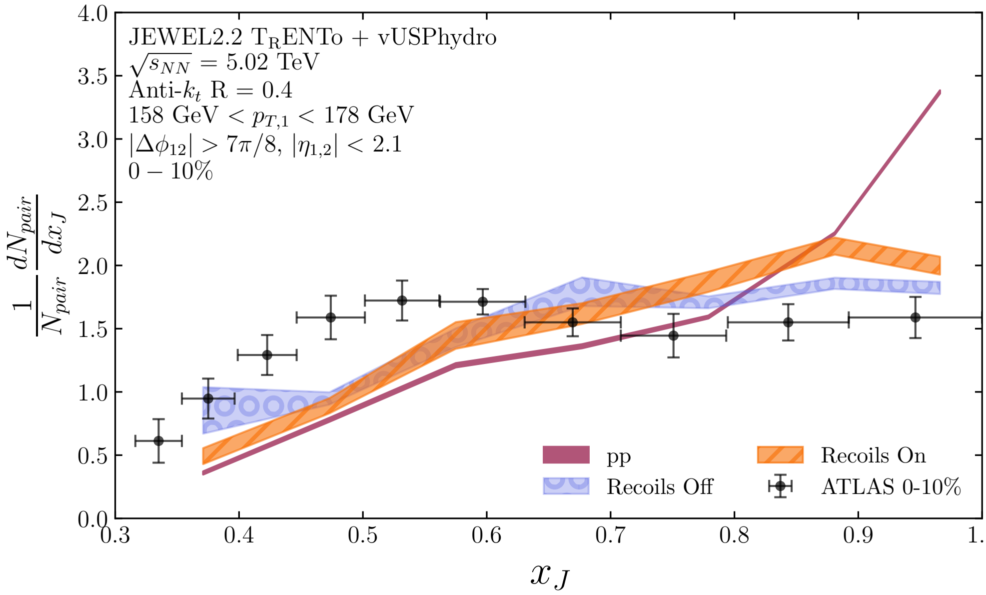

Figure 3.18: The $(1/N)dN/dx_J$ distributions for jet pairs with $158 < p_{T,1} < 178$ GeV for T$_R$ENTo + v-USPhydro for $R = 0.4$ jets at $\sqrt{s_{NN}} = 5.02$ TeV. The PbPb data [62] are shown in black, while the pp distribution is shown for comparison in purple and is the same in all plots.

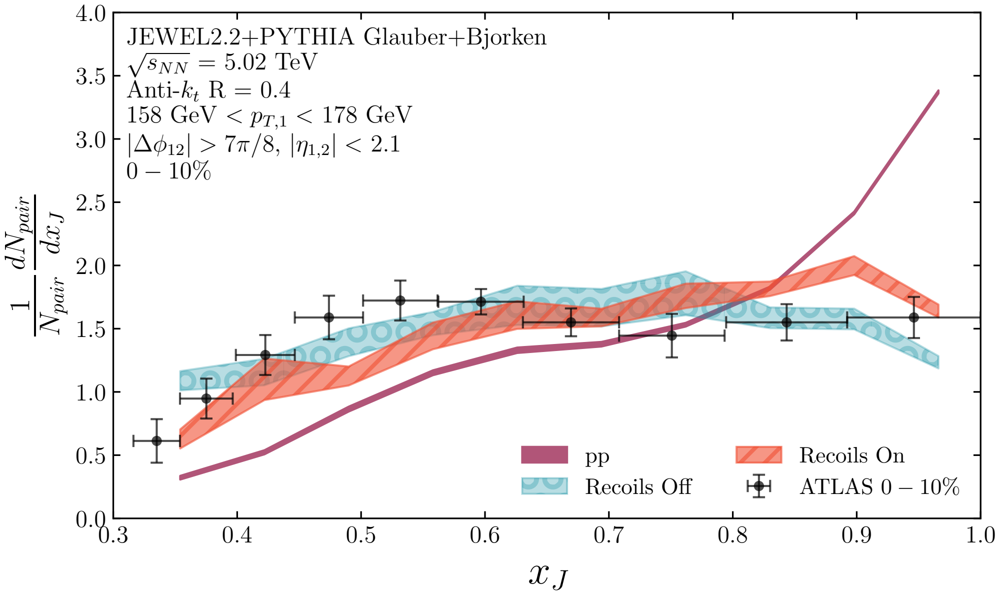

Figure 3.19: The $(1/N)dN/dx_J$ distributions for jet pairs with $158 < p_{T,1} < 178$ GeV for Glauber + Bjorken for $R = 0.4$ jets at $\sqrt{s_{NN}} = 5.02$ TeV. The PbPb data [62] are shown in black, while the pp distribution is shown for comparison in purple and is the same in all plots.

From the results in Figures 3.18 and 3.19, it is noticeable that there is a slight improvement in the data description when not employing the method of thermal background subtraction, that is, with recoils turned off. Additionally, for this energy and centrality, that slight increase in the distribution around $0.45 < x_J < 0.65$ is better captured by the default JEWEL simulation without recoils.

In an attempt to ascertain whether this trend persists for other energies, centralities, and transverse momentum cuts, PbPb collisions were once again simulated, this time at an energy of $\sqrt{s_{NN}} = 2.76$ TeV while keeping the jet radius $R = 0.4$. However, the centrality was adjusted to $40 - 60\%$, and the transverse momentum cuts were set at $100 < p_{T,1} < 126$ GeV. The outcomes are presented below in Figures 3.20 and 3.21.

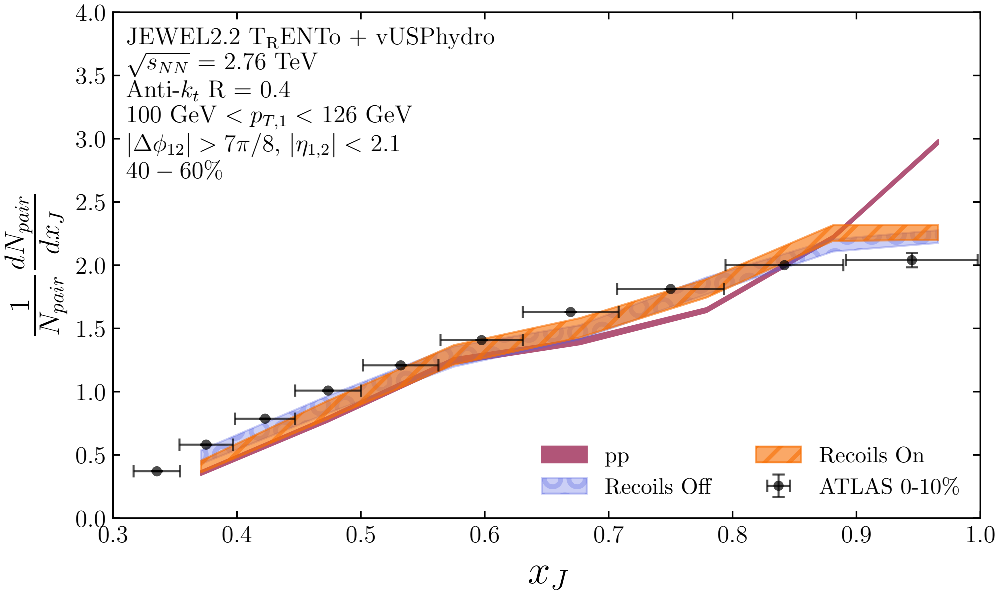

Figure 3.20: The $(1/N)dN/dx_J$ distributions for jet pairs with $100 < p_{T,1} < 126$ GeV for T$_R$ENTo + v-USPhydro for $R = 0.4$ jets at $\sqrt{s_{NN}} = 2.76$ TeV. The PbPb data [63] are shown in black, while the pp distribution is shown for comparison in purple and is the same in all plots.

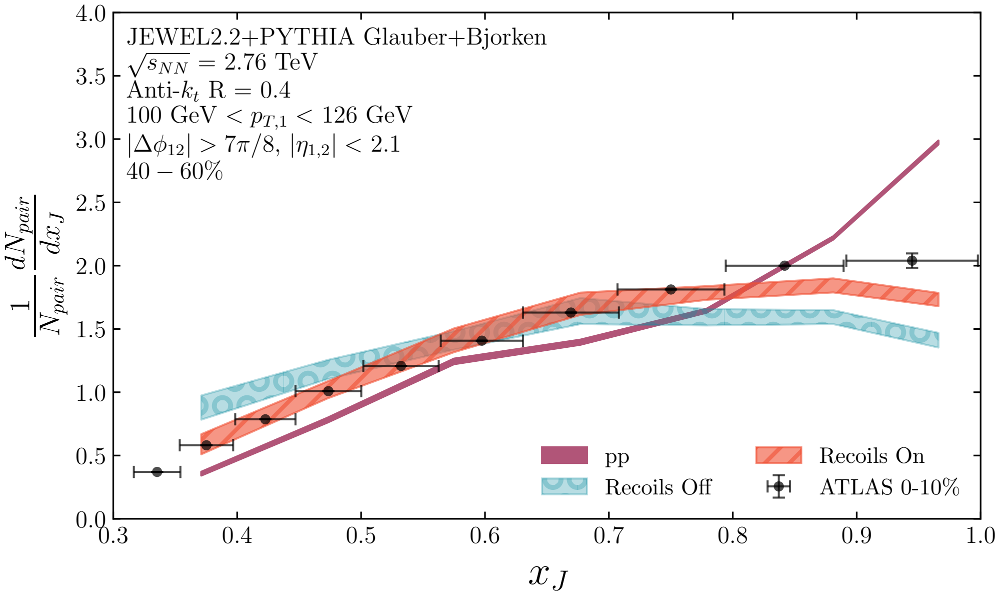

Figure 3.21: The $(1/N)dN/dx_J$ distributions for jet pairs with $100 < p_{T,1} < 126$ GeV for Glauber + Bjorken for $R = 0.4$ jets at $\sqrt{s_{NN}} = 2.76$ TeV. The PbPb data [63] are shown in black, while the pp distribution is shown for comparison in purple and is the same in all plots.

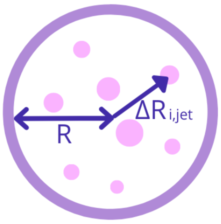

Figure 3.22: Euclidean azimuth-rapidity distance of particle i from the jet axis representation.

For the configuration used in these latest results depicted in Figures 3.20 and 3.21, a notably distinct behavior is observed compared to the outcome presented in Figures 3.18 and 3.19 for the energy of 5.02 TeV. For the energy of 2.76 TeV and a more peripheral centrality range, the combination of JEWEL, T$_R$ENTo, and vUSPhydro models significantly provides a better description of the data, particularly when increasing the value of x_J, i.e., when the two leading jets possess similar momenta.

Despite this slight improvement in data description utilizing the more realistic medium model, it might be deduced that x_J is not necessarily a suitable observable for studying and comprehending the medium interference in the formation of particles in high-energy heavy-ion collisions. This is because, for central collisions and an energy of $\sqrt{s_{NN}} = 5.02$ TeV, the data agrees with $x_J \sim 1$, without notable differences among the employed models. On the other hand, for more peripheral collisions at an energy of $\sqrt{s_{NN}} = 2.76$ TeV, both models describe the data well, albeit the combined model with vUSPhydro exhibits an improved description, particularly around $x_J \sim 1$.

3.3 Angularity – λ_α^κ

3.3.1 Definition

The study of the internal structure of jets has become an active area in particle physics in the last few years. Jet substructure techniques are generally used in experimental analyses of the LHC in search of a better understanding of the Standard Model. From the point of view of theoretical physics, the jet substructure has been contributing to renewed calculations of QCD. New ideas constantly appear, proposing better observables for a solid description of the jet substructure [64].

Generalized Angularities are computed on the hardest jet, denoted as the jet with the highest transverse momentum ($p_{T,\text{jet}}$). In this context, the angularities are measured using the formula in [64], see Figure 3.22. Where $\Delta R_{i,jet}$ represents the Euclidean azimuth-rapidity distance of particle i from the axis of the jet.

$$\lambda_\alpha^\kappa \equiv \sum_{i \in jet} \left(\frac{p_{T,i}}{p_{T,jet}}\right)^\kappa \left(\frac{\Delta R_{i,jet}}{R}\right)^\alpha \tag{3.3}$$

$$\Delta R_{i,jet} = \sqrt{(y_i - y_{jet})^2 + (\varphi_i - \varphi_{jet})^2} \tag{3.4}$$

We can define the angular fraction with respect to the jet radius R as $\theta_i \equiv \Delta R_{i,jet}/R$ and $z_i \equiv p_{T,i}/p_{T,jet}$ as the energy fraction. Then, generalized angularity becomes [64].

$$\lambda_\alpha^\kappa \equiv \sum_{i \in jet} z_i^\kappa \theta_i^\alpha \tag{3.5}$$

Starting from the case where $\kappa = 1$ and also when $\alpha = 0$, as in [64].

$$\begin{aligned} e_\alpha \equiv \lambda_\alpha^1 &= \sum_{i \in jet} z_i \theta_i^\alpha \\ \lambda_0^\kappa &= \sum_{i \in jet} z_i^\kappa \end{aligned} \tag{3.6}$$

It is easy to verify that case where $\kappa = 1$ and $\alpha = 0$ result in $\lambda_0^1 = 1$. Therefore, we can expand the λ_0^κ around $\kappa = 1$ as

$$\lim_{\kappa \to 1} \lambda_0^\kappa = 1 + \sum_{i \in jet} (\kappa - 1) z_i \ln z_i \tag{3.7}$$

In the collision context at LHC, the analytic investigations commence with considering the IRC (Infrared and Collinear) safe limit, characterized by $\kappa = 1$ [64]. We focus on this limit's angularities denoted as $e_\beta = \lambda_\alpha^1$. These angularities are IRC safe for all values of α greater than zero. Notably, when α equals 1, it is commonly referred to as the width (or broadening or girth), whereas $\alpha = 2$ is associated with the observable known as thrust, which exhibits a relationship with the squared mass at a fixed jet energy [64], see Figure 3.23.

In this way, the generalized angularity can be rewritten as

$$\lambda_\alpha \equiv \sum_{i \in jet} z_i \theta_i^\alpha \tag{3.8}$$

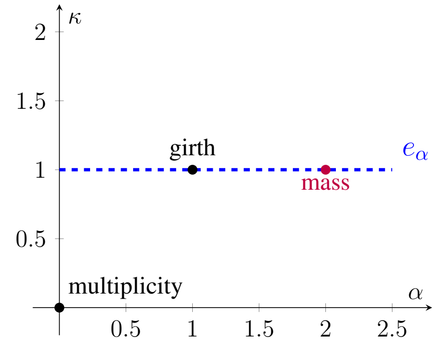

Figure 3.23: The visualization of the observable space λ_β^κ includes well-known jet observables used in quark/gluon discrimination. For example, the line $\kappa = 1$ represents IRC safe angularities, denoted as e_α. The origin $(\beta, \kappa) = (0, 0)$ corresponds to multiplicity. The point $(1, 1)$ is associated with "girth," which also refers to broadening and width. Similarly, point $(2, 1)$ represents "mass," which is related to the jet-mass-squared divided by energy (thrust).

3.3.2 Jet Mass

We begin with an important jet physics observable, the jet invariant mass, which appears when $\kappa = 1$ and $\alpha = 2$ in Eq.(3.5). The jet mass is a direct measure of the energy distribution of particles composing a jet. Since jets consist of several particles, measuring their mass allows for probing the distribution of these particles within the jet.

$$\lambda_2^1 = \left(\frac{m}{p_T}\right)^2 + \mathcal{O}(\lambda_2^2) \tag{3.9}$$

which results in the magnitude of the four-momentum sum of constituents inside a jet [65][66]

$$M_{jet} = \sqrt{E - p_T^2 - p_z^2} \tag{3.10}$$

where E is the jet energy, p_T is the transverse momentum, and p_z is the longitudinal momentum of the jet.

Certain cuts and parameters were replicated to consistently compare simulations and experimental data from the Large Hadron Collider (LHC). For the comparison with ALICE data, a cut of $|\eta_{jet}| < 0.9 - R$ was applied in addition to a jet transverse momentum cut between 60 and 80 GeV, 80 and 100 and 100 and 120 GeV [65].

The parameter $R = 0.4$ and energy $\sqrt{s_{NN}} = 2.76$ TeV was compared with the ALICE data for the first result. The result can be found in Figure 3.24.

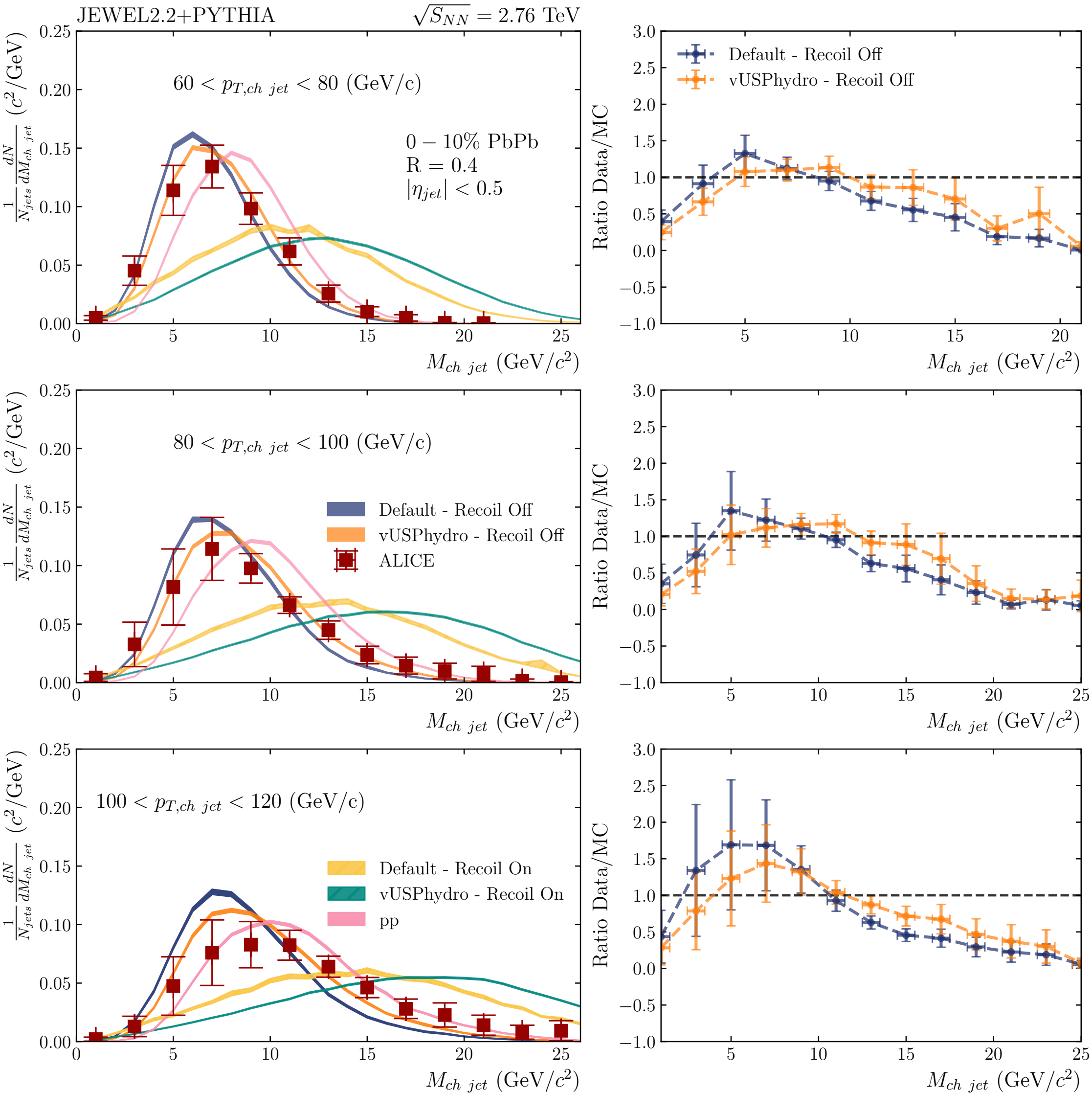

Figure 3.24: Jet mass distribution for JEWEL+Glauber+Bjorken and JEWEL+T$_\mathrm{R}$ENTRo+v-USPhydro with and without recoils jets and R = 0.4 compared to ALICE data [65] from central Pb–Pb collisions for three ranges of $p_{T,ch\ jet}$.

It can be observed that across all jet transverse momentum cuts, among all four employed models, those that exhibit the closest agreement are the ones without recoils, namely JEWEL Default and JEWEL+T$_R$ENTo + v-USPhydro. Furthermore, the model featuring a realistic medium significantly approaches the data compared to JEWEL Default. This suggests a high likelihood that the subtraction method employed by JEWEL is removing some of the final jet energy it shouldn't, as evidenced by the yellow and green curves in Figure 3.24.

3.4 Hadron-jet correlation

One technique employed for studying jets in heavy-ion collisions is the semi-inclusive measurement of jets recoiling against a high-energy charged hadron trigger. This method involves identifying a high-energy charged hadron, acting as a trigger for jet production, and quantifying the jet production rate as a function of various variables, such as jet transverse energy and the energy loss experienced by the jet as it traverses the hot and dense medium created during the collision. In essence, the semi-inclusive measurement of jets recoiling against a high-energy charged hadron trigger serves as a potent tool for investigating jet-medium interactions in central Pb-Pb collisions, shedding light on the properties of the medium.

The primary objective of this study is to analyze jet quenching in lead-lead ion collisions at a center-of-mass energy of 2.76 TeV per nucleon-nucleon pair, employing the semi-inclusive jet measurement technique [67].

Jets are reconstructed using charged particle tracks with the anti-k$_T$ algorithm, imposing an infrared cutoff for tracks with $p_T > 5.0$ GeV/c in analysis. Background unrelated to the jet signal is corrected only at the level of average distributions, without event-by-event discrimination between the jet signal and background. This correction method leverages the phenomenology of jet production in QCD.

In this study, we consider jet candidates valid if their pseudo-rapidity (η_{jet}) falls within the range $|\eta_{jet}| < 0.5$ for jet sizes $R = 0.4$. Pseudo-rapidity is a measure of the angle at which particles are produced in the detector. Additionally, we define the azimuthal acceptance for the recoil yield measurement as $\pi - \Delta\phi < 0.6$, see Figure 3.25. Here, $\Delta\phi$ represents the angular difference between the azimuthal angle of the trigger hadron ϕ_{trig} (Trigger Track, or TT, class) and the central position of the jet candidate (ϕ_{jet}), with the constraint that $0 \leqslant \phi_{trig} \leqslant \pi$ [67].

The semi-inclusive h+jet distribution represents the p_T-differential distribution of re-

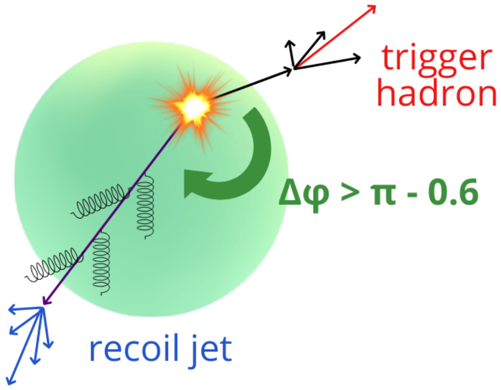

Figure 3.25: Semi-inclusive hadron-jet correlation scheme.

coil jets, scaled by the number of trigger hadrons (N_{trig}). This distribution, denoting the count of jets observed within the recoil acceptance region relative to the count of trigger hadrons, is analogous to the ratio of inclusive production cross-sections.

$$\frac{1}{N_{trig}}\frac{d^2N^{AA}_{jet}}{d\eta_{jet}\;dp^{ch}_{T,jet}}\bigg|_{p_{T,trig}\in\ \mathrm{TT}} = \left(\frac{1}{\sigma^{AA\to h+x}}\frac{d^2\sigma^{AA\to h+jet+x}}{dp^{ch}_{T,jet}\;d\eta_{jet}}\right)\bigg|_{p_{T,h}\in\ \mathrm{TT}} \tag{3.11}$$

Where AA represents either pp or $Pb-Pb$ collisions, $\sigma^{AA\to h+X}$ represents the cross-section for generating a hadron within the chosen p_T range of the selected TT class. Similarly, $d2\sigma^{AA\to h+jet+X}/p^{ch}_{T,jet}d\eta$ stands for the differential cross-section for the coincidental production of a hadron within the TT range and a recoil jet, with $p^{ch}_{T,jet}$ and η_{jet} denoting the transverse momentum and pseudo-rapidity of the charged jet [67].

As in the experimental description [67], for the analysis, trigger hadrons are confined to the charged-track acceptance region $|\eta| < 0.9$ and are chosen within specific $p_{T,trig}$ intervals. These intervals are defined as follows: $8 < p_{T,trig} < 9$ GeV/c, denoted as TT{8,9}, and referred to as the Reference TT class; and $20 < p_{T,trig} < 50$ GeV/c, denoted as TT{20,50}, and referred to as the Signal TT class both at $\sqrt{s_{NN}} = 2.76$ TeV.

The results for JEWEL + T$_R$ENTo + v-USPhydro with and without thermal subtraction (recoils On and Off) can be found in Figures 3.26 and for JEWEL Glauber + Bjorken with and without thermal subtraction (recoils On and Off) can be found in Figures 3.27.

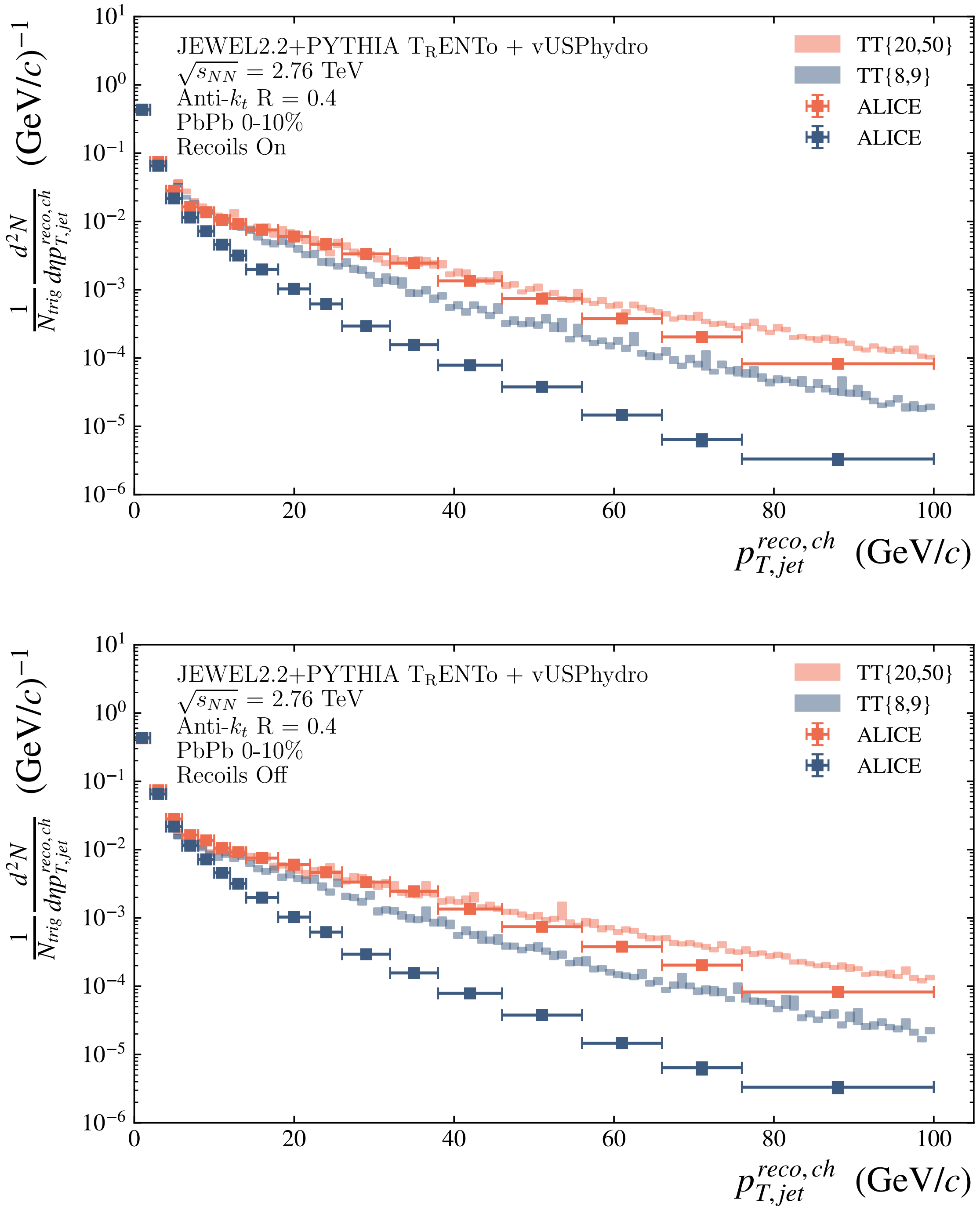

Figure 3.26: Semi-inclusive h+jet distribution corresponds to the p_T-differential distribution of recoil jets normalized by the number of trigger hadrons simulated using JEWEL with T_RENTo + v-USPhydro configuration. Data from [67].

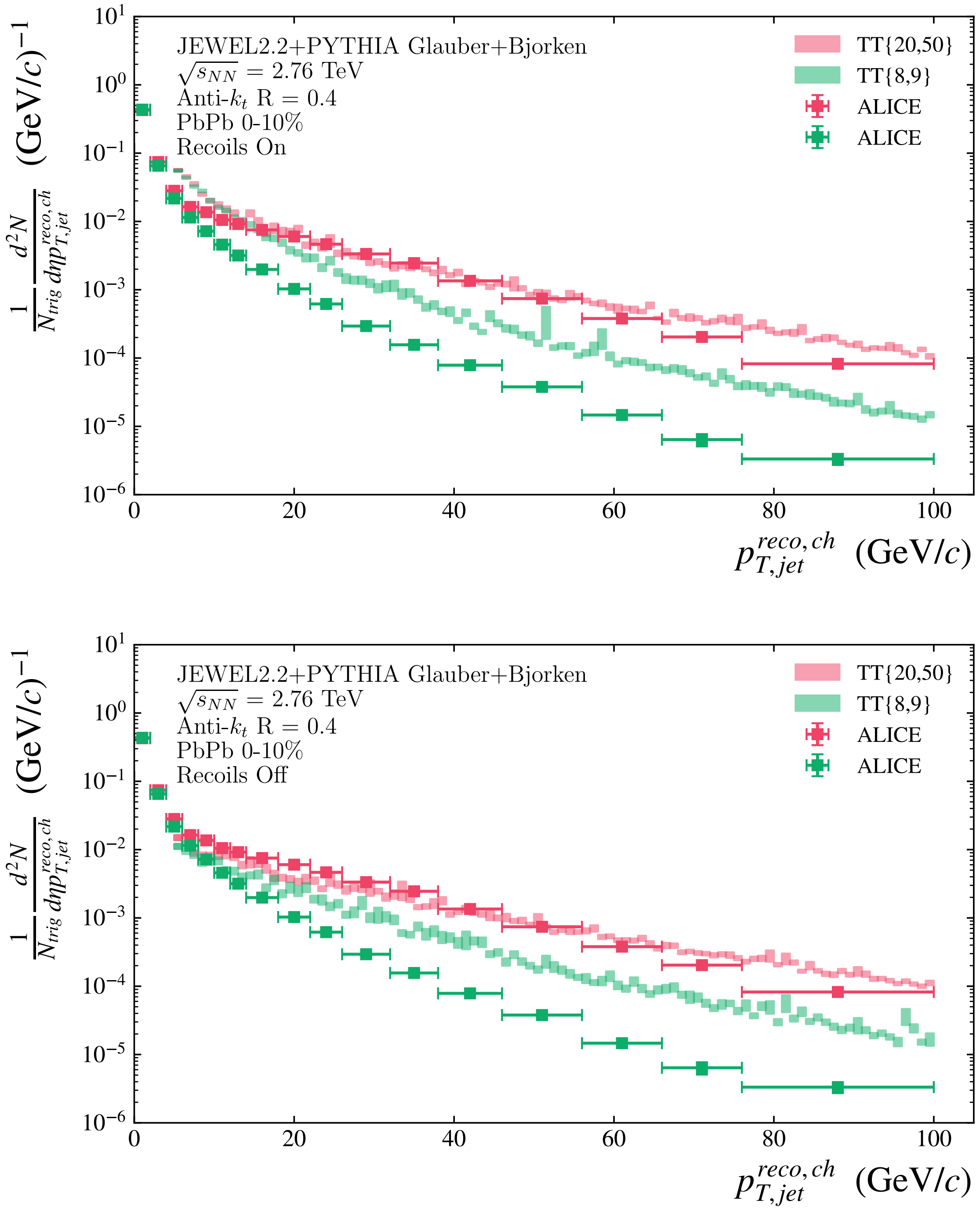

Figure 3.27: Semi-inclusive h+jet distribution corresponds to the p_T-differential distribution of recoil jets normalized by the number of trigger hadrons simulated using JEWEL default configuration. Data from [67]

From the results, we observe that there are no discernible differences between with and without recoils for the realistic medium (T$_R$ENTo + v-USPhydro). Furthermore, we find that the cut TT{20,50} adequately reproduces the experimental data, while for TT{8,9}, the description is not suitable and deviates as $p_{T,jet}^{reco,ch}$ increases, as seen in Figure 3.26.

To gain further insights, the next step in this study was to analyze the hadron-jet correlation using another observable called Δ_{recoil}. This entails the difference between two semi-inclusive hadron-jet distributions following Equation (3.11) for the Signal and Reference TT classes, as described in [67].

$$\Delta_{recoil} = \frac{1}{N_{trig}} \frac{d^2 N_{jet}^{AA}}{d\eta_{jet}\, dp_{T,jet}^{ch}}\Bigg|_{p_{T,trig} \in\, TT_{Sig}} - c_{Ref} \frac{1}{N_{trig}} \frac{d^2 N_{jet}^{AA}}{d\eta_{jet}\, dp_{T,jet}^{ch}}\Bigg|_{p_{T,trig} \in\, TT_{Ref}} \tag{3.12}$$

The value for constant c_{Ref} utilized in [67] was determined through a linear fit near $p_{T,jet}^{reco,ch} = 0$ within a linear region present in the Ratio(TT{20,50}/TT{8,9}) plot. Since our simulated results have a minimum $p_{T,jet}^{reco,ch}$ of 5.0 GeV/c, which falls outside the region suitable for a similar fit, the same value of c_{Ref} as in [67] was applied in this work, that is $c_{Ref} = (0.96 \pm 0.01)$. See Figures 3.28, 3.29, 3.30 and 3.31.

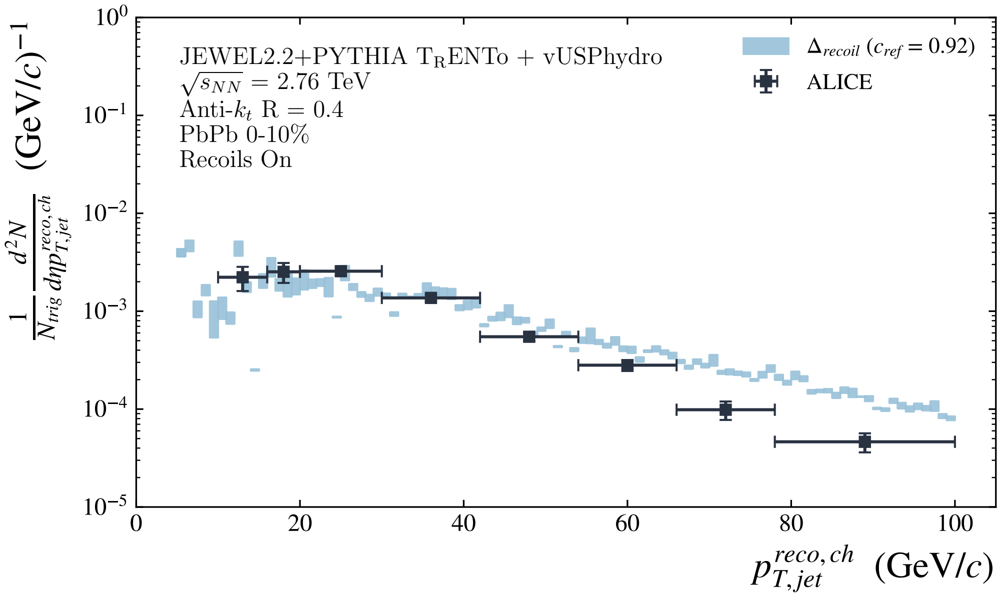

Figure 3.28: Distribution of Δ_{recoil} using JEWEL T$_R$ENTo + v-USPhydro with recoils for R = 0.4 in central Pb-Pb collisions for Signal TT class {20,50} and Reference TT class {8,9}. Data from [67].

The results obtained in this analysis indicate that the semi-inclusive correlation between hadrons and jets is not a sensitive observable to the medium properties. This is evi-

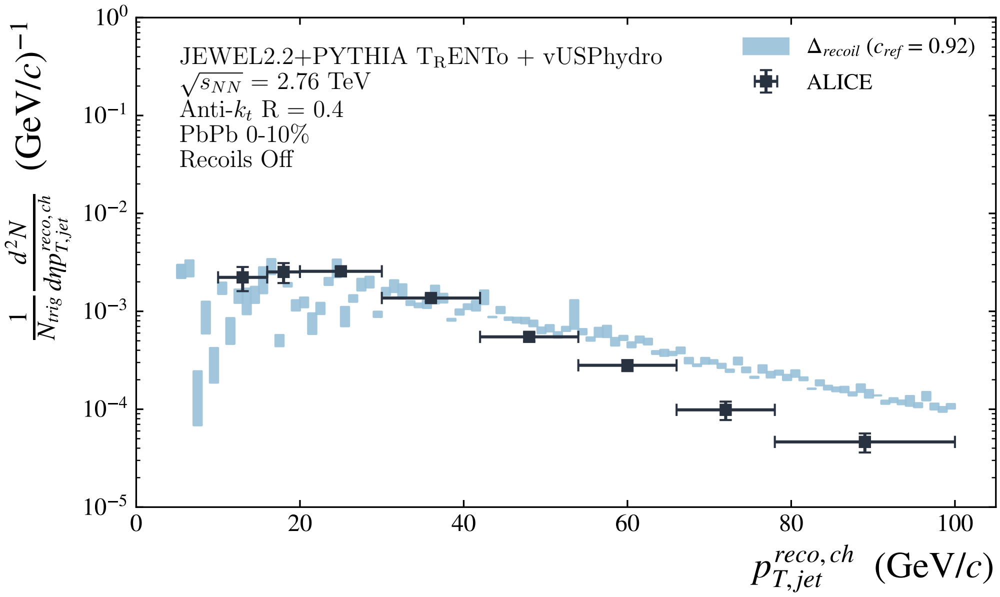

Figure 3.29: Distribution of Δ_{recoil} using JEWEL T$_R$ENTo + v-USPhydro without recoils for R = 0.4 in central Pb-Pb collisions for Signal TT class $\{20,50\}$ and Reference TT class $\{8,9\}$. Data from [67].

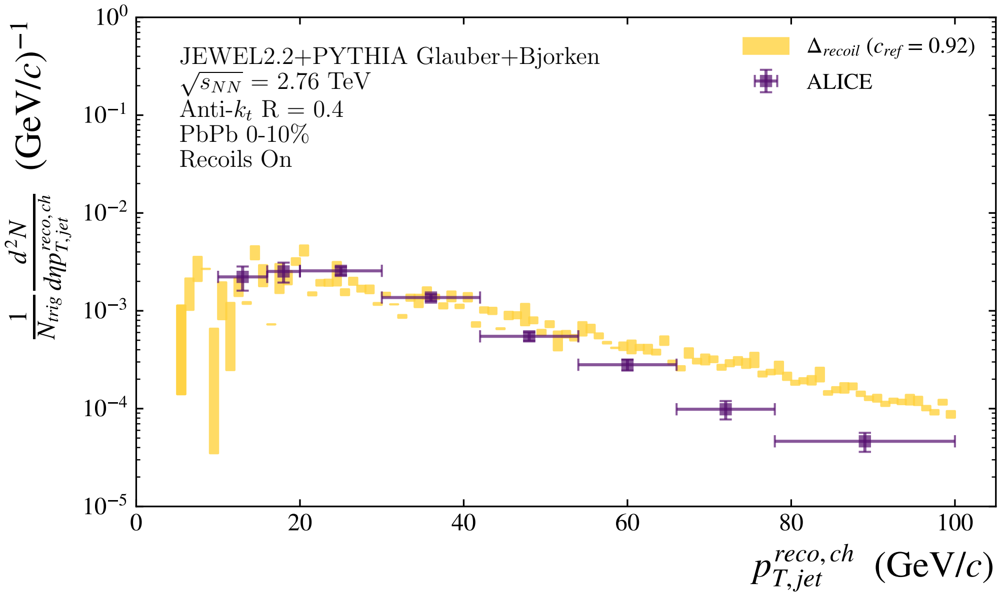

Figure 3.30: Distribution of Δ_{recoil} using JEWEL default configuration with recoils for R = 0.4 in central Pb-Pb collisions for Signal TT class $\{20,50\}$ and Reference TT class $\{8,9\}$. Data from [67].

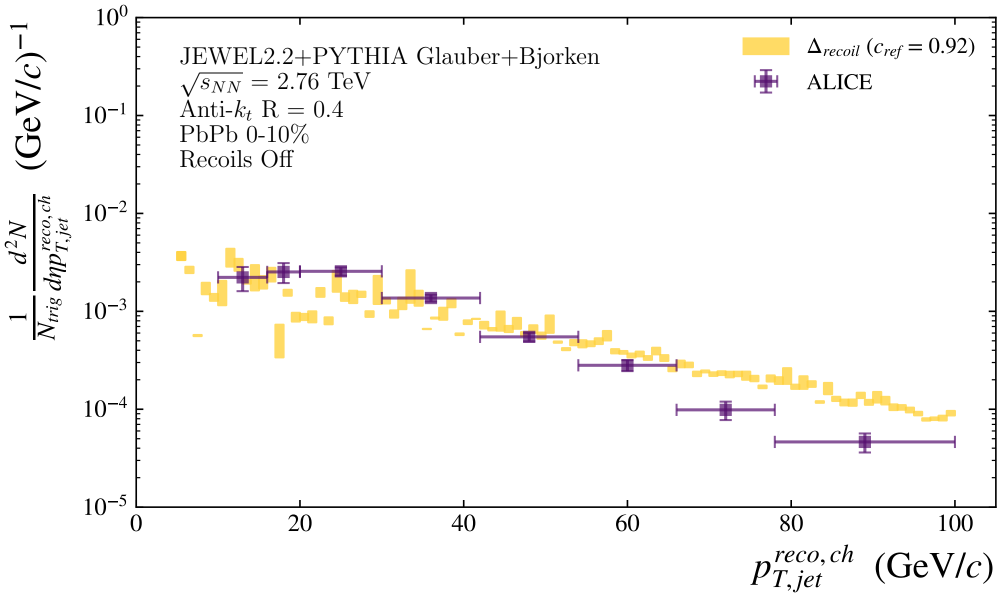

Figure 3.31: Distribution of Δ_{recoil} using JEWEL default configuration without recoils for R = 0.4 in central Pb-Pb collisions for Signal TT class {20,50} and Reference TT class {8,9}. Data from [67].

dent from the lack of significant changes in the distributions when comparing the JEWEL default configuration (Glauber+Bjorken) and the JEWEL with a more realistic medium (T$_R$ENTo + v-USPhydro).

Conclusions and future perspectives

Particularly, in this dissertation, there was a special focus on analyzing how the medium interferes in parton and jet production in relativistic heavy-ion collisions. By incorporating a more realistic medium into JEWEL, certain discoveries enabled a comprehensive explanation for certain effects observed in key observables of the analyzed system throughout the study. This underscores the significance of a faithfully realistic event-by-event hydrodynamic evolution of the Quark-Gluon Plasma (QGP).

In the initial segment of this dissertation, we examined the implications of implementing T$_R$ENTo + v-USPhydro on the first jet observable, the nuclear modification factor. Through its findings, it was possible to ascertain that the realistic medium better replicates the data, with a slight improvement for the model without thermal background subtraction. This can be observed both in central to peripheral collisions and when varying the jet radius R. The latter provides us with insights into how much the performed thermal subtraction contributes to the significant increase of R_{AA} with R.

Utilizing the nuclear modification factor as our fundamental study makes it possible to compare its results with those of other observables related to jets as well. This comparison aims to determine potential sensitivities to the medium.

To explore whether jet generation can be altered by interaction with the Quark-Gluon Plasma (QGP), similar to the case of R_{AA}, the di-jet observable x_J was studied across specific p_T and energy cuts. The findings reveal that there is no variation in the ratio between the transverse momenta of the two most energetic jets, irrespective of the initial conditions model of hydrodynamics or the medium evolution model employed. Consequently, this analysis indicates that the x_J observable is not sensitive to the medium.

This investigation underscores the importance of discerning which observables are influenced by the QGP's presence. The distinct behaviors observed between x_J and R_{AA} potentially provide insight into the complex interactions and modifications of parton processes within the evolving medium. Such insights contribute to our broader comprehension of the dynamics occurring in heavy-ion collisions and their implications for the

Quark-Gluon Plasma. The distinct behaviors observed between x_J and R_{AA} potentially provide insight into the complex interactions and modifications of parton processes within the evolving medium.

Regarding the study of the correlation between hadrons and jets, the simulation has revealed something intriguing: this observable does not appear to be influenced by the conditions of the environment to which it is subjected. This implies that its distribution remains consistent, irrespective of the environment, in central collisions with $R = 0.4$ and a center-of-mass energy of $\sqrt{s_{NN}} = 2.76$ TeV.

In concluding the study, the simulation results of the jet mass, denoted as M_{jet}, were analyzed to gain insights into how the medium can interfere with parton fragmentation processes, given that jet mass is a condensed measure of jet mass. The analysis of the central collision and different cuts on the jet's transverse momentum (p_T) led to the repetition of the behavior initially observed by the nuclear modification factor (R_{AA}). In other words, the optimal models were those that did not consider thermal background subtraction. Furthermore, the implementation of a realistic medium approached the experimental data used with subtle alignment.

In conclusion, the combination of models JEWEL, PYTHIA, T$_R$ENTo, and v-USPhydro has facilitated an enhanced description of specific observables while also furnishing diverse indicators of characteristics that arise during the collision process and within the simulation methodology. This includes insights into the rationale behind the thermal subtraction method exceeding its intended scope.

Appendix A

Simulation Parameters

To ensure the reproducibility of our research, we have provided a comprehensive list of the pertinent model parameters in this appendix. Specifically, with regard to JEWEL's configuration files, it's important to note that we have excluded details such as file names, random seeds, the number of events, and any centrality-specific entries. However, it's worth mentioning that any parameters not explicitly specified in our setup follow the default settings of JEWEL 2.0.0, as documented in [34].

In the case of each observable, several parameters of both JEWEL and the medium were modified. These parameters are listed in Table A.2.

In addition to the parameters governing JEWEL and the medium, it is essential to introduce the parameters for the initial conditions required by T$_R$ENTo. The specific parameters utilized in this study are presented in Table A.4 below for reference.

JEWEL CONFIGURATION FILE		
	Recoils On	Recoils Off
PTMIN	30 (GeV)	
PTMAX	1200 (GeV)	
ETAMAX	3.3	
WEIGHTED	T	
KEEPRECOILS	T	F
HADRO	T	
SHORTHEPMC	T	
WRITESCATCEN	T	F
WRITEDUMMIES	T	F

Table A.1: Parameters used in JEWEL configuration for all runs with and without recoils.

JEWEL CONFIGURATION FILE							
	R_{AA}		x_J		M_{jet}	h-jet	
NEVENT	399600		399600		1998000	1998000	
SQRTS [GeV]	2760	5020	2760	5020	2760	2760	5020

Table A.2: Parameters event number and energy used in JEWEL configuration for runs of each observable.

JEWEL MEDIUM CONFIGURATION FILE		
	Glauber + Bjorken	T$_R$ENTo + v-USPhydro
TI [GeV]	0.59	0.59
TAUI [GeV]	0.4	0.6
TC [GeV]	0.17	0.17
MDSCALEFAC	0.9	1.1*
SIGMANN [fm^2]	7.0	7.0

Table A.3: Medium parameters used in both JEWEL Glauber+Bjorken and JEWEL + T$_R$ENTo + v-USPhydro configuration for runs of each observable. *Without recoils, the Debey mass changes to 1.0 for realistic configuration.

T$_R$ENTo CONFIGURATION FILE	
Projectile	Pb
Projectile	Pb
Reduced Thickness	0.0
Fluctuation	1.6
Cross Section	7.0
Grid Max	12
Grid Step	0.06

Table A.4: Parameters used in T$_R$ENTo initial conditions.

Bibliography

[1] M. RIORDAN and W.A. ZAJC, *the first few microseconds*, *Scientific American* **294** (2006) 34A.

[2] U. Heinz and M. Jacob, *Evidence for a new state of matter: An assessment of the results from the cern lead beam programme*, 2000.

[3] e.a. STAR Collaboration: J. Adams, *Experimental and theoretical challenges in the search for the quark–gluon plasma: The STAR collaboration's critical assessment of the evidence from RHIC collisions*, *Nuclear Physics A* **757** (2005) 102.

[4] W. Florkowski, *Phenomenology of Ultra-Relativistic Heavy-Ion Collisions*, WORLD SCIENTIFIC (Mar., 2010), 10.1142/7396.

[5] *Ultrarelativistic Heavy-Ion Collisions*, Elsevier (2007), 10.1016/b978-0-444-52196-5.x5000-2.

[6] A. Banfi, *Hadronic Jets*, 2053-2571, Morgan & Claypool Publishers (2016), 10.1088/978-1-6817-4073-7.

[7] K.C. Zapp, F. Krauss and U.A. Wiedemann, *A perturbative framework for jet quenching*, *Journal of High Energy Physics* **2013** (2013) .

[8] T. Sjöstrand, S. Mrenna and P. Skands, *PYTHIA 6.4 physics and manual*, *Journal of High Energy Physics* **2006** (2006) 026.

[9] K.C. Zapp, *Geometrical aspects of jet quenching in jewel*, *Physics Letters B* **735** (2014) 157.

[10] Y. Tachibana, *Medium response to jet-induced excitation: theory overview*, *Nuclear Physics A* **982** (2019) 156.

[11] J. Noronha-Hostler, G.S. Denicol, J. Noronha, R.P.G. Andrade and F. Grassi, *Bulk viscosity effects in event-by-event relativistic hydrodynamics*, *Phys. Rev. C* **88** (2013) 044916.

[12] J. Noronha-Hostler, J. Noronha and M. Gyulassy, *The unreasonable effectiveness of hydrodynamics in heavy ion collisions*, *Nuclear Physics A* **956** (2016) 890.

[13] R.A. Gingold and J.J. Monaghan, *Smoothed particle hydrodynamics: theory and application to non-spherical stars*, *Monthly Notices of the Royal Astronomical Society* **181** (1977) 375.

[14] T. Kodama and T. Koide, *Stochastic variational method for viscous hydrodynamics*, *Physics* **4** (2022) 847.

[15] M.E. Peskin, *An Introduction To Quantum Field Theory*, CRC Press (may, 2018), 10.1201/9780429503559.

[16] *Quantum Chromodynamics*, Springer Berlin Heidelberg (2007), 10.1007/978-3-540-48535-3.

[17] A. Deur, S.J. Brodsky and G.F. de Téramond, *The QCD running coupling*, *Progress in Particle and Nuclear Physics* **90** (2016) 1.

[18] C. Gattringer and C.B. Lang, *Quantum Chromodynamics on the Lattice*, Springer Berlin Heidelberg (2010), 10.1007/978-3-642-01850-3.

[19] A. Maire, "Phase diagram of QCD matter : Quark-Gluon Plasma." 2015.

[20] T.L. collaboration, *Centrality determination in heavy-ion collisions with the LHCb detector*, *Journal of Instrumentation* **17** (2022) P05009.

[21] D.D. Chinellato, *Poster: From small to large: Particle production from proton-proton to lead-lead collisions*, in *3rd International þing on QCD Challenges from pp to AA*, August, 2019.

[22] A. Vaidya, "Jet physics at the lhc an introduction." `https://www.hep.ucl.ac.uk/postgrad/teaching/lhc/Jets_2017.pdf`, June, 2023.

[23] U. Heinz, *Towards the little bang standard model*, *Journal of Physics: Conference Series* **455** (2013) 012044.

[24] I. Karpenko, P. Huovinen and M. Bleicher, *A 3+1 dimensional viscous hydrodynamic code for relativistic heavy ion collisions*, *Computer Physics Communications* **185** (2014) 3016.

[25] Z.-Y. Shi, C. Gao and H. Zhai, *Ideal-gas approach to hydrodynamics*, *Phys. Rev. X* **11** (2021) 041031.

[26] L.D. Zanna, V. Chandra, G. Inghirami, V. Rolando, A. Beraudo, A.D. Pace et al., *Relativistic viscous hydrodynamics for heavy-ion collisions with ECHO-QGP*, *The European Physical Journal C* **73** (2013) .

[27] I. Karpenko, P. Huovinen and M. Bleicher, *A 3+1 dimensional viscous hydrodynamic code for relativistic heavy ion collisions*, *Computer Physics Communications* **185** (2014) 3016.

[28] H. Marrochio, J. Noronha, G.S. Denicol, M. Luzum, S. Jeon and C. Gale, *Solutions of conformal israel-stewart relativistic viscous fluid dynamics*, *Phys. Rev. C* **91** (2015) 014903.

[29] L. Du, U. Heinz and G. Vujanovic, *Hybrid model with dynamical sources for heavy-ion collisions at BES energies*, *Nuclear Physics A* **982** (2019) 407.

[30] I. Georgescu, *Simulating parton showers*, *Nature Reviews Physics* **3** (2021) 73.

[31] S. Cao and X.-N. Wang, *Jet quenching and medium response in high-energy heavy-ion collisions: a review*, *Reports on Progress in Physics* **84** (2021) 024301.

[32] Jing Wang, “Heavy-flavor production from pp to nucleus-nucleus collisions.”

[33] K. Zapp, J. Stachel and U.A. Wiedemann, *Local monte carlo implementation of the non-abelian landau-pomeranchuk-migdal effect*, *Physical Review Letters* **103** (2009) .

[34] K. Zapp, *JEWEL 2.0.0: directions for use*, *The European Physical Journal C* **74** (2014) .

[35] R. Baier, Y. Dokshitzer, A. Mueller and D. Schiff, *Medium-induced radiative energy loss equivalence between the BDMPS and zakharov formalisms*, *Nuclear Physics B* **531** (1998) 403.

[36] L. Barreto, *Study of Jet Modification in Relativistic Heavy-Ion Collisions*, Master's thesis, Sao Paulo U., 2021, 10.11606/D.43.2021.tde-05112021-191914.

[37] L. GROUP, "Large hadron collider."
urlhttps://www.mariangelalisanti.com/collider-physics, June, 2023.

[38] A. Buckley, J. Butterworth, S. Gieseke, D. Grellscheid, S. Höche, H. Hoeth et al., *General-purpose event generators for lhc physics*, *Physics Reports* **504** (2011) 145.

[39] C. Bierlich, *Rope Hadronization, Geometry and Particle Production in pp and pA Collisions*, Ph.D. thesis, Dec., 2016.

[40] C.-Y. Wong, *Introduction to High-Energy Heavy-Ion Collisions*, WSPC, hardcover ed. (9, 1994).

[41] J.D. Bjorken, *Highly relativistic nucleus-nucleus collisions: The central rapidity region*, *Phys. Rev. D* **27** (1983) 140.

[42] S. Basu, S. Thakur, T.K. Nayak and C.A. Pruneau, *Multiplicity and pseudo-rapidity density distributions of charged particles produced in pp, pA and AA collisions at RHIC LHC energies*, *J. Phys. G* **48** (2020) 025103 [`2008.07802`].

[43] J.S. Moreland, J.E. Bernhard and S.A. Bass, *Alternative ansatz to wounded nucleon and binary collision scaling in high-energy nuclear collisions*, *Phys. Rev. C* **92** (2015) 011901 [`1412.4708`].

[44] J. Noronha-Hostler, G.S. Denicol, J. Noronha, R.P.G. Andrade and F. Grassi, *Bulk viscosity effects in event-by-event relativistic hydrodynamics*, *Physical Review C* **88** (2013) .

[45] M.R. Whalley, D. Bourilkov and R.C. Group, *The Les Houches accord PDFs (LHAPDF) and LHAGLUE*, in *HERA and the LHC: A Workshop on the Implications of HERA and LHC Physics (Startup Meeting, CERN, 26-27 March 2004; Midterm Meeting, CERN, 11-13 October 2004)*, pp. 575–581, 8, 2005 [`hep-ph/0508110`].

[46] M. Cacciari, G.P. Salam and G. Soyez, *FastJet user manual*, *The European Physical Journal C* **72** (2012) .

[47] C. Bierlich, A. Buckley, J. Butterworth, C.H. Christensen, L. Corpe, D. Grellscheid et al., *Robust independent validation of experiment and theory: Rivet version 3*, *SciPost Physics* **8** (2020) .

[48] F. Canedo, *Study of jet quenching in relativistic heavy-ion collisions*, 2020.

[49] ATLAS Collaboration, *Measurement of the nuclear modification factor for inclusive jets in Pb+Pb collisions at* $\sqrt{s_{NN}} = 5.02$ *TeV with the ATLAS detector*, *Physics Letters B* **790** (2019) 108.

[50] L. Barreto, F.M. Canedo, M.G. Munhoz, J. Noronha and J. Noronha-Hostler, *Jet cone radius dependence of* r_{AA} *and* v_2 *at pbpb 5.02 tev from jewel*+$\mathrm{t_rento}$+*v-usphydro*, 2022.

[51] R. Baier, Y. Dokshitzer, A. Mueller, S. Peigné and D. Schiff, *Radiative energy loss and p*$\perp$*-broadening of high energy partons in nuclei*, *Nuclear Physics B* **484** (1997) 265.

[52] H. Qu, C. Li and S. Qian, *JetClass: A large-scale dataset for deep learning in jet physics*, 2022.

[53] H. Qu, C. Li and S. Qian, *Particle transformer for jet tagging*, 2022.

[54] J.E. Huth et al., *Toward a standardization of jet definitions*, in *1990 DPF Summer Study on High-energy Physics: Research Directions for the Decade (Snowmass 90)*, pp. 0134–136, 12, 1990.

[55] M. Seymour, *Jet shapes in hadron collisions: Higher orders, resummation and hadronization*, *Nuclear Physics B* **513** (1998) 269.

[56] G.P. Salam, *Towards jetography*, *The European Physical Journal C* **67** (2010) 637.

[57] J.G. Milhano and K. Zapp, *Improved background subtraction and a fresh look at jet sub-structure in jewel*, 2022.

[58] ALICE Collaboration*, *Measurements of inclusive jet spectra in pp and central Pb-Pb collisions at* $\sqrt{s_{NN}} = 5.02$ *TeV*, *Physical Review C* **101** (2020) .

[59] ATLAS collaboration, *Measurement of the nuclear modification factor for inclusive jets in Pb+Pb collisions at* $\sqrt{s_{\mathrm{NN}}} = 5.02$ *TeV with the ATLAS detector*, *Phys. Lett. B* **790** (2019) 108 [`1805.05635`].

[60] CMS collaboration, *First measurement of large area jet transverse momentum spectra in heavy-ion collisions*, *JHEP* **05** (2021) 284 [`2102.13080`].

[61] ATLAS collaboration, *Measurements of the Nuclear Modification Factor for Jets in Pb+Pb Collisions at* $\sqrt{s_{\mathrm{NN}}} = 2.76$ *TeV with the ATLAS Detector*, *Phys. Rev. Lett.* **114** (2015) 072302 [`1411.2357`].

[62] ATLAS COLLABORATION collaboration, *Measurements of the suppression and correlations of dijets in Pb+Pb collisions at* $\sqrt{s_{NN}} = 5.02$ *TeV*, *Phys. Rev. C* **107** (2023) 054908.

[63] ATLAS COLLABORATION collaboration, *Measurement of jet pT correlations in Pb+Pb and pp collisions at* $\sqrt{s_{NN}} = 2.76$ *TeV with the ATLAS detector*, *Physics Letters B* **774** (2017) 379.

[64] A.J. Larkoski, J. Thaler and W.J. Waalewijn, *Gaining (mutual) information about quark/gluon discrimination*, *Journal of High Energy Physics* **2014** (2014) .

[65] ALICE collaboration, *First measurement of jet mass in Pb–Pb and p–Pb collisions at the LHC*, *Phys. Lett. B* **776** (2018) 249 [`1702.00804`].

[66] Y.-T. Chien, R. Kelley, M.D. Schwartz and H.X. Zhu, *Resummation of jet mass at hadron colliders*, *Physical Review D* **87** (2013) .

[67] ALICE Collaboration, *Measurement of jet quenching with semi-inclusive hadron-jet distributions in central pb-pb collisions at* $\sqrt{s_{NN}} = 2.76$ *tev*, *Journal of High Energy Physics* **2015** (2015) .